



KATHOLIEKE UNIVERSITEIT LEUVEN  
FACULTEIT DER INGENIEURSWETENSCHAPPEN  
DEPARTEMENT ELEKTROTECHNIEK  
Kasteelpark Arenberg 10, 3001 Leuven (Heverlee)

**SUBSPACE-BASED QUANTIFICATION OF  
MAGNETIC RESONANCE SPECTROSCOPY DATA  
USING BIOCHEMICAL PRIOR KNOWLEDGE**

**Promotoren:**  
Prof. dr. ir. S. Van Huffel  
Prof. dr. ir. L. De Lathauwer

**Proefschrift voorgedragen tot  
het behalen van het doctoraat  
in de ingenieurswetenschappen  
door  
Teresa LAUDADIO**

**December 2005**



KATHOLIEKE UNIVERSITEIT LEUVEN  
FACULTEIT DER INGENIEURSWETENSCHAPPEN  
DEPARTEMENT ELEKTROTECHNIEK  
Kasteelpark Arenberg 10, 3001 Leuven (Heverlee)

**SUBSPACE-BASED QUANTIFICATION OF  
MAGNETIC RESONANCE SPECTROSCOPY DATA  
USING BIOCHEMICAL PRIOR KNOWLEDGE**

Jury:

Prof. dr. E. Aernoudt, voorzitter  
Prof. dr. ir. S. Van Huffel, promotor  
Prof. dr. ir. L. De Lathauwer, promotor  
Prof. dr. B. Celda, (Universidad de València)  
Prof. dr. ir. M. Moonen,  
Prof. dr. R. Sepulchre, (Université de Liège)  
Prof. dr. ir. M. Van Barel, (Computer Science)  
Prof. dr. P. Van Hecke, (Faculty of Medicine)

Proefschrift voorgedragen tot  
het behalen van het doctoraat  
in de ingenieurswetenschappen  
door

**Teresa LAUDADIO**

©Katholieke Universiteit Leuven – Faculteit Ingenieurswetenschappen  
Arenbergkasteel, B-3001 Heverlee (Belgium)

Alle rechten voorbehouden. Niets uit deze uitgave mag vermenigvuldigd en/of openbaar gemaakt worden door middel van druk, fotocopie, microfilm, elektronisch of op welke andere wijze ook zonder voorafgaande schriftelijke toestemming van de uitgever.

All rights reserved. No part of the publication may be reproduced in any form by print, photoprint, microfilm or any other means without written permission from the publisher.

D/2005/7515/88

ISBN 90-5682-654-9

---

---

# CONTENTS

<b>SYMBOLS AND ACRONYMS</b>	<b>ix</b>
<b>ACKNOWLEDGMENTS</b>	<b>xiii</b>
<b>ABSTRACT</b>	<b>xvii</b>
<b>1 INTRODUCTION</b>	<b>1</b>
1.1 Basic principles of NMR	2
1.1.1 Magnetic Resonance Spectroscopy (MRS)	6
1.1.2 Magnetic Resonance Imaging (MRI)	7
1.1.3 Magnetic Resonance Spectroscopic Imaging (MRSI)	7
1.2 Clinical relevance of MRS and MRSI data for diagnosis and treatment of cancer	8
1.3 Goals of the thesis	11
1.4 Structure of the thesis	12
1.5 Conclusions	14
<b>2 QUANTIFICATION OF MRS SIGNALS: AN OVERVIEW OF TIME-DOMAIN METHODS</b>	<b>15</b>
2.1 Time-domain parameter estimation methods	16
2.2 Theoretical model of the MRS signal	16
2.3 Biochemical Prior Knowledge	17
2.4 Optimization-based methods: VARPRO, AMARES and AQSES	18
2.5 Subspace-based methods: HSVD	22
2.5.1 HSVD - noiseless data	22
2.5.2 HSVD - noisy data	24
	<b>v</b>

---

2.5.3	HTLS	24
2.6	Subspace-based methods using biochemical prior knowledge	26
2.6.1	HTLSPK(fd)	27
2.6.2	HTLSPK(fp)	28
2.6.3	HTLSPK(fdp)	29
2.6.4	HTLSPK(p)	30
2.6.5	HTLSPK( $\Delta f d_{eq}$ )	30
2.6.6	HTLSPKfast( $\Delta f d_{eq}$ )	31
2.7	Conclusions	34
<b>3</b>	<b>IMPROVED LANCZOS ALGORITHMS FOR SUBSPACE-BASED MRS DATA QUANTIFICATION</b>	<b>35</b>
3.1	Computing the truncated SVD	36
3.2	The Lanczos bidiagonalization algorithm	37
3.2.1	Circulant matrices	38
3.2.2	Embedding a Toeplitz matrix in a circulant matrix	39
3.2.3	Toeplitz matrix-vector multiplication	40
3.2.4	Hankel matrix-vector multiplication	41
3.3	The Lanczos algorithm with partial reorthogonalization	41
3.4	The implicitly restarted Lanczos algorithm	41
3.5	HLSVD	42
3.6	Lanczos-based HSVD methods: a numerical comparison	43
3.6.1	Comparison in computational efficiency	43
3.6.2	Statistical accuracy measure	45
3.6.3	HSVD for solvent suppression	45
3.6.4	HLSVD accuracy aspects	48
3.7	Conclusions	49
<b>4</b>	<b>SUBSPACE-BASED MRS DATA QUANTIFICATION OF MULTIPLETS USING PRIOR KNOWLEDGE</b>	<b>51</b>
4.1	KNOB-TLS algorithm for multiplet parameter estimation	52
4.1.1	The KNOB-SVD algorithm	53
4.1.2	Outline of the KNOB-TLS algorithm	60
4.2	Quantification of a simulated MRS signal	62
4.3	Quantification of <i>In vivo</i> MRS signals	66
4.3.1	<i>In vivo</i> $^{31}\text{P}$ signals	66
4.3.2	<i>In vivo</i> $^1\text{H}$ signals	68
4.4	Conclusions	71

---

<b>5</b>	<b>TISSUE SEGMENTATION AND CLASSIFICATION OF MRSI DATA USING CCA</b>	<b>73</b>
5.1	Tissue segmentation of MRSI data	74
5.2	Canonical Correlation Analysis	75
5.2.1	Algorithm CCA-GEP: CCA by solving a Generalized Eigenvalue Problem (GEP)	77
5.2.2	Algorithm CCA-PA: CCA by computing Principal Angles (PA)	77
5.3	CCA applied to MRSI data	78
5.3.1	Choice of the spatial model	79
5.3.2	Choice of the subspace model	80
5.4	Simulation studies	81
5.4.1	Simulation results	83
5.5	<i>In vivo</i> studies	91
5.5.1	<i>In vivo results</i>	91
5.6	Conclusions	95
<b>6</b>	<b>FAST NOSOLOGICAL IMAGING OF 2DTSI BRAIN DATA BASED ON CCA</b>	<b>97</b>
6.1	Biochemical features of brain tumors	98
6.2	Turbo Spectroscopic Imaging applied to brain	99
6.3	Tissue segmentation and classification of 2DTSI brain data using CCA	99
6.3.1	Acquisition of 2DTSI brain data	99
6.3.2	CCA applied to 2DTSI brain data: selection of the model spectra	102
6.3.3	CCA applied to 2DTSI brain data: selection of the subspace and spatial models	103
6.3.4	Detection results: Example 1	103
6.3.5	Detection results: Example 2	109
6.3.6	Detection results: Example 3	110
6.3.7	Detection results: Example 4	111
6.3.8	Detection results: Example 5	112
6.4	Conclusions	113
<b>7</b>	<b>CONCLUSIONS AND FURTHER RESEARCH</b>	<b>131</b>
7.1	Summary	132
7.1.1	Quantification of MRS signals	132
7.1.2	Quantification of MRS signals using prior knowledge	132
7.1.3	Tissue segmentation and classification of prostate MRSI data	133

7.1.4	Tissue segmentation and classification of brain 2DTSI data	133
7.2	Further research	134
7.2.1	CCA based on selected MRSI data features	134
7.2.2	CCA applied to three-dimensional MRSI data	134
7.2.3	Tissue assignment criterion in CCA	134
7.2.4	Multistage CCA	135
<b>BIBLIOGRAPHY</b>		<b>137</b>

---

---

# SYMBOLS AND ACRONYMS

The current section lists the symbols and acronyms that occur frequently in this thesis. The last column refers to the page on which the symbol or acronym is first used and/or defined.

Remark. The notation used in this thesis allows the reader to distinguish between scalars, vectors and matrices. Lower-case characters represent scalar values. Boldface lower-case characters are used for vectors. Boldface capitals represent matrices.

## List of symbols

$a_k$	amplitude of the $k$ th sinusoid	<i>page 16</i>
$\mathbf{A}^T$	transpose of $\mathbf{A}$	
$\mathbf{A}^H$	hermitian transpose of $\mathbf{A}$	
$\mathbf{A}^{-1}$	inverse of $\mathbf{A}$	
$\ \mathbf{A}\ _2$	Euclidean norm of $\mathbf{A}$	
$\mathbf{A}^\uparrow$	matrix obtained by deleting the top row of $\mathbf{A}$	<i>page 23</i>
$\mathbf{A}^\downarrow$	matrix obtained by deleting the last row of $\mathbf{A}$	<i>page 23</i>
$c_k$	complex amplitude $a_k e^{j\phi_k}$ of the $k$ th sinusoid	<i>page 22</i>
$\mathbb{C}$	the set of complex numbers	<i>page 23</i>
$Cov[\cdot]$	covariance operator	<i>page 75</i>
$d_k$	damping factor of the $k$ th sinusoid	<i>page 16</i>
$e_n$	the $n$ th noise sample	<i>page 16</i>
$E[\cdot]$	expected value operator	<i>page 75</i>
$eig(\cdot)$	eigenvalues of $(\cdot)$	<i>page 23</i>
$f_k$	frequency of the $k$ th sinusoid	<i>page 16</i>
$\mathbf{I}_n$	$n \times n$ identity matrix	
$j$	imaginary unit	<i>page 16</i>
$\mathbf{0}$	a zero vector or matrix	
$\mathbf{H}$	noisy Hankel data matrix	<i>page 24</i>
$\bar{\mathbf{H}}$	noiseless Hankel data matrix	<i>page 22</i>
$K$	model order	<i>page 16</i>
$N$	number of data samples	<i>page 16</i>
$O$	order of magnitude	<i>page 38</i>
$t_n$	the $n$ th time sample	<i>page 16</i>
$t_0$	begin time	<i>page 16</i>
$\Delta t$	sampling time interval	<i>page 16</i>
$\Delta \omega$	sampling frequency interval	<i>page 80</i>
$S(\omega_n)$	magnitude spectrum	<i>page 80</i>
$V[\cdot]$	variance operator	<i>page 75</i>
$z_k$	signal pole of the $k$ th sinusoid	<i>page 22</i>
$\phi_k$	phase of the $k$ th sinusoid	<i>page 16</i>

**List of acronyms and abbreviations**

a.u.	arbitrary unit	<i>page 62</i>
ATP	adenosine triphosphate	<i>page 7</i>
Cho	Choline	<i>page 8</i>
Citr	Citrate	<i>page 8</i>
Cr	Creatine	<i>page 8</i>
CRB	Cramer-Rao bound	<i>page 17</i>
CSI	chemical shift imaging	<i>page 8</i>
dB	decibel	<i>page 43</i>
FID	free induction decay	<i>page 4</i>
FIR	finite impulse response	<i>page 21</i>
Hz	Hertz	
Lac	lactate	<i>page 10</i>
Lip	lipids	<i>page 10</i>
LS	least squares	<i>page 19</i>
mM	milliMolar	
MRS	magnetic resonance spectroscopy	<i>page 2</i>
MRSI	magnetic resonance spectroscopy imaging	<i>page 2</i>
ml	milliliter	
mm	millimeter	
ms	millisecond	
NAA	N-acetyl-aspartate	<i>page 9</i>
NMR	nuclear magnetic resonance	<i>page 2</i>
NLLS	nonlinear least squares	<i>page 19</i>
ppm	part per million	<i>page 6</i>
PCr	phosphocreatine	<i>page 7</i>
PDE	phosphodiester	<i>page 7</i>
$P_i$	inorganic phosphate	<i>page 7</i>
PME	phosphomonoester	<i>page 7</i>
RF	radio frequency	<i>page 5</i>
(R)RMSD	(relative) root mean square difference	<i>page 67</i>
(R)RMSE	(relative) root mean square error	<i>page 45</i>
s	second	
SNR	signal to noise ratio	<i>page 4</i>
SVD	singular value decomposition	<i>page 12</i>
T	Tesla	
TLS	total least squares	<i>page 24</i>



---

---

# ACKNOWLEDGMENTS

At the end of my Ph.D. journey, it is time to look back at the years of my life spent in Leuven and to thank all the people who supported me throughout my Ph.D. experience. This work would not have been possible without their contributions and friendship.

First of all, I would like to express my deep gratitude to my supervisor Prof. Sabine Van Huffel. I thank her for offering me the immeasurable opportunity of starting my Ph.D. studies and, above all, for introducing me in the fascinating world of the research in Biomedical Signal Processing. I know she considers me a motivated student. The reason of my motivation is due to the hope that our research can really help to improve the quality of people's lives. I also thank her for the endless availability, encouragement, guidance and insightful comments that, during these years, significantly contributed to the contents of this thesis.

I would also like to thank my co-supervisor Dr. Lieven De Lathauwer, whose broad and deep knowledge in Mathematics and Signal Processing, strongly contributed to improve the quality of the research achievements of the last two years. I thank him for his availability, encouragement and for the clarity with which he explained the solution of various problems to me. I also thank him for introducing me in the world of the tensors' theory. It is my desire to continue studying and to learn to apply this new and powerful theory in the near future.

This work would not have been possible without the presence of Prof. Paul Van Hecke of the Faculty of Medicine, member of the reading committee, who offered me the big opportunity of starting my research activity in 2001 for the EC TMR project on MRI/MRS, entitled "Advanced signal processing for medical MRI and spectroscopy". I thank him for providing me most of the MRS/MRSI data sets I processed, for all his valuable suggestions and comments, and for answering all my questions.

Many thanks to Prof. Marc Moonen and Prof. Marc Van Barel, members of the

reading committee, for their profound reading of the manuscript and their important suggestions and comments.

During the last year of my Ph.D., I had the nice opportunity to be involved in the eTUMOUR EU project and I had the great pleasure to meet Prof. Bernardo Celda and Dr. M.Carmen Martínez-Bisbal, from the University of València. In particular, the last part of this thesis has arisen out of a cooperation with them. I would like to thank them for providing me the 2DTSI data sets and, above all, for their large expertise and many valuable comments they provided me whenever I needed. It has been a great pleasure to work with them!

I would also like to express my gratitude to Prof. Bernardo Celda for so kindly accepting to come to Leuven and be a member of the Jury.

I am very grateful to Prof. Rodolphe Sepulchre for the great honor he so kindly conceded me by accepting to come to Leuven and be a member of the Jury.

Prof. E. Aernoudt is gratefully acknowledged for chairing the Jury.

Very special thanks go to Dr. Leentje Vanhamme, with whom I had the great pleasure to work together during the first years of my doctoral studies. I am deeply grateful to her for the endless scientific and human support she provided me during my Ph.D. and my stay in Leuven, especially in difficult times. I immediately realized that I had found one of my best friends in Belgium. I will never forget all her advices and the nice time we spent together. Thanks!

My special thanks also go to another of my best friends, Bart De Neuter, with whom I had the luck to share the office for four years. I thank him for supplying a nice and funny work atmosphere. I already miss the great times I had together with him and Leen during our working hours and sport activities. I thank him for the help he offered me whenever I did not know a particular software. I would also like to thank Bart's girlfriend, Jacinta, for the warm friendship and endless availability.

A hearty thank is sent out to all the friends and colleagues I had the pleasure to work with at ESAT: Philippe, Diana, Mieke, Ivan, Andy, Lukas, Chuan, Geert, Jean-Michel, Wim, Anneleen, Bart, Pieter, Jean-Baptiste, Maarten, Jan, Arjan and Ben. Thanks for providing a rich and warm work atmosphere!

Special thanks go to Philippe, Diana and Mieke for their unconditioned availability whenever I needed help. Thanks!

Although they do not belong to the Biomed group, I would also like to thank Ellen, Nico, Joris, Raf and Maria for their friendship and the great times we had together.

On a monetary note, I thank the K.U.Leuven, and the eTUMOUR and BIOPATTERN EU projects, for financing my Ph.D. research. A special word of thank goes

to Ida Tassens, Ilse Pardon and Bart Motmans for arranging any number of practical issues.

In the last months I have also been working with Dr. Antonio Lamura, Dr. Giovanni Nico and Dr. Massimo Ladisa, of the National Research Council, Bari, Italy. I want them to know that it is a honor and a pleasure for me to work with such valid Italian researchers and I hope our collaboration will be very productive in the near future.

My parents and my brother missed me so much during the years I spent in Leuven. There are no words to express my gratitude for all the selfless efforts they made for me and their support in all my choices. In particular, I would like to thank my mother for her love, friendship and endless encouragement, especially in difficult times.

A special thought goes to my father in law, who is living a difficult moment of his life. I would like to thank him for all the times he wished me “good luck” during these years, for his positive view of the life he tried to transfer to me and for the proudness he showed me whenever he heard about some of my achievements.

Last but not least, I would like to thank the person closest to me: my husband Nicola. It was not easy to live far away from each other during these last years, but I am so proud we have been able to face such a situation! I thank him for all his understanding and caring, and for being so confident about my abilities. If now I can write these Ph.D. thesis acknowledgements, it is only because he strongly encouraged me to make this big change in my life. This achievement would not have been possible without his support. It is with my deepest love I dedicate this thesis to him.



---

---

# ABSTRACT

Nowadays, Nuclear Magnetic Resonance (NMR) is widely used in oncology as a non-invasive diagnostic tool in order to detect the presence of tumor regions in the human body. An application of NMR is Magnetic Resonance Imaging, which is applied in routine clinical practice to localize tumors and determine their size. Magnetic Resonance Imaging is able to provide an initial diagnosis, but its ability to delineate anatomical and pathological information is significantly improved by its combination with another NMR application, namely Magnetic Resonance Spectroscopy. The latter reveals information on the biochemical profile tissues, thereby allowing clinicians and radiologists to identify in a non-invasive way the different tissue types characterizing the sample under investigation, and to study the biochemical changes underlying a pathological situation. In particular, an NMR application exists which provides spatial as well as biochemical information. This application is called Magnetic Resonance Spectroscopic Imaging (MRSI) and involves the simultaneous acquisition of signals from many volume elements.

The success of MRSI as a diagnostic tool depends on the accurate estimation of the concentrations of the chemical compounds that are present in the suspicious region. Such quantities can be obtained by computing the physical parameters that characterize the MRSI signals located in that region. The first part of the thesis concerns the development of accurate, robust and efficient algorithms for the quantification of time domain MRSI signals. A variety of methods are available in the literature. They are generally divided into two classes: optimization-based methods and subspace-based methods. The former are iterative, require user involvement and allow inclusion of biochemical prior knowledge. The subspace-based methods are easier to use, since minimal user interaction is required, but they allow limited incorporation of biochemical prior knowledge. In this thesis, we focus on the latter class. In particular, we develop an improved version of the popular HLSVD method. This method is very frequently used in NMR for solvent suppression and is freely available in the MRUI software package. Our studies show that sometimes HLSVD fails in the estimation of the parameters of interest because some numerical problems occur in its implementation, which is based on the Lanczos algorithm for

the computation of the truncated SVD of the Hankel data matrix. We propose two alternative variants of HLSVD, namely HLSVD-PRO (based on the Lanczos algorithm with partial reorthogonalization) and HLSVD-IRL (based on the implicitly restarted Lanczos algorithm), which are able to outperform HLSVD in terms of accuracy and efficiency.

In the literature, it has extensively been proved that the performance of parameter estimation methods significantly improves if biochemical prior knowledge is used. In this thesis we propose a new subspace-based method called KNOB-TLS, which allows the use of more prior knowledge about the signal parameters than previously published subspace-based methods. Extensive simulation and *in vivo* studies show that the proposed algorithm performs best in terms of robustness and accuracy and provides results that are comparable to those of the optimization-based methods.

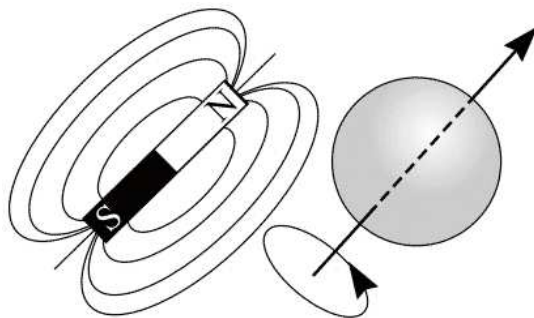
The final topic is the development of a fast and accurate tissue segmentation and classification technique. This is based on a statistical method, called Canonical Correlation Analysis, able to simultaneously exploit the spectral and spatial information characterizing the MRSI data. The potential and limitations of the new technique to retrieve the possible tissue types characterizing the considered sample, are investigated. Moreover, its performance is compared to that of ordinary correlation analysis, which does not exploit any spatial information. Extensive simulation and *in vivo* studies are carried out by using prostate MRSI data as well as two-dimensional Turbo Spectroscopic Imaging brain data. Test results show that the proposed tissue typing technique is fast and accurate, even when the region under investigation presents a high degree of heterogeneity. Furthermore, it outperforms ordinary correlation analysis in robustness and accuracy.

# INTRODUCTION

*In this chapter the theoretical foundations of nuclear magnetic resonance (NMR) are introduced and a description of possible biomedical applications is provided. More precisely, in Section 1.1 the basic principles of NMR are explained and the different applications of NMR, such as magnetic resonance spectroscopy (MRS), magnetic resonance imaging (MRI) and magnetic resonance spectroscopic imaging (MRSI), are introduced. In Section 1.2 the relevance, for clinical purposes, of the analysis of NMR data is illustrated. In Section 1.3 the goals of the thesis are defined and, finally, Section 1.4 provides an overview of the thesis structure.*

## 1.1 Basic principles of NMR

Nuclear magnetic resonance represents a powerful non-invasive diagnostic tool, used in daily radiological practice to obtain clinical images and to study the chemical composition and structure of tissues *in vivo*. Unlike conventional radiography and Computed Tomographic imaging, which make use of potentially harmful radiations (X-rays), NMR is based on the magnetic properties of atoms. It is well known that subatomic particles (protons, electrons and neutrons) possess a property called spin. Spin can be visualized as a rotating motion of the particle around its own axis. In many atoms these spins are paired against each other and the nucleus of the atom has no overall spin. However, there exist some atoms, such as proton ( $^1\text{H}$ ) and phosphorus ( $^{31}\text{P}$ ), in which the nucleus is characterized by an overall spin. The nuclei of the aforementioned atoms for instance possess an overall spin  $I$  equal to  $\frac{1}{2}$ . According to quantum mechanics, when atoms are embedded in a magnetic field, their nuclei can only assume a precise number of possible orientations given by  $2I + 1$ , equal to 2 for the considered nuclei. Let us focus on  $^1\text{H}$  nuclei. As they have a positive charge, the spinning motion causes a magnetic moment in the direction of the spin axis, as shown in Figure 1.1.



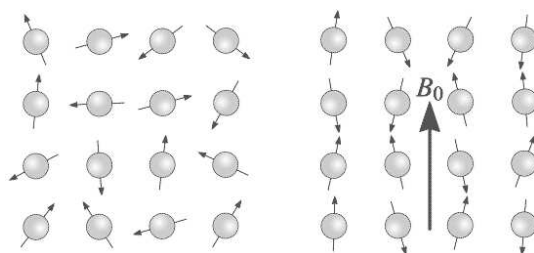
**Figure 1.1.** A charged spinning nucleus creates a magnetic moment which acts like a bar magnet (dipole).

Figure 1.2 (left) shows a system of  $^1\text{H}$  nuclei. When no external magnetic field is applied, the magnetic moments assume random orientations. However, if an

external magnetic field  $B_0$  is applied, the magnetic moments align with the direction of  $B_0$  by adopting one of the two allowed orientations, parallel and anti-parallel, with respect to the external field, as shown in Figure 1.2 (right). The spin axes are not exactly aligned with  $B_0$ , but they precess around  $B_0$  with a characteristic frequency  $f$  defined by the Larmor equation

$$f = \frac{\gamma B_0}{2\pi}, \quad (1.1.1)$$

where  $\gamma$  is a constant and is called the gyromagnetic ratio of the nucleus, and  $f$  represents the so-called Larmor frequency.



**Figure 1.2.** A collection of  $^1\text{H}$  nuclei in the absence of an externally applied magnetic field (left) and in presence of an external magnetic field  $B_0$  (right).

The two possible orientations are characterized by different energy levels and the initial populations of the spins along the two directions are determined by thermodynamics. Indeed, if the temperature of the system were absolutely zero, all spins would adopt the parallel orientation, characterized by the lowest energy level. When thermal energy is present, an amount of energy equal to the difference between the two energy states, denoted by  $\Delta E$ , is supplied to some of the spins which, therefore, will assume the orientation with highest energy level. The energy difference  $\Delta E$  between the two possible states is proportional to the applied field and given by

$$\Delta E = \frac{\gamma \hbar B_0}{2\pi}, \quad (1.1.2)$$

where  $\hbar$  represents the Planck constant.

At any given instant, the magnetic moments of the considered system of  $^1\text{H}$  nuclei can be represented as vectors, as shown in Figure 1.3. Every vector can be decomposed into its components perpendicular and parallel to  $B_0$ . For a large enough number of spins, the perpendicular components cancel each other. Since most spins adopt the parallel orientation rather than the anti-parallel one, a net magnetization  $M$  can be observed in the direction of the  $B_0$  field.

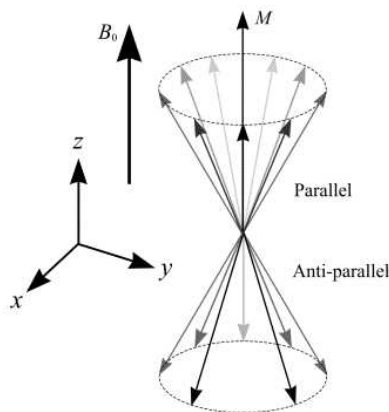


**Figure 1.3.** A collection of spins at any given instant in an external magnetic field  $B_0$ . A small net magnetization  $M$  can be observed in the direction of  $B_0$ .

When an additional oscillating magnetic field is applied to the system, with direction perpendicular to that of  $B_0$  and frequency equal to the Larmor frequency, spins are excited from the lower to the higher energy state. If the direction of  $B_0$  is aligned with the  $z$  axis of an Euclidean 3-space, the swap of the spins from the parallel to the anti-parallel state causes the  $M$  vector to tilt from the  $z$  direction into the  $x$ - $y$  plane. When the oscillating magnetic field is turned off, spins return to their equilibrium state and, at the same time, the vector  $M$  begins to precess around the  $z$  axis until it recovers its original direction. This phenomenon allows the detection of an NMR signal. In fact, during its precession motion,  $M$  induces an electromotive force in a receiver coil according to Faraday's law of magnetic induction. Figure 1.4 (left) schematically shows the detection procedure of the signal, while Figure 1.4 (right) shows a graph versus time of the signal induced in the receiver coil. Such a signal is called free induction decay (FID) and, as can be observed in the figure, it corresponds to an oscillation that gradually dies out in the time domain. In order to obtain a graph easier to interpret from a visual point of view, the FID is subjected to Fourier transformation so that a conventional spectrum is obtained, in which the signal amplitude is plotted as a function of frequency.

It is important to observe that the magnitude of the signal depends on the number of nuclei contributing to produce the transverse magnetization. Normally, this number is not very large and, therefore, the signal is characterized by a low signal-to-noise ratio (SNR). In order to increase the intensity of the signal and obtain a higher SNR, a number of acquisitions is performed consecutively and the final signal is the average of all measured signals. Moreover, as shown in Eq.(1.1.2), the higher the field strength  $B_0$  the higher the energy difference between both states. This will increase the amount of emitted energy and, hence, signals with higher intensity can

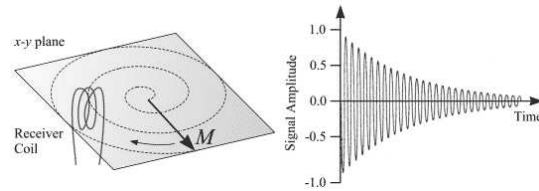


**Figure 1.4.** Left: after a  $90^\circ$  RF pulse,  $M$  lies in the x-y plane and rotates around the z axis. The component of  $M$  in the x-y plane decays over time. Right: an alternating current is induced in the receiver coil.

be produced.

The return of  $M$  to its equilibrium state is known as relaxation. There are three factors that influence the decay of  $M$ : inhomogeneity of the magnetic field  $B_0$ , longitudinal  $T_1$  relaxation and transverse  $T_2$  relaxation.

The first factor consists of the impossibility of producing a perfectly uniform magnetic field. In fact, during an NMR experiment, the sample under investigation experiences different  $B_0$ 's and, therefore, its nuclei that exhibit spin have different precessional frequencies (according to the Larmor equation). This causes phase differences at various points across the sample, which will increase with time. The resultant vector of these phases reduces the x-y component of  $M$  with time.

The second factor, known as  $T_1$  relaxation, is due to the realignment of the spins (and so of  $M$ ) with the external magnetic field  $B_0$ . When the oscillating magnetic field is switched off, nuclei dissipate their excess energy as heat to the surrounding environment in order to revert to their equilibrium state. Realignment of the spins along  $B_0$  leads to a gradual increase of the z component of  $M$  and, at the same time, to a corresponding decrease of its x-y component. The time needed for the recovery of the magnetization along the direction of  $B_0$  is denoted by the constant  $T_1$ .

While nuclei dissipate their excess of energy, the magnetic moments interact with each other causing a further decrease of the x-y component of  $M$ . This phenomenon is known as  $T_2$  relaxation and the decrease of the transverse magnetization is called decay. The rate of decay is described by a time constant,  $T_2$ , that represents the time needed for the relaxation process in the plane perpendicular to  $B_0$ .

It is important to observe that the parameters  $T_1$  and  $T_2$  are tissue-specific time constants and, thus, introduce the possibility of separating different tissue types.

In conclusion, an NMR experiment consists of applying a radio frequency (RF) pulse with a bandwidth chosen to excite all the nuclei within the required frequency range and acquiring the response, the FID signal. This process is repeated until the desired SNR is obtained. Many special pulse sequences have been developed in order to enhance the quality and information content of the spectra. In fact, spectra obtained with different pulse sequence parameters can exhibit significant differences. An important parameter in that respect is the so called echo time (TE). Typically,

long ( $TE \geq 130$  ms) and short ( $TE \leq 50$  ms) echo times are used. The two types of spectra differ for the number of peaks as well as for their shapes. In particular, short echo time spectra are characterized by a larger number of peaks that very often exhibit a high overlap. Moreover, very broad and underlying peaks can also be observed which are due to the signals from macromolecules [3].

### 1.1.1 Magnetic Resonance Spectroscopy (MRS)

Nuclei of different atoms can be easily distinguished from one another since they are characterized by a different  $\gamma$  and thus resonate at different frequencies. Nuclei of the same isotope, but belonging to different molecules are differentiable due to the so-called shielding effect. Indeed, the magnetic field at each nucleus is not equal to the applied field  $B_0$  since it is slightly perturbed by the electrons that surround the nucleus. This causes the Larmor precession frequency to be modified by the chemical environment of the spin. The effect of chemical shift is described by the equation

$$B = (1 - \sigma)B_0, \quad (1.1.3)$$

where  $\sigma$  is the shielding constant, a dimensionless number that depends on the electrical environment of the nucleus. This modifies the Larmor frequency as follows

$$f = \frac{\gamma(1 - \sigma)B_0}{2\pi}, \quad (1.1.4)$$

which is detected, upon Fourier transformation of the FID, as a shift in frequency from that expected if chemical shift played no part. Therefore, nuclei in a different chemical environment emit signals with different frequencies. This property makes MRS signals very useful since the different molecular structures composing the sample under investigation can be clearly identified and their analysis can lead to important biomedical information. Figure 1.5 shows the real part of the spectrum of a  $^{31}\text{P}$  MRS signal, in which different molecules (peaks) can be observed.

It is common to express the chemical shift of a peak in the spectrum in terms of the relative difference in frequency from a reference peak. The chemical shift in parts per million (ppm) is therefore defined as

$$\delta = \frac{f - f_{ref}}{f_{ref}} \times 10^6 \text{ ppm}, \quad (1.1.5)$$

where  $f$  and  $f_{ref}$  represent the resonance frequencies of the peak of interest and of the reference component, respectively.

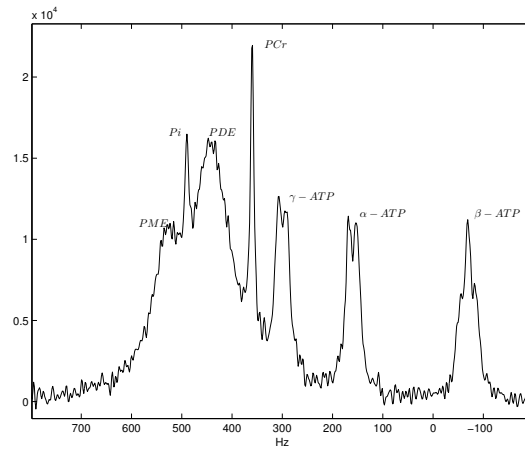


Figure 1.5. Real part of the spectrum of a  $^{31}\text{P}$  MRS signal.

### 1.1.2 Magnetic Resonance Imaging (MRI)

NMR is widely applied in order to obtain *in vivo* clinical images of tissues in the human body. This particular application is called MRI and is based on the detection of signals from water. The proton nuclei possess the strongest magnetic moment and are present in high abundance in biological material. In particular, the protons of water generate strong signals and, consequently, this type of nucleus is most widely used in MRI. The proton signals from other compounds are used for metabolic studies.

The theoretical principles of MRI coincide with the general ones explained in section 1.1.1, but gradients need to be applied to the external magnetic field  $B_0$  in order to construct images. More precisely, if no gradient were applied, all the water protons would give rise to a signal of the same frequency, but no information about their spatial distribution would be available. Lauterbur (1973) solved this problem by introducing gradients in the magnetic field. These gradients modify the strength of  $B_0$  which is no longer constant and, specifically, varies linearly as a function of the distance. According to the Larmor equation, the new magnetic field causes identical nuclei to precess at different Larmor frequencies. The frequency deviation is proportional to the distance of each nucleus from the center of the coil and, hence, the position of the nucleus can be identified.

### 1.1.3 Magnetic Resonance Spectroscopic Imaging (MRSI)

MRSI can be considered as a combination of MRS and MRI. As described above, MRS signals provide chemical information while MRI provides spatial information. In many applications, it is necessary to obtain spectra from well localized regions of the body. Two approaches of spectral localization exist: one is known as sin-

gle voxel spectroscopy (SVS) and is based on the detection of the signal from a single well defined volume element (called voxel) of the human body; the second approach involves the simultaneous acquisition of signals from many volumes and is called MRSI or, equivalently, chemical shift imaging (CSI). The MRSI FIDs are arranged into a two-dimensional or three-dimensional array, typically with dimensions  $16 \times 16 \times 16$  or  $32 \times 32 \times 32$ .

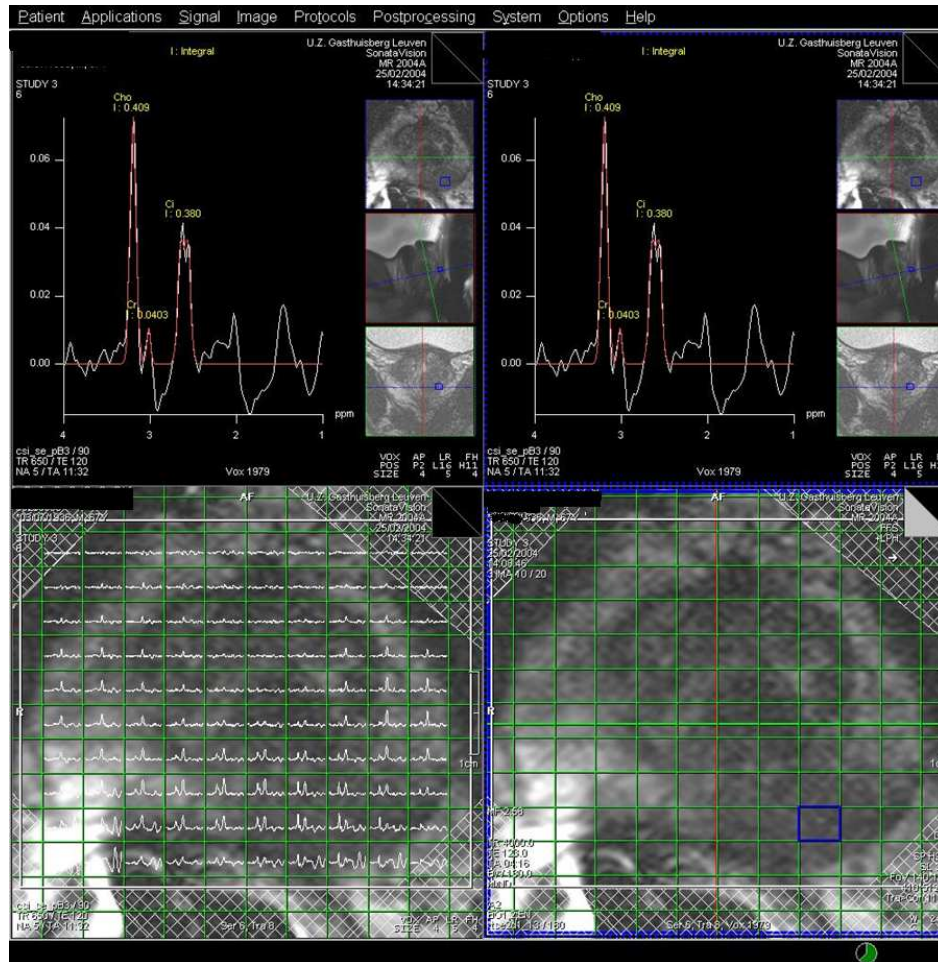
Both approaches make use of specific techniques which allow for the use of magnetic field gradients to obtain spatial information, but are also able to retain the required chemical information. These techniques are not discussed here and more background information can be found in ([17], [24]) and references therein.

Figure 1.6 shows a screenshot provided by a Siemens scanner for an *in vivo* example of MRSI data measured in the human prostate. The original data set is three-dimensional with dimensions  $16 \times 16 \times 16$ . The bottom part of the figure shows only one slice. This slice is the most interesting one since some of the spectra that can be observed in it are characteristic for tumor tissue. One example of these spectra is displayed in the upper part of the screenshot.

## 1.2 Clinical relevance of MRS and MRSI data for diagnosis and treatment of cancer

MRS and MRSI have been proved to play an important role in oncology. In particular, the analysis of this type of NMR data can be used as a non-invasive tool to detect and localize the presence of a tumor, to classify its nature, to study the tumor metabolism in order to evaluate the response to possible therapies, thereby helping clinicians to optimize the treatment.

A well known technique to detect the presence of a tumor is based on the estimation of the biochemically relevant metabolite concentrations. These values can be retrieved by estimating the areas under the peaks, corresponding to the considered metabolites, that occur in the spectrum of the MRS signal characterizing the voxel/voxels under investigation. For example, Figure 1.7 shows the magnitude spectra of two  $^1\text{H}$  signals. The signals were acquired at 1.5T in the human prostate of a patient affected by a tumor. As can be observed in the figure, the spectra are characterized by the presence of three metabolite peaks: choline (Cho), creatine (Cr) and citrate doublet (Citr). In general, aggressive tumor tissue (left-hand side spectrum) is characterized by a strong contribution of choline, while healthy tissue (right-hand side spectrum) exhibits a higher contribution of citrate. The increase of choline is attributed to an increase in cellular proliferation and cell density as well as to changes in phospholipid metabolism that result in higher levels of membrane synthesis and degradation products [52]. The decrease in citrate is due to changes in cellular function combined with the replacement of the tissue's characteristic ductal morphology [15]. Therefore, the ratio citrate-to-choline can be used as an indicator of the presence of a prostate tumor and of its grade of malignancy.



**Figure 1.6.** Screenshot provided by a Siemens scanner for an *in vivo* prostate MRSI data set.

Also brain tumors can be detected by studying alterations in the metabolite levels. In general, a brain tumor is present when N-acetyl-aspartate (NAA) and creatine levels are reduced, while choline levels are increased. In particular, NAA in the brain is commonly used as a marker of the neuronal density and, thus, reduced NAA levels may reflect neuronal dysfunction or loss [29]. Figure 1.8 shows the real part of the spectra of two  $^1\text{H}$  signals measured in the brain of a patient affected by a glioblastoma tumor. The spectrum on the left-hand side is characteristic of tumor tissue while the spectrum on the right-hand side is typical of healthy tissue.

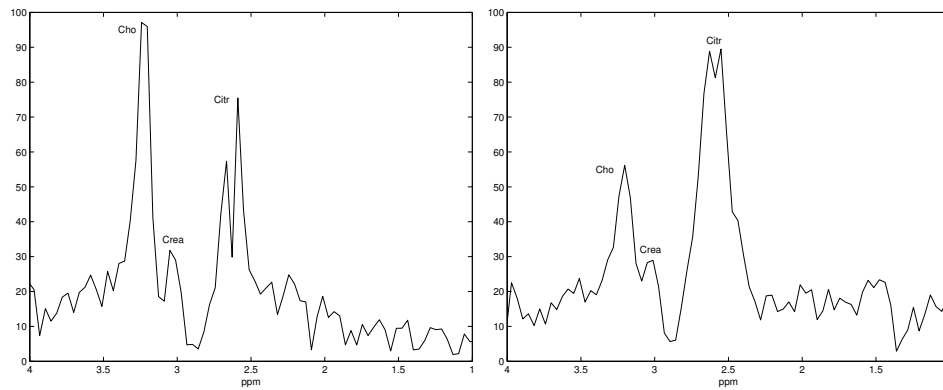


**Figure 1.7.** Magnitude spectra of characteristic  $^1\text{H}$  prostate signals. Three metabolites are visible: choline (Cho), creatine (Cr) and citrate (Citr). Left: moderately aggressive tumor tissue spectrum. Right: healthy tissue spectrum.

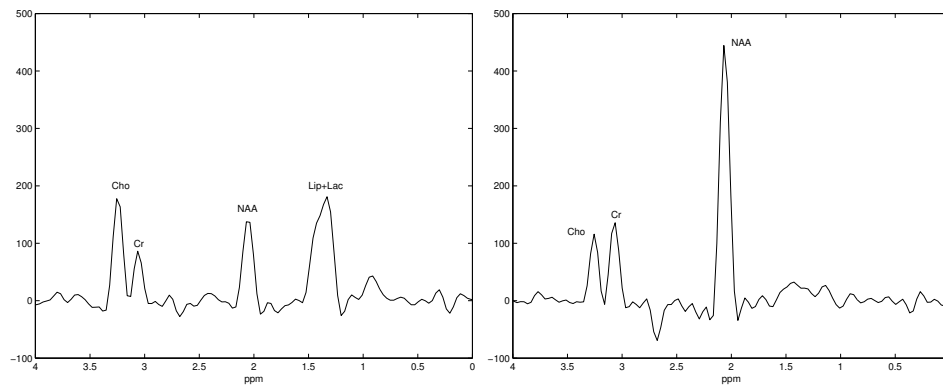


**Figure 1.8.** Real part of the spectra of characteristic  $^1\text{H}$  brain signals. Several metabolites are visible: choline (Cho), creatine (Cr), N-acetyl-aspartate (NAA) and lipids overlapping to lactate (Lip+Lac). Left: tumor tissue spectrum. Right: healthy tissue spectrum.

In particular, if MRSI data is considered, the concentrations of the relevant metabolites are determined for each voxel and are afterwards exploited in order to construct metabolite maps, in which a spatial distribution of the intensity of any relevant metabolite is visualized. The advantage of these images with respect to MRI images is quite clear: they provide spectroscopic as well as spatial information of the tissue, while MRI images only provide information about the water distribution in

the sample.

In conclusion, the success of MRS/MRSI as a diagnostic tool depends on the accurate estimation of the metabolite intensities characterizing the spectra. As described above, such estimates can be obtained by computing the areas under the corresponding peaks in the spectrum by using integration techniques. Unfortunately, this approach is not the most accurate one since the spectra are often characterized by overlapping peaks. More accurate estimation methods exist which make use of modeling the data in the time domain. A survey of the most significant time-domain algorithms available in the literature will be provided in Chapter 2. In addition to this type of application, MRSI data can also be exploited in tissue segmentation and classification techniques, without the need for computing the metabolite concentrations. Many algorithms are available in the literature and are based on a variety of theoretical principles. Some of them will be listed in Chapter 5 along with the corresponding references. Finally, the information contained in an MRSI data set can be summarized in a single image, called nosologic image, in which all the detected tissue types are visualized by means of different colors [62]. Such an image can be easily interpreted by radiologists and physicians and, along with clinical and radiological information, can improve the accuracy of the diagnosis.

### 1.3 Goals of the thesis

This thesis concerns two main topics: the development of accurate, robust and efficient algorithms for the quantification of time domain MRS signals, and for the tissue segmentation and classification of MRSI data. As already explained in the previous section, accurate results are of fundamental importance for a reliable diagnosis and for the choice of suitable therapies. Unfortunately, accuracy is not an easy property to obtain. In fact, *in vivo* MRS signals are usually characterized by poor SNRs, overlapping peaks and interfering signal components. In particular, in proton spectra the contribution of the water is very high compared to the metabolites of interest. The concentrations of e.g. NAA is of the order of  $1.5 \times 10^{-2}$  mM per gram of tissue compared to 55.5 mM per gram for water. In order to adequately digitize the signals from the metabolites of interest, it is common to suppress the water resonance by applying special RF pulses. However, it is impossible to completely suppress the water without affecting the metabolites of interest. Therefore, a water peak is always observed in the spectra of the measured signals, which needs to be further removed by applying specific techniques.

In order to improve the performance of the methods in terms of accuracy and robustness, biochemical prior knowledge that is often available when considering MRS/MRSI data, is exploited. Further, particular attention is paid to the performance of the algorithms in terms of efficiency since usually large amounts of data are processed and, in a clinical environment, the results of the data analysis need to be available as soon as possible. A more detailed description of the goals of this thesis are provided in the next section, where a chapter-by-chapter overview

is outlined.

## 1.4 Structure of the thesis

This thesis mainly consists of two parts. Chapters 2, 3 and 4 deal with the quantification of MRS signals, while chapters 5 and 6 deal with a new fast and accurate nosological imaging technique based on the use of a statistical method called canonical correlation analysis. More precisely:

- **Chapter 2** consists of an overview of a few but significant methods currently used by the NMR community to quantify individual MRS signals in the time domain. The overview includes:
  - the VARPRO and AMARES optimization methods. They require a lot of user expertise and interaction, but are very flexible with respect to the choice of the model function that is used to model the time-domain signal, and to the prior knowledge that can be imposed.
  - subspace-based methods. They are easier to use but are suboptimal since only limited prior knowledge can be imposed. In particular, the HSVD method and its improved variant HTLS will be described since their performance will be always compared to that of other quantification methods considered in this thesis.
  - subspace-based methods using prior knowledge. In this part of the chapter, some relevant subspace-based methods using prior knowledge will be described. In fact, recently several subspace-based algorithms have been developed that are able to exploit biochemical prior knowledge. Such methods are able to improve the accuracy and robustness compared to HSVD/HTLS, where no biochemical prior knowledge is imposed, although sometimes a higher computational load is required.
- **Chapter 3** deals with the use of the Lanczos algorithm in HSVD/HTLS. It is well known that the computationally most intensive part of the HSVD method is the computation of the truncated singular value decomposition (SVD) of a Hankel matrix. In order to reduce the computational load without affecting the accuracy of the parameters of interest, algorithms based on the Lanczos method are suitable. In the first part of the chapter the Lanczos algorithm will be described. Then, the performance in terms of accuracy and efficiency of four HSVD-based methods will be compared. Two of them are already available in the NMR literature: the first is based on the classical SVD algorithm which makes use of the QR decomposition; the second one is based on the Lanczos algorithm and is called HLSVD. In particular, the latter is very well known to the NMR community and widely used for solvent suppression

since it is implemented in a freely available software package called MRUI.

In this thesis we propose the use of two alternative HSVD-based methods, namely HLSVD-PRO and HLSVD-IRL, which are respectively based on the Lanczos algorithm with partial reorthogonalization and the implicitly restarted Lanczos algorithm. Extensive simulation studies show that the latter two algorithms perform best in terms of computational efficiency and numerical reliability. The results have been published in [35].

- **Chapter 4** is more focused on the use of prior knowledge in subspace-based methods. As already described above, including such knowledge significantly improves the accuracy of the parameter estimates and the robustness of the methods. Here a method is presented: KNOB-SVD, and its improved variant KNOB-TLS. This method allows the use of more prior knowledge about the signal parameters than previously published subspace-based methods. Its performance, in terms of accuracy and robustness, is compared with that of three commonly used methods that have been described in Chapter 2: the subspace-based methods HTLS and HTLSPK( $\Delta f d_{eq}$ ), and the optimization-based method AMARES. In particular, the second method, HTLSPK( $\Delta f d_{eq}$ ), is obtained by incorporating in HTLS the prior information that is available for some signal parameters. Extensive simulation and *in vivo* studies, using  $^{31}\text{P}$  as well as  $^1\text{H}$  MRS signals, will be reported. They show that the new method outperforms HTLS and HTLSPK( $\Delta f d_{eq}$ ) in robustness, accuracy and resolution, and that it provides parameter estimates comparable to the AMARES estimates. These results are published in [36].
- **Chapter 5** is devoted to the broad research topic of tissue segmentation and classification of MRSI data. In particular, an accurate and efficient technique for tissue typing is presented. It is based on Canonical Correlation Analysis (CCA), a statistical method able to simultaneously exploit the spectral and spatial information characterizing the MRSI data. Here, CCA is applied in order to retrieve in an accurate and efficient way the possible tissue types that characterize the sample under investigation. The potential and limitations of the new technique are investigated by using simulated as well as *in vivo* prostate MRSI data. Moreover, the performance of CCA is compared to that of ordinary correlation analysis. The test results show that CCA performs best in terms of accuracy and robustness. These results are published in [37].
- in **Chapter 6** a validation study is carried out about CCA. Different brain MRSI data sets are considered instead of prostate data. The data were acquired with two dimensional turbo-spectroscopic imaging sequences (2DTSI). In particular, all the data sets were measured in patients affected by a glioblastoma tumor. This type of tumor is very heterogeneous since different types of tissue can be present, such as cellular areas, necrotic areas, infiltrating lesions and, sometimes, areas of lower glioma tumor grades, as grade III. CCA is applied to this type of data in order to assess its ability to detect and classify

tissues even when a high degree of heterogeneity is present in the considered sample.

- in **Chapter 7** the main conclusions are formulated and the future research plans are described.

## **1.5 Conclusions**

In this chapter the theoretical principles of NMR were described. In particular, different NMR applications were illustrated, namely MRS, MRI and MRSI. The potential of such applications for clinical purposes was addressed in order to show how relevant the analysis of this type of data can be, and to introduce the reader to the main topics of this thesis. The specific goals were defined and, finally, the structure of the thesis was explained by means of a chapter-by-chapter overview.

# **QUANTIFICATION OF MRS SIGNALS: AN OVERVIEW OF TIME-DOMAIN METHODS**

*The purpose of this chapter is to provide a survey of some of the most significant time-domain parameter estimation methods that are available in the literature. More precisely, Section 2.1 introduces the so-called time-domain methods. In Section 2.2 the most important theoretical function used to model the measured signal is introduced. Section 2.3 illustrates the concept of biochemical prior knowledge and how this type of information is translated into mathematical relations between the model parameters. Section 2.4 is devoted to the optimization-based methods VARPRO and AMARES, while in Section 2.5 the subspace-based method called HSVD, along with its improved variant HTLS, is described. The last section of the chapter, Section 2.6, offers an overview of some subspace-based methods in which some types of prior knowledge are incorporated. Finally, Section 2.7 summarizes the main conclusions.*

## 2.1 Time-domain parameter estimation methods

The success of MRS depends on the quantitative data analysis, i.e., the interpretation of the signal in terms of relevant physical parameters, such as frequencies, decay constants and amplitudes. In fact, these parameters provide direct information about the sample under investigation: the frequency of the spectral components characterizes the identity of the molecules, the decay constant characterizes the mobility of the molecules, and the amplitude is directly proportional to the number of molecules. Therefore, accurate and efficient quantification of MRS signals is an essential step before converting the estimated signal parameters into biochemical quantities (concentrations, pH).

A variety of advanced techniques to extract parameters, based on time-domain model functions, have been developed. On one hand, interactive methods exist. They are optimization-based methods, require user involvement, and allow inclusion of prior knowledge. On the other hand, there are so-called subspace-based algorithms. Minimal user interaction and limited incorporation of prior knowledge are inherent to this type of methods.

## 2.2 Theoretical model of the MRS signal

The function often used to model the measured data points of an MRS signal is the sum of  $K$  exponentially damped complex sinusoids

$$y_n = \bar{y}_n + e_n = \sum_{k=1}^K a_k e^{j\phi_k} e^{(-d_k + j2\pi f_k)t_n} + e_n, \quad n = 0, \dots, N-1, \quad (2.2.1)$$

where  $y_n$  is the  $n$ th measured data point,  $\bar{y}_n$  represents the model function rather than the actual measurement,  $j = \sqrt{-1}$ ,  $a_k$  is the amplitude,  $\phi_k$  is the phase,  $d_k$  the decay constant, known as damping factor, and  $f_k$  the frequency of the  $k$ th sinusoid ( $k = 1, \dots, K$ ),  $K$  is the number of sinusoids,  $t_n = n\Delta t + t_0$  with  $\Delta t$  the

sampling period,  $t_0$  the time between the effective time origin and the first data point to be included into the analysis, and  $e_n$  is complex white noise with a circular Gaussian distribution, which means that the real and imaginary parts of the noise are uncorrelated and have equal variances. In particular, the phase  $\phi_k$  consists of a so-called zero-order phase and an additional phase factor  $\phi'_k$ , usually equal to zero, which represents extra degrees of freedom that may be required under certain experimental conditions.

Alternative model functions are available, such as the Gaussian model

$$y_n = \sum_{k=1}^K a_k e^{j\phi_k} e^{(-g_k t_n + j2\pi f_k)t_n} + e_n, \quad n = 0, \dots, N-1, \quad (2.2.2)$$

and the Voigt model [40]

$$y_n = \sum_{k=1}^K a_k e^{j\phi_k} e^{(-d_k - g_k t_n + j2\pi f_k)t_n} + e_n, \quad n = 0, \dots, N-1, \quad (2.2.3)$$

but they will not be considered in this thesis.

## 2.3 Biochemical Prior Knowledge

As already described, the potential of MRS as a non-invasive medical diagnostic tool depends on the accurate estimation of the signal parameters. Unfortunately, *in vivo* signals are often characterized by distortions with respect to the model function. These distortions are normally due to a low SNR, and to the presence of unwanted components and highly overlapping peaks. However, the relations among the resonance frequencies, amplitudes, and damping factors of multiplet components are usually known and by imposing such relations, the Cramer-Rao Bounds (CRBs) [59], which indicate the best possible accuracy achievable by any unbiased estimator, on the errors of estimated parameters are reduced ([7],[8]).

This prior knowledge can in some cases be derived from the spin properties. An example is the adenosine triphosphate (ATP) signal. This consists of three phosphorus atoms,  $P_\alpha$ ,  $P_\beta$  and  $P_\gamma$ , which experience a different chemical/electrical environment and thus a different shielding. As a consequence, the three atoms resonate at slightly different resonances, giving rise to three groups of spectral lines in the spectrum (Figure 2.1). Moreover, as a result of the spin-spin coupling between the neighboring phosphorus nuclei, the groups corresponding to the  $\alpha$  and  $\gamma$  phosphates contain two peaks (doublets), while the  $\beta$  phosphate group consists of three peaks (triplet).

Specific relations between the signal parameters can be derived from the spin properties, namely:

- the frequency differences between the individual resonances within a multiplet are equal and known:  $f_1 - f_2 = f_3 - f_4 = f_5 - f_6 = f_6 - f_7 = \Delta f$ ;

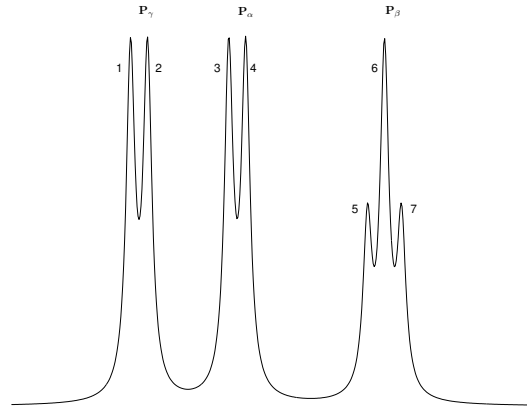


**Figure 2.1.** Theoretical spectrum of ATP. Three multiplets can be observed corresponding to the  $P_\alpha$ ,  $P_\beta$  and  $P_\gamma$  atoms.

- the damping factors of the peaks are all equal:  $d_1 = d_2 = d_3 = d_4 = d_5 = d_6 = d_7$ ;
- the phases of the peaks are all equal:  $\phi_1 = \phi_2 = \phi_3 = \phi_4 = \phi_5 = \phi_6 = \phi_7$ ;
- the amplitudes of the doublet peaks and of the central peak of the  $P_\beta$  group are equal, while the outer peaks of  $P_\beta$  are half the amplitude of the central peak. More precisely:  $a_1 = a_2 = a_3 = a_4 = 2a_5 = a_6 = 2a_7$ .

An alternative procedure to obtain prior knowledge consists of measuring *in vitro* signals in the same experimental conditions as the *in vivo* experiment. The relations among the signal parameters are then retrieved from the *in vitro* spectra, since they are typically characterized by a high SNR and contain more spectral components. In fact, *in vitro* signals are MRS signals obtained from body fluids, cells, tissue extracts, etc., dissolved in water and measured in small sample tubes. Therefore, there are no limitations on the measurement time. Moreover, higher magnetic field strengths can be applied and the local field inhomogeneities, that normally characterize *in vivo* signals, no longer occur. For more details, the reader is referred to [18].

## 2.4 Optimization-based methods: VARPRO, AMARES and AQSES

When an MRS signal is modelled by Eq.(2.2.1), the signal parameters can be estimated by applying a well known Maximum Likelihood based method called VARIable PROjection (VARPRO) ([26],[64]). The model problem consists of minimizing the squared difference between the measured data points  $\mathbf{y} = [y_0, \dots, y_{N-1}]^T$  and

the model data points  $\bar{\mathbf{y}} = [\bar{y}_0, \dots, \bar{y}_{N-1}]^T$ , where the superscript  $T$  denote transpose. This is a nonlinear least-squares problem (NLLS) that can be formulated in vector notation as

$$\min \|\mathbf{y} - \bar{\mathbf{y}}\|^2, \quad (2.4.4)$$

where  $\|\cdot\|$  denotes the Euclidean vector norm.

In order to apply VARPRO, the model function  $\bar{y}_n$  used in Eq.(2.2.1) is reformulated as follows

$$\bar{y}_n = \sum_{k=1}^K c_k \gamma_k(\boldsymbol{\alpha}_k, n), \quad n = 0, \dots, N-1, \quad (2.4.5)$$

where  $c_k = a_k e^{j\phi_k}$  are the complex amplitudes and  $\gamma_k(\boldsymbol{\alpha}_k, n) = e^{(-d_k + j2\pi f_k)t_n}$  are nonlinear functions of the parameter vector  $\boldsymbol{\alpha}_k = [f_k \ d_k \ t_0]^T$ . Using the matrix notation, Eq.(2.4.5) becomes

$$\bar{\mathbf{y}} = \mathbf{\Gamma} \mathbf{c}, \quad (2.4.6)$$

with  $\mathbf{c} = [c_1, \dots, c_K]^T$  and

$$\mathbf{\Gamma} = \begin{bmatrix} \gamma_1(\boldsymbol{\alpha}_1, 0) & \cdots & \gamma_K(\boldsymbol{\alpha}_K, 0) \\ \vdots & \ddots & \vdots \\ \gamma_1(\boldsymbol{\alpha}_1, N-1) & \cdots & \gamma_K(\boldsymbol{\alpha}_K, N-1) \end{bmatrix}, \quad (2.4.7)$$

an  $N \times K$  matrix of full rank.

Eq.(2.4.4), which needs to be minimized, can then be reformulated as

$$\min \|\mathbf{y} - \mathbf{\Gamma} \mathbf{c}\|^2. \quad (2.4.8)$$

In order to estimate the linear parameters  $c_k$  and the nonlinear parameters  $\boldsymbol{\alpha}_k$  ( $k = 1, \dots, K$ ), VARPRO amounts to temporarily assuming that the nonlinear parameters, present in the  $\mathbf{\Gamma}$  matrix, are known. In that case, the linear parameters can be expressed as the solution of a linear least-squares problem (LS), namely

$$\hat{\mathbf{c}} = (\mathbf{\Gamma}^H \mathbf{\Gamma})^{-1} \mathbf{\Gamma}^H \mathbf{y}, \quad (2.4.9)$$

where the superscript  $H$  denotes the Hermitian conjugate.

The cost function of Eq.(2.4.8) then becomes

$$\|\mathbf{y} - \mathbf{\Gamma}(\mathbf{\Gamma}^H\mathbf{\Gamma})^{-1}\mathbf{\Gamma}^H\mathbf{y}\|^2 = \|\mathbf{P}_{\mathbf{\Gamma}}^{\perp}\mathbf{y}\|^2, \quad (2.4.10)$$

where  $\mathbf{P}_{\mathbf{\Gamma}}^{\perp}$  is a projection operator on the column space of  $\mathbf{\Gamma}$ . This new cost function contains only the nonlinear parameters whose estimates,  $\hat{\boldsymbol{\alpha}}_k$ , are obtained as the parameters that minimize Eq.(2.4.10). Using  $\hat{\boldsymbol{\alpha}}_k$ , the matrix  $\hat{\mathbf{\Gamma}}$  is computed and the estimates of the linear parameters  $c_k$  are obtained as the LS solution of the system

$$\hat{\mathbf{\Gamma}}\mathbf{c} \approx \mathbf{y}. \quad (2.4.11)$$

The NLLS problem described above can be solved by using global optimization methods. Unfortunately, these methods are computationally inefficient. Local optimization algorithms are more efficient, but they provide a local minimum, instead of the global one. The problem can be overcome by providing good starting values, which are normally obtained by applying a procedure, called peak picking. This technique consists of retrieving rough estimates of the frequencies and damping factors from the frequency domain by a visual inspection, thereby requiring a lot of user interaction and expertise. In order to reduce the need for interaction, subspace-based parameter estimation methods can be used to estimate reliable starting values.

Specifically, in VARPRO the optimization problem is solved by applying a modified version of the Levenberg–Marquardt algorithm [44].

Nowadays, an improved version of VARPRO exists and is called AMARES (Advanced Method for Accurate, Robust and Efficient Spectral fitting) [65]. AMARES computes the signal parameters by minimizing a general functional consisting of the sum of the squared differences between the data and the model function (see (2.4.4)), instead of minimizing the variable projection functional (see (2.4.10)) that is used in VARPRO.

The *dn2gb* routine is used to minimize the general functional. This routine is the most recent version of the NL2SOL algorithm ([19],[20]), which combines approaches used in Gauss–Newton and quasi–Newton methods. AMARES outperforms VARPRO in terms of efficiency, accuracy and robustness since more types of prior knowledge can be incorporated, and upper and lower bounds can be imposed. Moreover, it allows the use of two different theoretical model functions, namely the Lorentzian (defined by Eq.(2.2.1)) and the Gaussian.

AMARES has also been extended to the processing of time-series. It is well-known that, in biochemical studies, MRS signals are often acquired consecutively to monitor metabolic changes over time. Often relations between the different spectra are present and these can be expressed as relations between the corresponding parameters. This means that information concerning the time evolution of some of the parameters is available and this can be easily included in the algorithm, thereby further improving the robustness and accuracy of the estimation. This extension of

AMARES is called  $\text{AMARES}_{t_s}$ .

Furthermore, another variant of AMARES, which is called  $\text{AMARES}_f$ , deserves to be mentioned here. The latter algorithm consists of combining AMARES with an FIR filter in order to process filtered signals. In fact, generally spectra contain unknown or uninteresting spectral features separated in frequency from the metabolites of interest. Such unwanted components can be removed by applying an FIR filter and the filtered signal can afterwards be estimated by using any parameter estimation method. It is proved that  $\text{AMARES}_f$  is easy to use, has a low computational complexity and is able to keep the bias and the standard deviation of the parameters of interest small.

For further details on  $\text{AMARES}_{t_s}$  and  $\text{AMARES}_f$  the reader is referred to [66] and [68], respectively.

Recently, a new optimization-based method has been developed in order to quantify short echo time signals. The new method is called AQSES (Accurate Quantification of Short Echo time domain Signals) and is available on line, under an Open-Source license, from: <http://www.esat.kuleuven.be/sista/members/biomed/new/>.

As already explained in Section 1.1, short echo time signals significantly differ from long echo time signals. In fact, they contain many more peaks, highly overlapping, and the so-called baseline which consists of disturbing underlying broad resonances due to macromolecules and lipids. Therefore, a suitable theoretical model is needed which is able to take into account all these additional factors characterizing the spectra. To this aim, a “metabolite database”, consisting of a set of  $K$  complex-valued time series  $v_k$ ,  $k = 1, \dots, K$ , is needed. These vectors represent *in vitro* measured MRS metabolite signals. The short echo time signal is then modelled as follows

$$y_n = \hat{y}_n + e_n = \sum_{k=1}^K a_k e^{j\phi_k} e^{(-d_k + j2\pi f_k)t_n} v_k(n) + b(n) + e_n, \quad n = 0, \dots, N-1,$$

where the term  $b(n)$  represents the baseline and is modelled as a linear combination of spline functions. Moreover, a maximum phase FIR filter is implemented in the algorithm that allows for the removal of disturbing components, such as the water resonance.

The signal parameters are estimated by minimizing a regularized nonlinear least squares criterion in order to fit the model and a smooth baseline at the same time. In ([54],[56]) it is proved that the method is robust and accurate and, although designed to quantify short echo time signals, it can be easily adapted to process long echo time signals.

Other algorithms for short echo time data quantification exist, such as LCModel and QUEST, but they are not described in this thesis. The reader is referred to [47] and [48] and references therein.

## 2.5 Subspace-based methods: HSVD

HSVD is a subspace-based parameter estimation method in which the noisy signal is arranged in a Hankel matrix  $\mathbf{H}$ . Its Singular Value Decomposition (SVD) allows to compute a “signal” subspace and a “noise” subspace. In fact, if  $\mathbf{H}$  is constructed from a noiseless time-domain signal, the data matrix  $\mathbf{H}$  has rank exactly equal to  $K$ , the number of exponentials that model the underlying signal. Due to the presence of the noise,  $\mathbf{H}$  becomes a full-rank matrix. However, as long as the SNR of the signal is not too low, one can still define the “numerical” rank being approximately equal to  $K$ . Then, the “signal” subspace is found by truncating the SVD of the matrix  $\mathbf{H}$  to rank  $K$ .

In the following subsections, the method will be derived in the context of linear algebra.

### 2.5.1 HSVD - noiseless data

Arrange the  $N$  noiseless data points  $\bar{y}_n$  defined in Eq.(2.2.1) in a Hankel matrix  $\bar{\mathbf{H}}$  of dimensions  $L \times M$ , with  $L$  and  $M$  greater than  $K$  and  $N = L + M - 1$

$$\bar{\mathbf{H}} = \begin{bmatrix} \bar{y}_0 & \bar{y}_1 & \cdots & \bar{y}_{M-1} \\ \bar{y}_1 & \bar{y}_2 & \cdots & \bar{y}_M \\ \vdots & \vdots & \ddots & \vdots \\ \bar{y}_{L-1} & \bar{y}_L & \cdots & \bar{y}_{N-1} \end{bmatrix}. \quad (2.5.12)$$

The model of Eq.(2.2.1), in which  $t_0 = 0$  is assumed, can be rewritten in terms of complex amplitudes  $c_k$  and signal poles  $z_k$  as follows

$$\bar{y}_n = \sum_{k=1}^K a_k e^{j\phi_k} e^{(-d_k + j2\pi f_k)n\Delta t} = \sum_{k=1}^K c_k z_k^n, \quad n = 0, \dots, N-1, \quad (2.5.13)$$

where  $c_k = a_k e^{j\phi_k}$  and  $z_k = e^{(-d_k + j2\pi f_k)\Delta t}$ . Using this model function, the Hankel matrix  $\bar{\mathbf{H}}$  can be factorized as follows

$$\begin{aligned} \bar{\mathbf{H}} &= \begin{bmatrix} 1 & 1 & \cdots & 1 \\ z_1 & z_2 & \cdots & z_K \\ \vdots & \vdots & \ddots & \vdots \\ z_1^{L-1} & z_2^{L-1} & \cdots & z_K^{L-1} \end{bmatrix} \begin{bmatrix} c_1 & 0 & \cdots & 0 \\ 0 & c_2 & \cdots & 0 \\ \vdots & \vdots & \ddots & \vdots \\ 0 & 0 & \cdots & c_K \end{bmatrix} \begin{bmatrix} 1 & 1 & \cdots & 1 \\ z_1 & z_2 & \cdots & z_K \\ \vdots & \vdots & \ddots & \vdots \\ z_1^{M-1} & z_2^{M-1} & \cdots & z_K^{M-1} \end{bmatrix}^T \\ &= \bar{\mathbf{S}}\bar{\mathbf{C}}\bar{\mathbf{T}}^T \end{aligned} \quad (2.5.14)$$

This factorization is called Vandermonde decomposition and from it the signal parameters can immediately be derived. Unfortunately, there is no algorithm that computes such a decomposition directly and, therefore, the parameters need to be

computed indirectly.

From Eq.(2.5.14) it can be easily proved that the matrix  $\bar{\mathbf{S}}$  satisfies the so-called shift-invariance property, i.e.

$$\bar{\mathbf{S}}^\dagger = \bar{\mathbf{S}}_\downarrow \bar{\mathbf{Z}} \quad (2.5.15)$$

where  $\bar{\mathbf{S}}^\dagger$  and  $\bar{\mathbf{S}}_\downarrow$  are derived from  $\bar{\mathbf{S}}$  by deleting its first and last row respectively, and  $\bar{\mathbf{Z}}$  is a  $K \times K$  complex diagonal matrix with entries equal to the  $K$  signal poles  $z_k$ ,  $k = 1, \dots, K$ . The rank of the matrix  $\bar{\mathbf{H}}$  is equal to  $K$  and, thus, its SVD has the following form

$$\bar{\mathbf{H}} = \bar{\mathbf{U}} \bar{\mathbf{\Sigma}} \bar{\mathbf{V}}^H = [\bar{\mathbf{U}}_K \ \bar{\mathbf{U}}_2] \begin{bmatrix} \bar{\mathbf{\Sigma}}_K & \mathbf{0} \\ \mathbf{0} & \mathbf{0} \end{bmatrix} [\bar{\mathbf{V}}_K \ \bar{\mathbf{V}}_2]^H = \bar{\mathbf{U}}_K \bar{\mathbf{\Sigma}}_K \bar{\mathbf{V}}_K^H, \quad (2.5.16)$$

where  $\bar{\mathbf{U}}_K \in \mathbb{C}^{L \times K}$ ,  $\bar{\mathbf{U}}_2 \in \mathbb{C}^{L \times (L-K)}$ ,  $\bar{\mathbf{\Sigma}}_K \in \mathbb{C}^{K \times K}$ ,  $\bar{\mathbf{V}}_K \in \mathbb{C}^{M \times K}$ ,  $\bar{\mathbf{V}}_2 \in \mathbb{C}^{M \times (M-K)}$ . From the comparison of Eq.(2.5.14) and Eq.(2.5.16), it follows that  $\bar{\mathbf{S}}$  and  $\bar{\mathbf{U}}_K$  span the same column space and hence are equal up to a multiplication by a non singular matrix  $\bar{\mathbf{Q}} \in \mathbb{C}^{K \times K}$ , i.e.

$$\bar{\mathbf{U}}_K = \bar{\mathbf{S}} \bar{\mathbf{Q}}. \quad (2.5.17)$$

Using Eq.(2.5.17), the shift-invariance property of Eq.(2.5.15) becomes

$$\bar{\mathbf{U}}_K^\dagger = \bar{\mathbf{U}}_{K\downarrow} \bar{\mathbf{Q}}^{-1} \bar{\mathbf{Z}} \bar{\mathbf{Q}}. \quad (2.5.18)$$

From Eq.(2.5.18) the matrix  $\bar{\mathbf{Q}}^{-1} \bar{\mathbf{Z}} \bar{\mathbf{Q}}$  can be determined and since the eigenvalues of  $\bar{\mathbf{Q}}^{-1} \bar{\mathbf{Z}} \bar{\mathbf{Q}}$  and  $\bar{\mathbf{Z}}$  are equal, the signal poles are easily derived as

$$\{z_k\}_{k=1}^K = \text{eig}(\bar{\mathbf{Q}}^{-1} \bar{\mathbf{Z}} \bar{\mathbf{Q}}) = \text{eig}(\bar{\mathbf{Z}}), \quad (2.5.19)$$

where the function  $\text{eig}(\cdot)$  determines the eigenvalues of the matrix between brackets. From the signal poles, frequency and damping factors are estimated. By filling in these estimates into the model function Eq.(2.5.13), a new system of linear equations is obtained with unknowns equal to the complex amplitudes  $c_k$ . Its solution provides estimates for the amplitudes and the phases.

Note that, once the signal poles have been estimated, the amplitudes and phases can be obtained by using other estimation methods. One example is the so-called APES method, where the acronym stands for Amplitude and Phase ESTimation, which provides accurate estimates at a reasonable computational cost as shown in [60] and [61].

### 2.5.2 HSVD - noisy data

When noise affects the data, as in real MRS signals, the noisy Hankel matrix  $\mathbf{H}$  replaces  $\bar{\mathbf{H}}$  and the relation (2.5.16) no longer holds. Although no exact solution of the shift-invariance property exists, the matrices  $\mathbf{H}$  and  $\bar{\mathbf{H}}$  have the same structure and, if the noise is small compared to the signal,  $\mathbf{H}$  can be approximated by the truncated SVD, i.e.

$$\mathbf{H} = \mathbf{U}\mathbf{\Sigma}\mathbf{V}^H \approx \mathbf{U}_K\mathbf{\Sigma}_K\mathbf{V}_K^H = \mathbf{H}_K, \quad (2.5.20)$$

where  $\mathbf{U}_K$  and  $\mathbf{V}_K$  are the first  $K$  columns of  $\mathbf{U}$  and  $\mathbf{V}$ , respectively, and  $\mathbf{\Sigma}_K$  is the  $K \times K$  upper-left sub-matrix of  $\mathbf{\Sigma}$ .

The matrix  $\mathbf{H}_K$  has rank  $K$  but its Hankel structure has been destroyed by the truncation of the SVD. Therefore, the system in Eq.(2.5.18) has no longer an exact solution. However, estimates of the signal poles can still be obtained by solving the aforementioned system in a LS sense and the signal parameters can be derived from such estimates as in the noiseless case. Further details about the derivation of HSVD can be found in ([2],[33]).

### 2.5.3 HTLS

The performance of HSVD can be improved by making use of the total least squares (TLS) technique instead of the LS technique, in solving the overdetermined set of equations occurring in Eq.(2.5.18). This variant is called HTLS [71] in the MRS literature and it possesses good resolution, parameter accuracy and efficiency. Specifically, the TLS solution of the system in Step 4 is given by

$$\hat{\mathbf{E}} = -\hat{\mathbf{V}}_{12}\hat{\mathbf{V}}_{22}^{-1}, \quad (2.5.21)$$

provided  $\hat{\mathbf{V}}_{22}$  is nonsingular. The matrices  $\hat{\mathbf{V}}_{12}$  and  $\hat{\mathbf{V}}_{22}$  are obtained from the SVD of the augmented data matrix

$$\left[ \mathbf{U}_{K\downarrow} \quad \mathbf{U}_K^\uparrow \right] = \hat{\mathbf{U}}_{L \times L} \hat{\mathbf{\Sigma}} \hat{\mathbf{V}}_{2K \times 2K}^H, \quad (2.5.22)$$

with

$$\hat{\mathbf{V}} = \begin{bmatrix} \hat{\mathbf{V}}_{11} & \hat{\mathbf{V}}_{12} \\ \hat{\mathbf{V}}_{21} & \hat{\mathbf{V}}_{22} \end{bmatrix}. \quad (2.5.23)$$

Other improved variants of HSVD exist and are based on the use of Cadzow's method or minimum variance estimation as preprocessing techniques, as explained in [10].

An outline of the algorithms HSVD and HTLS is provided here for the sake of clarity.

### Outline of the HSVD/HTLS algorithm

- **Step 1 :**

Arrange the  $N$  data points  $y_n$ ,  $n = 0, \dots, N - 1$ , in a Hankel matrix  $\mathbf{H}$  of dimensions  $L \times M$ , with  $N = L + M - 1$

$$\mathbf{H} = \begin{bmatrix} y_0 & y_1 & \cdots & y_{M-1} \\ y_1 & y_2 & \cdots & y_M \\ \vdots & \vdots & \vdots & \vdots \\ y_{L-1} & y_L & \cdots & y_{N-1} \end{bmatrix}$$

- **Step 2 :**

Compute the SVD of the Hankel matrix  $\mathbf{H}$

$$\mathbf{H}_{L \times M} = \mathbf{U}_{L \times L} \mathbf{\Sigma}_{L \times M} \mathbf{V}_{M \times M}^H$$

where  $\mathbf{\Sigma} = \text{diag}(\sigma_1, \sigma_2, \dots, \sigma_q)$ ,  $\sigma_1 \geq \sigma_2 \geq \dots \geq \sigma_q$ ,  $q = \min(L, M)$ ,  $\mathbf{U}^H \mathbf{U} = \mathbf{U} \mathbf{U}^H = \mathbf{I}$  and  $\mathbf{V}^H \mathbf{V} = \mathbf{V} \mathbf{V}^H = \mathbf{I}$  contain respectively the left and right singular vectors. According to [9],  $\mathbf{H}$  should be chosen as square as possible in order to get the best parameter accuracy.

- **Step 3 :**

Truncate  $\mathbf{H}$  to a matrix  $\mathbf{H}_K$  of rank  $K$

$$\mathbf{H}_K = \mathbf{U}_K \mathbf{\Sigma}_K \mathbf{V}_K^H,$$

where  $\mathbf{U}_K$  and  $\mathbf{V}_K$  are the first  $K$  columns of  $\mathbf{U}$  and  $\mathbf{V}$ , respectively,  $\mathbf{\Sigma}_K$  is the  $K \times K$  upper-left sub-matrix of  $\mathbf{\Sigma}$ .

- **Step 4 :**

Compute the LS solution (HSVD) or TLS (HTLS) solution  $\hat{\mathbf{E}}$  of the following overdetermined set of equations

$$\mathbf{U}_{K\downarrow} \hat{\mathbf{E}} \approx \mathbf{U}_K^\uparrow$$

where  $\mathbf{U}_{K\downarrow}$  and  $\mathbf{U}_K^\uparrow$  are derived from  $\mathbf{U}_K$  by deleting its last and first row respectively.

- **Step 5 :**

The  $K$  eigenvalues of  $\widehat{\mathbf{E}}$  yield the signal pole estimates

$$\hat{z}_k = e^{(-\hat{d}_k + j2\pi\hat{f}_k)\Delta t} \quad k = 1, \dots, K,$$

from which estimates for  $\hat{f}_k$  and  $\hat{d}_k$  are found.

- **Step 6 :**

Filling in the estimated frequencies  $\hat{f}_k$  and damping factors  $\hat{d}_k$  into the model equation (2.5.13), yields the set of equations in the complex amplitudes  $c_k$

$$y_n \approx \sum_{k=1}^K c_k e^{(-\hat{d}_k + j2\pi\hat{f}_k)t_n} \quad n = 0, 1, \dots, N-1.$$

From its LS solution  $\hat{c}_k = \hat{a}_k e^{j\hat{\phi}_k}$ , we find  $\hat{a}_k$  and  $\hat{\phi}_k$ , the estimated amplitudes and phases.

## 2.6 Subspace-based methods using biochemical prior knowledge

Several advantages characterize HSVD and HTLS: the signal parameters are computed in one step, no starting values are needed and, hence, minimal user interaction is required. On the other hand, they are statistically suboptimal under the noise assumptions made. Moreover, they do not exploit any prior knowledge about parameters in the data model, whose inclusion is important for further improvement of estimation accuracy and resolution.

More accurate and robust subspace-based methods have been developed by incorporating different types of prior knowledge (PK) in HTLS, such as:

- HTLSPK(fd): frequencies and damping factors of some exponentials are known ([11], [12]);
- HTLSPK(fp): frequencies and phases of some exponentials are known [13];
- HTLSPK(fdp): frequencies, dampings and phases of some exponentials are known [13];
- HTLSPK(p): phases of some exponentials are known [13];
- HTLSPK( $\Delta fd_{eq}$ ): the frequency differences between doublet components are known and the damping factors are equal ([70], [72]).

Below a short outline of these methods is provided.

### 2.6.1 HTLSPK(fd)

In HTLSPK(fd) the frequencies and damping factors of some exponentials are assumed to be known. This type of prior knowledge is equivalent to the following: some signal poles  $z_k$ ,  $k = 1, \dots, p$ , with  $p < K$ , are known, while the poles  $z_k$ ,  $k = p + 1, \dots, K$ , are unknown. Hence, in the Vandermonde decomposition of the matrix  $\bar{\mathbf{H}}$ , Eq.(2.5.14), the first  $p$  columns,  $\bar{\mathbf{S}}_p$  and  $\bar{\mathbf{T}}_p$ , of the matrices  $\bar{\mathbf{S}}$  and  $\bar{\mathbf{T}}$  are known a priori. If noiseless data are considered, the known part in Eq.(2.5.14) can be removed by means of a QR decomposition [25] of  $\bar{\mathbf{T}}_p$

$$\bar{\mathbf{T}}_p = [ \mathbf{Q}_{known} \quad \mathbf{Q}_{orth} ] [ \mathbf{R}^T \quad \mathbf{0} ]^T \quad (2.6.24)$$

and a projection of  $\bar{\mathbf{H}}$  onto the orthogonal subspace

$$\begin{aligned} \tilde{\mathbf{H}} &= \bar{\mathbf{H}}\mathbf{Q}_{orth}^H = [\bar{\mathbf{S}}_p \quad \bar{\mathbf{S}}_{K-p}] \begin{bmatrix} \bar{\mathbf{C}}_p & \mathbf{0} \\ \mathbf{0} & \bar{\mathbf{C}}_{K-p} \end{bmatrix} [\bar{\mathbf{T}}_p \quad \bar{\mathbf{T}}_{K-p}]^T \mathbf{Q}_{orth}^H \quad (2.6.25) \\ &= \bar{\mathbf{S}}_{K-p} \bar{\mathbf{C}}_{K-p} \bar{\mathbf{T}}_{K-p}^T \mathbf{Q}_{orth}^H, \end{aligned}$$

where  $\text{rank}(\bar{\mathbf{H}}) = K$  and  $\text{rank}(\tilde{\mathbf{H}}) = K - p$ . The matrix  $[\mathbf{Q}_{known} \quad \mathbf{Q}_{orth}]$  is unitary, with  $\mathbf{Q}_{known} \in \mathbb{C}^{M \times p}$ ,  $\mathbf{Q}_{orth} \in \mathbb{C}^{M \times (M-p)}$ , and  $\mathbf{R} \in \mathbb{C}^{p \times p}$  is upper triangular. Note that multiplication of  $\bar{\mathbf{H}}$  with  $\mathbf{Q}_{orth}^H$  from the right destroys the shift-invariance property in the row space but keeps the shift-invariance property in the column space, i.e.

$$\bar{\mathbf{S}}_{K-p} \downarrow \bar{\mathbf{Z}}_{K-p} = \bar{\mathbf{S}}_{K-p}^\dagger, \quad (2.6.26)$$

where  $\bar{\mathbf{Z}}_{K-p}$  is a diagonal matrix with diagonal elements equal to the  $K-p$  unknown signal poles. The unknown signal poles are obtained by computing the SVD of the matrix  $\tilde{\mathbf{H}}$ , i.e.

$$\tilde{\mathbf{H}} = \tilde{\mathbf{U}}_{K-p} \tilde{\mathbf{\Sigma}}_{K-p} \tilde{\mathbf{V}}_{K-p}^H, \quad (2.6.27)$$

where  $\tilde{\mathbf{U}}_{K-p}$ ,  $\tilde{\mathbf{\Sigma}}_{K-p}$ ,  $\tilde{\mathbf{V}}_{K-p}$  respectively contain the first  $K-p$  left singular vectors, singular values and right singular vectors. By equating Eq.(2.6.6) with (2.6.25), the shift-invariance property still holds

$$\tilde{\mathbf{U}}_{K-p} \downarrow \bar{\mathbf{Z}}_{K-p}^{(\tilde{\mathbf{U}})} = \tilde{\mathbf{U}}_{K-p}^\dagger, \quad (2.6.28)$$

where  $\bar{\mathbf{Z}}_{K-p}^{(\tilde{\mathbf{U}})}$  is a similarity transform of  $\bar{\mathbf{Z}}_{K-p}$ . The eigenvalues of  $\bar{\mathbf{Z}}_{K-p}^{(\tilde{\mathbf{U}})}$  yield the unknown signal poles and the linear parameters are found in the same way as in the HTLS method.

## 2.6.2 HTLSPK(fp)

In HTLSPK(fp) the following assumption is made: the frequency  $f_{\hat{k}}$  and the phase  $\phi_{\hat{k}}$  of the  $\hat{k}$ th exponential are known. When this type of prior knowledge is available, it is possible to perform a shifting in frequency and phase of the whole spectrum such that the  $\hat{k}$ th exponential is shifted to zero frequency and zero phase. More precisely, from the model function of Eq.(2.2.1), it follows

$$\begin{aligned}\hat{y}_n &= y_n e^{-j(2\pi f_{\hat{k}} n\Delta t + \phi_{\hat{k}})} \\ &= \sum_{k=1}^K a_k e^{j(\phi_k - \phi_{\hat{k}})} e^{-d_k n\Delta t + j2\pi(f_k - f_{\hat{k}})n\Delta t} \\ &= \hat{y}_{nr} + j\hat{y}_{ni},\end{aligned}\quad (2.6.29)$$

where the subscripts “ $nr$ ” and “ $ni$ ” denote the real and imaginary part, respectively. More precisely, these are equal to

$$\hat{y}_{nr} = a_{\hat{k}} e^{-d_{\hat{k}} n\Delta t} + \sum_{k=1, k \neq \hat{k}}^K a_k e^{-d_k n\Delta t} \cos(2\pi(f_k - f_{\hat{k}})n\Delta t + (\phi_k - \phi_{\hat{k}})), \quad (2.6.30)$$

$$\hat{y}_{ni} = \sum_{k=1, k \neq \hat{k}}^K a_k e^{-d_k n\Delta t} \sin(2\pi(f_k - f_{\hat{k}})n\Delta t + (\phi_k - \phi_{\hat{k}})), \quad (2.6.31)$$

with  $n = 0, \dots, N - 1$ . Note that the  $\hat{k}$ th shifted exponential is removed from  $\hat{y}_{ni}$ , but remains in  $\hat{y}_{nr}$ . Moreover,  $\hat{y}_{nr}$  and  $\hat{y}_{ni}$  have the  $2K - 2$  signal poles  $e^{-d_k n\Delta t \pm j2\pi(f_k - f_{\hat{k}})n\Delta t}$ ,  $k = 1, \dots, \hat{k} - 1, \hat{k} + 1, \dots, K$ , in common. The Hankel matrices  $\hat{\mathbf{H}}_r$  and  $\hat{\mathbf{H}}_i$  that are respectively constructed from  $\hat{y}_{nr}$  and  $\hat{y}_{ni}$ , have rank  $2K - 1$  and  $2K - 2$ . Moreover, the common signal poles can be removed from  $\hat{y}_{nr}$  via orthogonal projection as in HTLSPK(fd), but the SVD is used instead of QR to find the orthogonal complement  $\hat{\mathbf{U}}_{orth}$ , i.e.

$$\hat{\mathbf{H}}_i = \begin{bmatrix} \hat{\mathbf{U}}_{common} & \hat{\mathbf{U}}_{orth} \end{bmatrix} \hat{\Sigma} \hat{\mathbf{V}}^H, \quad (2.6.32)$$

where  $\hat{\mathbf{U}}_{orth}^H \hat{\mathbf{U}}_{common} = \mathbf{0}$  and  $\hat{\mathbf{U}}_{orth}^H \hat{\mathbf{H}}_i = \mathbf{0}$ . In particular, the matrix  $\tilde{\mathbf{H}}_r$ , which contains only 1 signal pole,  $e^{-d_{\hat{k}} n\Delta t}$ , can be obtained as

$$\tilde{\mathbf{H}}_r = \hat{\mathbf{U}}_{orth}^H \hat{\mathbf{H}}_r = \hat{\mathbf{U}}_{orth}^H \mathbf{S}_1 \mathbf{C}_1 \mathbf{T}_1^T, \quad (2.6.33)$$

where the subscript 1 denotes the rank of the matrix  $\tilde{\mathbf{H}}_r$ . The signal pole  $e^{-d_{\hat{k}} n\Delta t}$  can then be computed from the shift-invariance property of the row space of  $\tilde{\mathbf{H}}_r$ . In

general, if  $p$  pairs  $(f_k, \phi_k)$  are known,  $k = 1, \dots, p$ , the above procedure is repeated to estimate the damping factor  $d_k$  corresponding to each of these pairs. Since  $p$  signal poles are known, the remaining  $K - p$  poles can be estimated by applying the signal pole estimation part of HTLSPK(fd). Concerning the estimation of the amplitudes and unknown phases, HTLSPK(fp) differs from HTLS and HTLSPK(fd) since the number of the real unknowns,  $a_k$  and  $\phi_k$ , is reduced from  $2K$  to  $2K - p$ , when  $\phi_k$ ,  $k = 1, \dots, p$ , are known. More precisely, in HTLS and HTLSPK(fd), the amplitude and phase estimates are obtained by solving in the LS sense the following system of  $N$  equations

$$\begin{bmatrix} 1 & 1 & \cdots & 1 \\ z_1 & z_2 & \cdots & z_K \\ \vdots & \vdots & \ddots & \vdots \\ z_1^{N-1} & z_2^{N-1} & \cdots & z_K^{N-1} \end{bmatrix} \begin{bmatrix} c_1 \\ c_2 \\ \vdots \\ c_K \end{bmatrix} \approx \begin{bmatrix} y_0 \\ y_1 \\ \vdots \\ y_{N-1} \end{bmatrix} \quad (2.6.34)$$

Instead, in HTLSPK(fp) the  $k$ th column of the left-hand side matrix of Eq.(2.6.34) is multiplied by  $e^{j\phi_k}$  and the  $k$ th element  $c_k$  is multiplied by  $e^{-j\phi_k}$ , where  $k = 1, \dots, p$ . Therefore, Eq.(2.6.34) is replaced by

$$\mathbf{A}\mathbf{c} \approx \mathbf{y}, \quad (2.6.35)$$

where  $\mathbf{c} = [a_1, \dots, a_p, c_{p+1}, \dots, c_K]^T$ . If each element of the system is separated into real and imaginary parts, i.e.,  $\mathbf{c} = \mathbf{c}_r + j\mathbf{c}_i$ ,  $\mathbf{A} = \mathbf{A}_r + j\mathbf{A}_i$  and  $\mathbf{y} = \mathbf{y}_r + j\mathbf{y}_i$ , then Eq.(2.6.35) consists of a system with  $2N$  real-valued equations, namely

$$\begin{bmatrix} \mathbf{A}_r & -\mathbf{A}_i \\ \mathbf{A}_i & \mathbf{A}_r \end{bmatrix} \begin{bmatrix} \mathbf{c}_r \\ \mathbf{c}_i \end{bmatrix} \approx \begin{bmatrix} \mathbf{y}_r \\ \mathbf{y}_i \end{bmatrix}, \quad (2.6.36)$$

where  $\mathbf{c}_r = [a_1, \dots, a_p, c_{(p+1)r}, \dots, c_{Kr}]^T$ ,  $\mathbf{c}_i = [0, \dots, 0, c_{(p+1)i}, \dots, c_{Ki}]^T$ . Since the first  $p$  elements of  $\mathbf{c}_i$  are equal to zero, the corresponding columns in the left-hand side matrix can be dropped.

As a result, the system in Eq.(2.6.36) contains a reduced number of real-valued unknowns, i.e.  $2K - p$ , which will further improve the accuracy of the estimation. In particular, the final estimates are obtained as  $a_k = \|c_{kr} + jc_{ki}\|$  and  $\phi_k = \tan^{-1}(c_{kr}/c_{ki})$ ,  $k = p + 1, \dots, K$ .

### 2.6.3 HTLSPK(fdp)

If  $f_k$ ,  $d_k$  and  $\phi_k$ , with  $k = 1, \dots, p$ , are all known, the so-called HTLSPK(fdp) algorithm can be applied. Practically, it is equal to the HTLSPK(fp) method without the part in which the damping factor corresponding to each pair of known frequency and phase is estimated.

### 2.6.4 HTLSPK(p)

If only  $\phi_k$ , with  $k = 1, \dots, p$ , are known, the pole estimation part of HTLS can be applied, followed by the amplitude and phase estimation part of HTLSPK(fp). This algorithm is called HTLSPK(p), whose results are suboptimal with respect to the previous ones since the prior knowledge of the phases is not used in the pole estimation part.

### 2.6.5 HTLSPK( $\Delta f d_{eq}$ )

Assume that the signal  $y_n$ ,  $n = 0, \dots, N-1$ , is described by Eq.(2.2.1) and that we have as prior knowledge

$$d_1 = d_2 = d \text{ and } f_2 = f_1 + \Delta f, \quad (2.6.37)$$

with  $d$  and  $f_1$  unknown and  $\Delta f$  known. We shift the data in frequency

$$\tilde{y}_n = y_n e^{-j2\pi\Delta f n \Delta t}, \quad (2.6.38)$$

which can be written in the following form

$$\tilde{y}_n = c_2 e^{(-d_1 + j2\pi f_1)n \Delta t} + \sum_{k=1, k \neq 2}^K c_1 e^{(-d_k + j2\pi(f_k - \Delta f))n \Delta t}. \quad (2.6.39)$$

This means that  $y_n$  and  $\tilde{y}_n$  have one signal pole in common from which the pair  $(f_1, d_1)$  can be estimated. This signal pole is computed via the intersection of the column subspaces [25] of the Hankel matrices  $\mathbf{H}$  and  $\tilde{\mathbf{H}}$  obtained from the elements  $y_n$  and  $\tilde{y}_n$  as done in Eq.(4.1.6). More precisely, we compute the rank  $K$  truncated SVD of the two matrices  $\mathbf{H}$  and  $\tilde{\mathbf{H}}$

$$\mathbf{H}_K = \mathbf{U}_K \mathbf{\Sigma}_K \mathbf{V}_K^H \quad (2.6.40)$$

$$\tilde{\mathbf{H}}_K = \tilde{\mathbf{U}}_K \tilde{\mathbf{\Sigma}}_K \tilde{\mathbf{V}}_K^H, \quad (2.6.41)$$

and the SVD of the matrix  $\mathbf{U}_K^H \tilde{\mathbf{U}}_K$

$$\mathbf{U}_K^H \tilde{\mathbf{U}}_K = \dot{\mathbf{U}} \dot{\mathbf{\Sigma}} \dot{\mathbf{V}}^H. \quad (2.6.42)$$

The singular values  $\dot{\sigma}_i = \cos \dot{\theta}_i$  of  $\mathbf{U}_K^H \tilde{\mathbf{U}}_K$  yield the canonical angles  $\dot{\theta}_i$  and point out the correlation between both subspaces. Then, a basis for the intersection of  $\mathbf{U}_K$  and  $\tilde{\mathbf{U}}_K$  is

$$\ddot{\mathbf{U}} = \mathbf{U}_K [\dot{\mathbf{u}}_1, \dots, \dot{\mathbf{u}}_s], \quad (2.6.43)$$

where  $s$  is the number of common poles for  $\mathbf{H}_K$  and  $\tilde{\mathbf{H}}_K$  and  $[\dot{\mathbf{u}}_1, \dots, \dot{\mathbf{u}}_s]$  denotes the first  $s$  columns of  $\dot{\mathbf{U}}$ . Note that  $\dot{\sigma}_i = 1$  in the noiseless case, while  $\dot{\sigma}_i \geq 1 - \epsilon$

in the noisy case with  $\epsilon$  a user-defined tolerance. If  $y_n$  has only one pair of poles  $(z_1, z_2)$  with frequency difference  $\Delta f$  and equal damping, then  $s = 1$  and  $z_1$  is computed using the shift-invariance property in the column space

$$\ddot{\mathbf{U}}_{\downarrow} z_1 = \ddot{\mathbf{U}}^{\uparrow}, \quad (2.6.44)$$

where  $\ddot{\mathbf{U}}_{\downarrow}$  and  $\ddot{\mathbf{U}}^{\uparrow}$  are derived from  $\ddot{\mathbf{U}}$  by deleting its last and first row respectively. In the presence of noise, Eq.(2.6.44) is solved with TLS yielding an estimate for  $z_1 = e^{(-d_1 + j2\pi f_1)\Delta t}$  and hence also for  $z_2 = e^{(-d_2 + j2\pi f_2)\Delta t}$  since  $f_2 = f_1 + \Delta f$  and  $d_1 = d_2$ . If, more generally,  $y_n$  has  $s + 1$  poles  $(z_1, z_2, \dots, z_{s+1})$  with the same frequency difference  $\Delta f = \Delta f_1 = \dots = \Delta f_s$  and equal dampings  $d_1 = \dots = d_s$ , then the intersection of  $\mathbf{U}_K$  and  $\tilde{\mathbf{U}}_K$  has dimension  $s$  and a basis is computed by exploiting Eq.(2.6.43). Solving

$$\ddot{\mathbf{U}}_{\downarrow} \ddot{\mathbf{Z}} = \ddot{\mathbf{U}}^{\uparrow}, \quad (2.6.45)$$

the computation of the eigenvalues of  $\ddot{\mathbf{Z}}$  yields the desired signal poles  $z_i$ ,  $i = 1, \dots, s$ .

In the presence of noise, Eq.(2.6.45) is solved by using TLS and the computed pairs  $(f_i, d_i)$  only approximately satisfy the imposed constraints. Therefore, the following correction is applied: compute by averaging

$$\bar{f} = \frac{1}{s} \left( \sum_{i=1}^s f_i - (i-1)\Delta f \right) \quad \text{and} \quad \bar{d} = \frac{1}{s} \sum_{i=1}^s d_i \quad (2.6.46)$$

and, then, set  $f_i = \bar{f} + (i-1)\Delta f$  and  $d_i = \bar{d}$  for  $i = 1, \dots, s + 1$ .

### 2.6.6 HTLSPKfast( $\Delta f d_{eq}$ )

A more efficient version of HTLSPK( $\Delta f d_{eq}$ ) can be obtained by observing that

$$\tilde{\mathbf{H}} = \mathbf{D}_L \mathbf{H} \mathbf{D}_{N-L+1}^T, \quad (2.6.47)$$

where  $\mathbf{D}_k$  is unitary (with  $k = L$  or  $N - L + 1$ ) and defined as

$$\mathbf{D}_k = \text{diag}(1, e^{-j2\pi\Delta f\Delta t}, \dots, e^{-(k-1)j2\pi\Delta f\Delta t}). \quad (2.6.48)$$

This implies that  $\tilde{\mathbf{U}}_K = \mathbf{D}_L \mathbf{U}_K$ . Hence,  $\tilde{\mathbf{U}}_K$  can be computed directly from the SVD of the matrix  $\mathbf{H}$  (i.e., the SVD of  $\tilde{\mathbf{H}}$  can be avoided) thereby improving the computational efficiency of HTLSPK( $\Delta f d_{eq}$ ).

Here, an outline of the algorithm is provided since it will be applied in Chapter 4.

#### Outline of the HTLSPKfast( $\Delta f d_{eq}$ ) algorithm

- **Step 1 :**

Arrange the  $N$  data points  $y_n$ ,  $n = 0, \dots, N - 1$ , in a Hankel matrix  $\mathbf{H}$  of dimensions  $L \times M$ , with  $N = L + M - 1$

$$\mathbf{H} = \begin{bmatrix} y_0 & y_1 & \cdots & y_{M-1} \\ y_1 & y_2 & \cdots & y_M \\ \vdots & \vdots & \vdots & \vdots \\ y_{L-1} & y_L & \cdots & y_{N-1} \end{bmatrix}$$

- **Step 2 :**

Compute the truncated SVD of the Hankel matrix  $\mathbf{H}$

$$\mathbf{H}_K = \mathbf{U}_K \mathbf{\Sigma}_K \mathbf{V}_K^H$$

where  $\mathbf{U}_K$  and  $\mathbf{V}_K$  are the first  $K$  columns of the left and right singular vector matrices  $\mathbf{U}$  and  $\mathbf{V}$ , respectively,  $\mathbf{\Sigma}_K$  is the  $K \times K$  upper-left sub-matrix of the singular value matrix  $\mathbf{\Sigma}$ .

- **Step 3 :**

Construct the matrix

$$\mathbf{D}_L = \text{diag}(1, e^{-j2\pi\Delta f\Delta t}, \dots, e^{-(L-1)j2\pi\Delta f\Delta t})$$

and compute the matrix

$$\tilde{\mathbf{U}}_K = \mathbf{D}_L \mathbf{U}_K.$$

- **Step 4 :**

Compute the SVD of the matrix  $\mathbf{U}_K^H \tilde{\mathbf{U}}_K$ , i.e.

$$\mathbf{U}_K^H \tilde{\mathbf{U}}_K = \dot{\mathbf{U}} \dot{\mathbf{\Sigma}} \dot{\mathbf{V}}^T.$$

- **Step 5 :**

Form the basis for the intersection of  $\mathbf{U}_K$  and  $\tilde{\mathbf{U}}_K$

$$\ddot{\mathbf{U}} = \mathbf{U}_K [\dot{\mathbf{u}}_1, \dots, \dot{\mathbf{u}}_s],$$

where  $s$  is the number of common poles for  $\mathbf{H}_K$  and  $\tilde{\mathbf{H}}_K$  and  $[\dot{\mathbf{u}}_1, \dots, \dot{\mathbf{u}}_s]$  denotes the first  $s$  columns of  $\dot{\mathbf{U}}$ .

- **Step 6 :**

Compute the TLS solution of the system obtained from the shift-invariance property in the column space

$$\ddot{\mathbf{U}}_{\downarrow} \ddot{\mathbf{Z}} = \ddot{\mathbf{U}}^{\uparrow},$$

where  $\ddot{\mathbf{U}}_{\downarrow}$  and  $\ddot{\mathbf{U}}^{\uparrow}$  are obtained from  $\ddot{\mathbf{U}}$  deleting its last and first row respectively. The computation of the eigenvalues of  $\ddot{\mathbf{Z}}$  yields the desired signal poles  $z_i = e^{(-d_i + j2\pi f_i)\Delta t}$ ,  $i = 1, \dots, s$ .

- **Step 7 :**

Apply the following correction: compute by averaging

$$\bar{f} = \frac{1}{s} \left( \sum_{i=1}^s f_i - (i-1)\Delta f \right) \quad \text{and} \quad \bar{d} = \frac{1}{s} \sum_{i=1}^s d_i$$

and, then, set  $f_i = \bar{f} + (i-1)\Delta f$  and  $d_i = \bar{d}$  for  $i = 1, \dots, s+1$ .

- **Step 8 :**

Compute the remaining signal poles  $z_i$ ,  $i = s+1, \dots, K$ , by applying the signal pole estimation part of the HTLSPK(fd) algorithm. More precisely, construct the known part of the Vandermonde matrix (see Eq.(2.5.14)  $\mathbf{T}_s$  by using the known signal poles.

- **Step 9 :**

Compute the QR decomposition of  $\mathbf{T}_s$

$$\mathbf{T}_s = [ \mathbf{Q}_{known} \quad \mathbf{Q}_{orth} ] [ \mathbf{R}^T \quad \mathbf{0} ]^T$$

- **Step 10 :**

Compute the projection of  $\mathbf{H}$  onto the orthogonal subspace

$$\tilde{\mathbf{H}} = \mathbf{H} \mathbf{Q}_{orth}^H$$

- **Step 11 :**

The unknown signal poles are obtained by computing the SVD of the matrix  $\tilde{\mathbf{H}}$ , i.e.

$$\tilde{\mathbf{H}} = \tilde{\mathbf{U}}_{K-s} \tilde{\mathbf{\Sigma}}_{K-s} \tilde{\mathbf{V}}_{K-s}^H,$$

where  $\tilde{\mathbf{U}}_{K-s}$ ,  $\tilde{\mathbf{\Sigma}}_{K-s}$ ,  $\tilde{\mathbf{V}}_{K-s}$  respectively contain the first  $K - s$  left singular vectors, singular values and right singular vectors, and by solving the following set of equations, derived from the shift-invariance property, i.e.

$$\tilde{\mathbf{U}}_{K-s\downarrow} \mathbf{Z}_{K-s}^{(\tilde{U})} = \tilde{\mathbf{U}}_{K-s}^{\uparrow},$$

The eigenvalues of  $\mathbf{Z}_{K-s}^{(\tilde{U})}$  yield the unknown signal poles  $\hat{z}_i$ ,  $i = s + 1, \dots, K$ .

• **Step 12 :**

Filling in the estimated signal poles  $\hat{z}_i$  into the model equation (2.5.13), yields the set of equations in the complex amplitudes  $c_k$

$$y_n \approx \sum_{k=1}^K c_k \hat{z}_k^n \quad n = 0, 1, \dots, N - 1.$$

From its LS solution  $\hat{c}_k = \hat{a}_k e^{j\hat{\phi}_k}$ , we find  $\hat{a}_k$  and  $\hat{\phi}_k$ , the estimated amplitudes and phases.

## 2.7 Conclusions

In this chapter the concepts of MRS data quantification and prior knowledge were introduced. Then, some well known time-domain methods to estimate the parameters of MRS signals were outlined. Since time-domain parameter estimation methods can be divided in two classes, optimization-based methods and subspace-based methods, examples of both types were given. In particular, VARPRO and AMARES were described for the first class. These methods are flexible since they allow the choice of several theoretical model functions and the inclusion of a variety of prior knowledge. On the other hand, they require a lot of user interaction and expertise since they need good starting values in order to converge to the optimal solution. As far the class of the subspace-based methods, the popular HSVD and HTLS methods were outlined. The main advantage of these methods is that they require minimal user interaction. The main drawback inherent to this class of algorithms is that they are statistically suboptimal and allow limited inclusion of prior knowledge. Improved variants of HTLS have been developed in order to include some types of prior knowledge and a survey of such methods was provided in Section 2.6.

**IMPROVED LANCZOS  
ALGORITHMS FOR  
SUBSPACE-BASED MRS  
DATA QUANTIFICATION**

In Chapter 2 the parameter estimation method HSVD was introduced. The aim of the study presented in this chapter is to reduce the computational load required by HSVD without affecting the accuracy of the parameter estimates. Specifically, the computationally most intensive part of HSVD is the computation of the SVD of the Hankel matrix  $\mathbf{H}$ . In order to improve the efficiency, algorithms based on the Lanczos method are suitable because the main computation at each step, a matrix–vector product, can be efficiently performed by means of the Fast Fourier Transform exploiting the structure of the involved matrix. Here, we compare the performance in terms of accuracy and efficiency of HSVD when four algorithms for the computation of the SVD are used: the classical SVD algorithm based on the QR decomposition, the Lanczos algorithm with partial reorthogonalization, the implicitly restarted Lanczos algorithm and the Lanczos algorithm based on the interlacing theorem. The first algorithm and the last one are already available in the NMR literature. We propose the use of the HSVD method based on the Lanczos algorithm with partial reorthogonalization and the implicitly restarted Lanczos algorithm. Extensive simulation studies show that the latter two methods perform best.

The chapter is organized as follows: in Section 3.1 the classical SVD algorithm, which makes use of the QR decomposition, is introduced. Section 3.2 describes the Lanczos bidiagonalization procedure as well as the properties which make it significantly more efficient with respect to the classical SVD algorithm. Unfortunately, when the Lanczos bidiagonalization is carried out in finite precision arithmetic, multiple copies of the same singular values and other drawbacks arise, and HSVD fails in computing the parameter estimates. Sections 3.3, 3.4 and 3.5 describe three variants of the Lanczos bidiagonalization procedure that address such problems. More precisely, Section 3.3 is devoted to the Lanczos algorithm with partial reorthogonalization, Section 3.4 describes the implicitly restarted Lanczos algorithm and in Section 3.5 the Lanczos-based algorithm called HLSVD, which makes use of some eigenvalues’ properties, is explained. In Section 3.6 four HSVD–based methods are considered, which are based on the algorithms introduced in Sections 3.1, 3.3, 3.4 and 3.5, and a numerical comparison is carried out in terms of efficiency and accuracy. Finally, Section 3.7 summarizes the main conclusions.

### 3.1 Computing the truncated SVD

Various algorithms are available for computing the SVD of a matrix. The most reliable algorithm for dense matrices is due to Golub and Reinsch [27] and it is available in LAPACK [1].

In the Golub–Reinsch algorithm the matrix  $\mathbf{H}$  is first transformed by Householder matrices into a bidiagonal matrix  $\mathbf{B}$

$$\mathbf{Q}^H \mathbf{H} \mathbf{P} = \mathbf{B}. \quad (3.1.1)$$

Since the matrices  $\mathbf{Q}$  and  $\mathbf{P}$  are unitary, the bidiagonal matrix  $\mathbf{B}$  has the same singular values as  $\mathbf{H}$ . The SVD of  $\mathbf{B}$  is computed by using the QR algorithm

$$\mathbf{B} = \mathbf{Q}_B \Sigma \mathbf{P}_B^H \quad (3.1.2)$$

and the final SVD then becomes

$$\mathbf{H} = \mathbf{Q} \mathbf{Q}_B \Sigma (\mathbf{P} \mathbf{P}_B)^H = \mathbf{U} \Sigma \mathbf{V}^H. \quad (3.1.3)$$

A description of the QR algorithm for computing the SVD of a bidiagonal matrix can be found in [25].

The Golub–Reinsch method computes the full SVD in a reliable way and takes approximately  $2LM^2 + 4M^3$  complex multiplications for an  $L \times M$  matrix. However, when only the computation of a few largest singular values and corresponding singular vectors is needed, as in our case, the method is computationally too expensive. Moreover, it does not exploit the particular structure of the Hankel matrix  $\mathbf{H}$ . For this type of matrices, the matrix–vector product can be computed efficiently by using the Fast Fourier Transform (FFT) matrix. Moreover, Hankel matrices can be stored in  $L + M - 1$  memory locations rather than in  $LM$  and this property is crucial when dealing with large matrices.

### 3.2 The Lanczos bidiagonalization algorithm

An efficient tool for computing the SVD of large and structured or sparse matrices is the Lanczos bidiagonalization [25]. Given the rectangular  $L \times M$  matrix  $\mathbf{H}$ , the algorithm computes a sequence of vectors (Lanczos vectors)  $\mathbf{u}_j \in \mathbb{C}^L$  and  $\mathbf{v}_j \in \mathbb{C}^M$ , where  $\mathbb{C}$  is the set of complex numbers, and scalars  $\alpha_j$  and  $\beta_j$  for  $j = 1, 2, \dots$  as follows

Choose a starting vector  $\mathbf{p}_0 \in \mathbb{C}^L$ ,  $\mathbf{p}_0 \neq \mathbf{0}$  and let  $\beta_1 = \|\mathbf{p}_0\|_2$ ,  $\mathbf{u}_1 = \mathbf{p}_0/\beta_1$  and  $\mathbf{v}_0 \equiv \mathbf{0}$

```

for  $j = 1, 2, \dots$ 
   $\mathbf{r}_j = \mathbf{H}^H \mathbf{u}_j - \beta_j \mathbf{v}_{j-1}$ 
   $\alpha_j = \|\mathbf{r}_j\|_2$ 
   $\mathbf{v}_j = \mathbf{r}_j / \alpha_j$ 
   $\mathbf{p}_j = \mathbf{H} \mathbf{v}_j - \alpha_j \mathbf{u}_j$ 
   $\beta_{j+1} = \|\mathbf{p}_j\|_2$ 
   $\mathbf{u}_{j+1} = \mathbf{p}_j / \beta_{j+1}$ 
end

```

After  $k$  steps, the lower bidiagonal matrix  $\mathbf{B}_k$  is generated

$$\mathbf{B}_k = \begin{bmatrix} \alpha_1 & & & & \\ \beta_2 & \alpha_2 & & & \\ & \beta_3 & \ddots & & \\ & & \ddots & \alpha_k & \\ & & & \beta_{k+1} & \end{bmatrix}. \quad (3.2.4)$$

In exact arithmetic the Lanczos vectors are orthonormal such that

$$\mathbf{U}_{k+1} = [\mathbf{u}_1, \mathbf{u}_2, \dots, \mathbf{u}_{k+1}] \in \mathbb{C}^{L \times (k+1)}, \quad (3.2.5)$$

$$\mathbf{V}_k = [\mathbf{v}_1, \mathbf{v}_2, \dots, \mathbf{v}_k] \in \mathbb{C}^{M \times k}, \quad (3.2.6)$$

with  $\mathbf{U}_{k+1}^H \mathbf{U}_{k+1} = \mathbf{I}_{k+1}$  and  $\mathbf{V}_k^H \mathbf{V}_k = \mathbf{I}_k$ , where  $\mathbf{I}_l$  is the  $l \times l$  identity matrix. By construction, the columns of  $\mathbf{U}_{k+1}$  and  $\mathbf{V}_k$  satisfy the recurrences

$$\begin{aligned} \alpha_j \mathbf{v}_j &= \mathbf{H}^H \mathbf{u}_j - \beta_j \mathbf{v}_{j-1}, \\ \beta_{j+1} \mathbf{u}_{j+1} &= \mathbf{H} \mathbf{v}_j - \alpha_j \mathbf{u}_j. \end{aligned} \quad (3.2.7)$$

We will refer to the columns of  $\mathbf{U}_{k+1}$  as left Lanczos vectors and the columns of  $\mathbf{V}_k$  as right Lanczos vectors. The singular values of  $\mathbf{B}_k$  converge monotonically to those of  $\mathbf{H}$ . Moreover, the extremal ones converge first [16].

The Lanczos procedure is an iterative method and the needed number of iterations depends on the distribution of the singular values and on the choice of the initial vector  $p_0$ . The latter is of crucial importance. In fact, let us assume that  $K$  eigenpairs need to be computed. A well known theorem states that if the vector  $p_0$  is equal to the linear combination of  $K$  eigenvectors, then the Lanczos recursion ends after  $K$  steps. Therefore, a good starting vector should be chosen as closely as possible to such a linear combination.

At each step of the Lanczos algorithm, two matrix–vector products,  $\mathbf{H}^H \mathbf{u}_j$  and  $\mathbf{H} \mathbf{v}_j$ , are performed. Taking into account the Hankel structure of the involved matrix  $\mathbf{H}$ , this can be done with  $O((L+M) \times \log_2(L+M))$  complexity by means of the FFT, rather than  $O(LM)$  complexity. The idea of using the FFT for computing a Hankel matrix–vector product was first used by Bluestein in 1968, in a discrete Fourier transform algorithm [63]. A later reference is the work by O’Leary and Simmons which was published in 1981 [43].

The FFT cannot be used directly to evaluate the Hankel matrix–vector product. Instead, the Hankel matrix is first embedded in a circulant matrix for which the FFT may be used to evaluate the circulant matrix–vector product.

### 3.2.1 Circulant matrices

An  $n \times n$  matrix is called circulant if it has the following form

$$\mathbf{C} = \begin{bmatrix} c_0 & c_{n-1} & c_{n-2} & \cdots & c_1 \\ c_1 & c_0 & c_{n-1} & \cdots & c_2 \\ c_2 & c_1 & c_0 & \cdots & c_3 \\ \vdots & \vdots & \cdots & \vdots & \vdots \\ c_{n-1} & c_{n-2} & c_{n-3} & \cdots & c_0 \end{bmatrix}. \quad (3.2.8)$$

$\mathbf{C}$  is a special kind of Toeplitz matrix where each row is obtained by doing a wrap-around downshift of the previous column. This means that  $\mathbf{C}$  is completely specified by its first column and can be written as

$$\mathbf{C} = [ \mathbf{c} \quad \mathbf{R}\mathbf{c} \quad \mathbf{R}^2\mathbf{c} \quad \cdots \quad \mathbf{R}^{n-1}\mathbf{c} ], \quad (3.2.9)$$

where

$$\mathbf{c} = [ c_0 \quad c_1 \quad c_2 \quad \cdots \quad c_{n-1} ]^T, \quad (3.2.10)$$

$$\mathbf{R} = [ \mathbf{e}_2 \quad \mathbf{e}_3 \quad \cdots \quad \mathbf{e}_n \quad \mathbf{e}_1 ], \quad (3.2.11)$$

with  $\mathbf{e}_k$  the the  $k$ th column of the identity matrix.

A circulant matrix satisfies several properties and, in particular, it can be diagonalized by the FFT matrix, i.e.

$$\mathbf{C} = \mathbf{F}^H \mathbf{\Delta} \mathbf{F} \quad (3.2.12)$$

with  $\mathbf{\Delta} = \text{diag}(\mathbf{F}\mathbf{c})$  is a diagonal matrix and

$$\mathbf{F} = \frac{1}{\sqrt{n}} \begin{bmatrix} 1 & 1 & 1 & \cdots & 1 \\ 1 & \omega^1 & \omega^2 & \cdots & \omega^{n-1} \\ 1 & \omega^2 & \omega^4 & \cdots & \omega^{2(n-1)} \\ \vdots & \vdots & \cdots & \vdots & \vdots \\ 1 & \omega^{n-1} & \omega^{2(n-1)} & \cdots & \omega^{(n-1)(n-1)} \end{bmatrix}, \quad (3.2.13)$$

which is unitary and where  $\omega = e^{-j2\pi/n}$ .

The factorization of Eq.(3.2.12) can be used for performing the matrix–vector multiplication. It follows that:

$$\mathbf{y} = \mathbf{C}\mathbf{x} = \mathbf{F}^H \text{diag}(\mathbf{F}\mathbf{c})\mathbf{F}\mathbf{x} = \mathbf{F}^H((\mathbf{F}\mathbf{c}) .* (\mathbf{F}\mathbf{x})), \quad (3.2.14)$$

where “.\*” is elementwise multiplication. Thus, to perform the matrix–vector multiplication,  $\mathbf{F}\mathbf{c}$  and  $\mathbf{F}\mathbf{x}$  are first computed and, then, the inverse transform of their pointwise product is calculated. The gain in using the FFT is most significant if the dimension of the vector is a power of two and, in this case, the matrix–vector product only requires  $O(n \log_2 n)$  complex multiplications.

### 3.2.2 Embedding a Toeplitz matrix in a circulant matrix

Given an arbitrary Toeplitz matrix  $\mathbf{T}$

$$\mathbf{T} = \begin{bmatrix} x_m & x_{m+1} & \cdots & \cdots & x_{m+n-1} \\ x_{m-1} & x_m & x_{m+1} & \cdots & \vdots \\ \vdots & x_{m-1} & x_m & \ddots & \vdots \\ \vdots & & x_{m-1} & \ddots & x_{m+1} \\ \vdots & & & \ddots & x_m \\ \vdots & & & & x_{m-1} \\ \vdots & & & & \vdots \\ x_1 & & & & x_n \end{bmatrix}, \quad (3.2.15)$$

it is completely specified by the following vectors

$$\mathbf{t}_{row} = [x_{m+n-1} \ x_{m+n-2} \ \cdots \ x_{m+1}]^T, \quad (3.2.16)$$

$$\mathbf{t}_{col} = [x_m \ x_{m-1} \ \cdots \ x_1]^T. \quad (3.2.17)$$

These two vectors can be used to form the first column of a circulant matrix and, thus, to embed the matrix  $\mathbf{T}$  in a circulant matrix  $\mathbf{C}$

$$\mathbf{c} = \begin{bmatrix} \mathbf{t}_{col} \\ \mathbf{0} \\ \mathbf{t}_{row} \end{bmatrix}, \quad (3.2.18)$$

$$(3.2.19)$$

where the extra zeros are used to make the dimension of  $\mathbf{c}$  a power of two, in order to obtain good performance of the FFT. The vector  $\mathbf{c}$  is used to construct the circulant matrix  $\mathbf{C}$ , whose top corner  $\mathbf{C}(1:m, 1:n)$  equals  $\mathbf{T}$ , i.e.

$$\mathbf{C} = \begin{bmatrix} \mathbf{T} & * \\ * & * \end{bmatrix}. \quad (3.2.20)$$

### 3.2.3 Toeplitz matrix-vector multiplication

To evaluate the Toeplitz matrix-vector product  $\mathbf{y} = \mathbf{T}\mathbf{x}$ , two new vectors  $\tilde{\mathbf{x}}$  and  $\tilde{\mathbf{y}}$  are formed of the same dimension as  $\mathbf{c}$

$$\tilde{\mathbf{x}} = [\mathbf{x} \ \mathbf{0}]^T, \quad (3.2.21)$$

$$\tilde{\mathbf{y}} = [\mathbf{y} \ *]^T. \quad (3.2.22)$$

$$(3.2.23)$$

The result  $\mathbf{y}$  is obtained as the  $m$  top elements in the result of  $\tilde{\mathbf{y}} = \mathbf{C}\tilde{\mathbf{x}}$ .

### 3.2.4 Hankel matrix-vector multiplication

It is well known that a Hankel matrix  $\mathbf{H}$  is easily obtained from a Toeplitz matrix  $\mathbf{T}$  by simply multiplying the latter by a permutation matrix  $\mathbf{P}$ , i.e.

$$\mathbf{H} = \mathbf{P}\mathbf{T}, \quad (3.2.24)$$

where  $\mathbf{P}$  is the anti-identity matrix. Therefore, the Hankel matrix-vector multiplication  $\mathbf{y} = \mathbf{H}\mathbf{x}$  can be computed in an efficient way by applying (3.2.14) and by reversing the order of the entries in the resulting vector  $\mathbf{y}$ .

## 3.3 The Lanczos algorithm with partial reorthogonalization

When the Lanczos bidiagonalization is carried out in finite precision arithmetic, error vectors accounting for the rounding errors at the  $j$ th step occur in the recurrence relations described in (3.2.7), and the orthogonality among the left and right Lanczos vectors is gradually lost. Moreover, multiple copies of the same singular values can arise.

There exist several ways for obtaining a robust Lanczos method in finite precision arithmetic. One of them is to enforce orthogonality among the Lanczos vectors by applying some reorthogonalization schemes. The simplest is the so-called full reorthogonalization procedure: each new Lanczos vector  $\mathbf{u}_{j+1}$  is orthogonalized against all previous  $\mathbf{u}_i$ ,  $i = 1, \dots, j$ , using, e.g., the Modified Gram-Schmidt algorithm. A similar procedure can be applied for the right Lanczos vectors  $\mathbf{v}_j$ . However, this algorithm is considered too expensive for large problems. In fact, the additional  $O(4(L+M)k^2)$  operations required by the orthogonalization quickly dominate the execution time, unless the necessary number of iterations  $k$  is very small compared to the dimensions of the problem. The storage requirements may also be a limiting factor since all the generated Lanczos vectors need to be saved. More efficient algorithms exist and are mainly based on work by Paige [45], who carried out a thorough error analysis of the Lanczos algorithm and managed to find out when and where the loss of orthogonality takes place.

Among these algorithms there is the Lanczos algorithm with partial reorthogonalization (PRO). Its central idea is that the level of orthogonality among the Lanczos vectors satisfies a recurrence relation which can be derived from the recurrence relations used to generate the vectors themselves. These recurrences can be used as a practical tool for computing estimates of the level of orthogonality in an efficient way, and this information can be used to decide when to reorthogonalize and which Lanczos vectors need to be included in the reorthogonalization [55]. A reliable implementation of this method is available in PROPACK [34].

## 3.4 The implicitly restarted Lanczos algorithm

When using Lanczos with full reorthogonalization, all Lanczos vectors need to be stored. Moreover, there is no way to know in advance how many steps will be

needed to provide the singular values of interest within a specified accuracy. The number of steps is determined by the distribution of the singular values and the choice of the starting vector  $\mathbf{p}_0$ . In many cases, e.g. as in the case where there is no significant gap between the wanted and unwanted singular values, convergence will not occur until  $k$  gets very large and the method suffers from large storage requirements and from numerical difficulties caused by loss of orthogonality of the generated basis vectors. These problems can be overcome by limiting the size of the basis set and by using restarting schemes, i.e. restarting the iterations after a number of steps by replacing the starting vector with an “improved” starting vector. Reorthogonalization is also performed when needed. This procedure keeps the storage requirement fixed and the computation load moderate. Several variants of explicitly restarted Lanczos methods have been developed and some references can be found in [57]. Calvetti, Reichel and Sorensen have proposed an implicitly restarted Lanczos algorithm (IRL) [5], which is an adaptation of the Implicitly Restarted Arnoldi method [57] to the case when a matrix is Hermitian. This method forces the initial vector into an invariant subspace of the matrix, by repeatedly filtering the initial vector through a polynomial filter and restarting the iterations implicitly. It can be considered as a technique which combines the implicitly shifted QR scheme [25] with a  $k$ -step Lanczos factorization, obtaining a truncated form of the implicitly shifted QR iteration. The numerical difficulties and storage problems normally associated with the Lanczos process are avoided. In fact, the method is able to compute a few ( $K$ ) singular values with user-specified features, such as the algebraically largest or smallest singular values, using storage for only a moderate multiple of  $K$  vectors. The computed singular vectors form a basis for the desired  $K$ -dimensional eigenspace and are numerically orthogonal to working precision. A reliable implementation of this method is included in ARPACK [38].

### 3.5 HLSVD

The popular method called HLSVD, which is very frequently used in NMR spectroscopy for solvent suppression, is a Lanczos-based HSVD algorithm. In fact, the computation of the truncated SVD of the matrix  $\mathbf{H}$ , which occurs in the HSVD method, is based on the Lanczos algorithm, but without using any reorthogonalization scheme. In this method, the extra copies of converged singular values are eliminated by using the so-called van Kats – van der Vorst procedure, which is based on the following property of the eigenvalues [16]

**The interlacing theorem** If  $\lambda_{1,j} \geq \lambda_{2,j} \geq \dots \geq \lambda_{j,j}$  denote the eigenvalues of  $\mathbf{B}_j$ , then

$$\lambda_{1,j} \geq \lambda_{1,j-1} \geq \lambda_{2,j} \geq \lambda_{2,j-1} \geq \dots \geq \lambda_{j-1,j} \geq \lambda_{j-1,j-1} \geq \lambda_{j,j}. \quad (3.5.25)$$

Because of the finite precision, the interlacing property will sooner or later be violated and at a certain stage the inequality  $\lambda_{k,j} \leq \lambda_{k,j-1}$  occurs. Because of the finite

precision in which the computer is working, it is impossible to distinguish between the eigenvalue  $\lambda_{k,j-1}$  of  $\mathbf{B}_{j-1}$  and  $\lambda_{k,j}$  of  $\mathbf{B}_j$ . Consequently, an eigenvalue of  $\mathbf{H}$  has been found. For further details, the method is described in [46] and implemented in the freely available software package MRUI:  
<http://www.mrui.uab.es/mrui/mruiHomePage.html>.

### 3.6 Lanczos-based HSVD methods: a numerical comparison

In the previous sections four different algorithms for computing the SVD of a Hankel matrix have been introduced: the classical SVD algorithm based on the QR decomposition, the Lanczos algorithm with partial reorthogonalization, the implicitly restarted Lanczos algorithm and the Lanczos algorithm based on the interlacing theorem. Therefore, four HSVD-based methods are obtained:

- **QR**: the classical method based on the QR decomposition;
- **PRO**: the method based on the Lanczos algorithm with partial reorthogonalization;
- **IRL**: the method based on the Implicitly Restarted Lanczos algorithm,
- **HLSVD**: the method based on the Lanczos algorithm and the interlacing theorem;

The methods QR and HLSVD are already available in the NMR literature and, as already specified above, are widely used by the NMR community. In this thesis we propose the use of the two alternative methods PRO and IRL. Here, the four HSVD-based methods are compared in terms of efficiency and accuracy. Extensive simulation studies are reported and the results show that PRO and IRL perform best.

#### 3.6.1 Comparison in computational efficiency

We consider a simulated signal derived from an *in vivo*  $^{31}\text{P}$  spectrum measured in the human brain and consisting of 256 complex data points and 11 exponentials, as defined in [67]. Figure 3.1 shows the spectrum of the simulated signal. We consider Eq.(2.2.1) with  $a_k, d_k, f_k$  and  $\phi_k$ ,  $k = 1, \dots, 11$ , known and perturb the signal by adding complex white noise with a circular Gaussian distribution with standard deviation  $\sigma$ . The SNR for each peak is measured in decibels (dB) and defined as

$$\text{SNR peak } k \equiv 20 \log\left(\frac{a_k}{\sigma}\right). \quad (3.6.26)$$

A low, intermediate and high noise level are used ( $\sigma = 5, 15, 25$  which corresponds to a SNR of 29.5, 20 and 15.6 dB for the middle peak of  $\beta - \text{ATP}$ ). Our goal is to reconstruct the parameters  $a_k, d_k, f_k$  and  $\phi_k$ ,  $k = 1, \dots, 11$ , characterizing the signal  $y_n$  and compare the execution time in seconds when computing the first

eleven singular values and vectors with the Lanczos method PRO, the complex version of the corresponding routine available in PROPACK [34], HLSVD and IRL. The computations are carried out on a PC with Intel Pentium 850 MHz in the Linux environment, in `fortran 77` with machine precision  $\omega \approx 2.22 \times 10^{-16}$ , with the exception of HLSVD, which is partly implemented in single precision. In Table 3.1 CPU times are reported for the simulated signal when considering 256 and 512 data points. We can see that PRO is clearly the fastest algorithm.

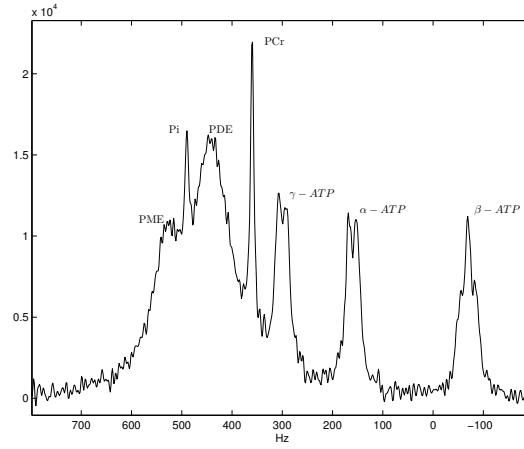


**Figure 3.1.** Real part of the spectrum of the simulated  $^{31}\text{P}$  MRS signal, obtained for  $\text{SNR}=20$ .

$\text{SNR}$	PRO	HLSVD	IRL
29.5	0.0258	0.0392	0.0389
20	0.0342	0.0560	0.0511
15.6	0.0720	0.1092	0.1085

$\text{SNR}$	PRO	HLSVD	IRL
29.5	0.0450	0.0878	0.0679
20	0.0982	0.1303	0.1473
15.6	0.3142	0.6834	0.4718

**Table 3.1.** Mean value of the computation times in seconds for 50 runs. Left:  $\text{length}(\text{signal})=256$ . Right:  $\text{length}(\text{signal})=512$ .

### 3.6.2 Statistical accuracy measure

Since HLSVD is very frequently used for water removal in the NMR spectra, in this section we apply the four HSVD-based methods QR, HLSVD, PRO and IRL to filter out the water signal in  $^1\text{H}$  spectra. We illustrate their performance in terms of statistical accuracy via computer simulation studies. More precisely, we focus on the amplitude estimates of the metabolite signals after water removal, obtained using the four methods, and compare the quality of these estimates. The quality is measured as the relative root mean squared error (RRMSE) in percent

$$\text{RRMSE peak } k \equiv 100 \sqrt{\frac{1}{L} \sum_{l=1}^L \frac{(a_k - \tilde{a}_k^l)^2}{a_k^2}}, \quad (3.6.27)$$

where  $L$  is the number of simulation runs and  $\tilde{a}_k^l$  denotes the estimate of  $a_k$  obtained in simulation run  $l$ . The RRMSE is compared with the relative Cramer-Rao lower bound (CRB). The CRB indicates the best possible accuracy of an estimate among all unbiased estimators.

### 3.6.3 HSVD for solvent suppression

The  $^1\text{H}$  spectrum contains the signal contribution of the water which can have a magnitude  $10^3$  to  $10^4$  larger than the magnitude of the metabolites of interest. A preprocessing step is necessary to remove the unwanted water contribution and it is obvious that it should influence the final parameter estimates of the metabolites of interest as little as possible and have a low computational complexity. HSVD provides a mathematical fit of the data by a sum of exponentially damped complex-valued sinusoids. Hence it can be used to approximate the complicated features of the water resonance, including its large tails. The fitted water region is subsequently subtracted from the original signal. We investigate the water suppression abilities of the four HSVD-based methods in terms of accuracy.

We use the following scheme to process proton spectra:

- The user specifies the model order  $K$  and a cutoff frequency  $f_r$ , which defines a so-called water region  $[-f_r, f_r]$ .
- HSVD-based methods are used to model the original signal by a sum of  $K$  exponentially damped complex-valued sinusoids.
- The peaks with frequencies belonging to the user-defined water region are used to reconstruct the water peak, after which the reconstructed water signal is subtracted from the original signal.
- The residual signal is quantified with AMARES, which minimizes the difference between the nonlinear model function and the data.

Since experimental signals contain errors introduced by factors such as unknown lineshape, data acquisition errors and eddy currents, all inevitably present *in vivo* experiments, we use simulated signals (see Figure 3.2) to evaluate the performance of the proposed quantification scheme. The cutoff frequency is chosen equal to 35 Hz and the parameters of the seven peaks used to reconstruct the water resonance and of the five metabolite peaks can be found in [68]. This implies that the correct order of the “signal” subspace is equal to 12. The added complex noise is white and circular Gaussian distributed. The noise standard deviation  $\sigma$  is varied to simulate a number of SNRs.

In Figure 3.2 the real part of the spectrum of the simulated signal is displayed. In Figure 3.3 the RRMSE results obtained from 400 simulation runs are compared with the CRB for the amplitude estimates of peak 4 (But9) when considering the exact model order  $K = 12$ . We omit the estimation results for the other peaks because they are very similar.

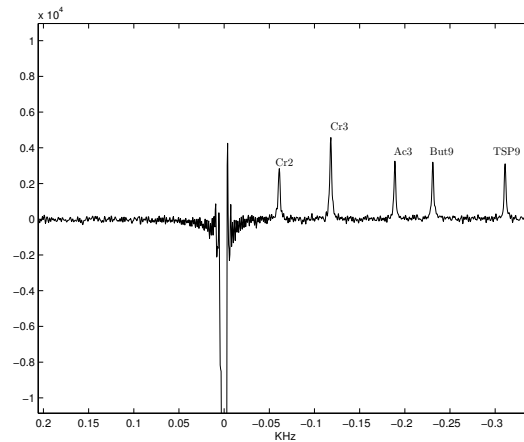


**Figure 3.2.** Real part of the spectrum of the noisy <sup>1</sup>H MRS signal containing the Water Peak obtained for SNR=15.

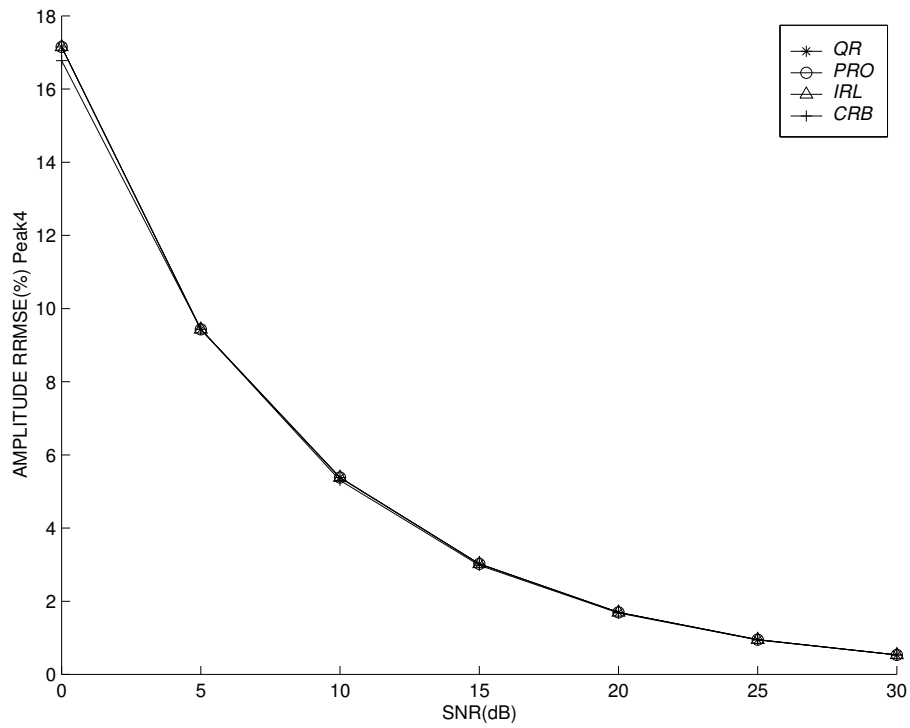


**Figure 3.3.** CRB and RRMSE of amplitude estimates as a function of the SNR for Peak4 (But9) obtained for  $K = 12$ .

First of all, QR, PRO and IRL perform in the same way and, above all, they perform in an accurate way. Moreover, we have to notice that the RRMSE results obtained by HLSVD have not been plotted. The reason for this is that when we consider SNR values greater or equal to 15, HLSVD sometimes fails in computing parameter estimates, thereby yielding too large values of the amplitude RRMSE. For SNR values lower than 15, HLSVD's behavior is comparable to the behavior of the other methods (see Table 3.2,  $K = 12$ ).

The mean value on 50 runs of the execution times in seconds are also reported (see Table 3.3) when computing the first twelve singular values with PRO and HLSVD. PRO is faster and, moreover, more accurate than HLSVD.

In Table 3.2 RRMSE results for all methods have been displayed when considering different model order values:  $K = 10$ ,  $K = 11$  and  $K = 12$ . The results clearly show that HLSVD runs into problems if the model order is exactly estimated ( $K = 12$ ); the failures rarely occur when the model order is approximately estimated ( $K = 11$ ) and disappear if it is underestimated ( $K = 10$ ). Then, we can conclude that HLSVD failure occurs when the model order is exact or overestimated. In case of underestimation, which is usually the case in practice when water removal is performed by using HLSVD, failures are unlikely to occur.

SNR	PRO ( $K = 10$ )	HLSVD ( $K = 10$ )	PRO ( $K = 11$ )	HLSVD ( $K = 11$ )	PRO ( $K = 12$ )	HLSVD ( $K = 12$ )
0	17.132	17.140	17.154	17.168	17.151	17.164
5	9.4755	9.4761	9.4634	*****	9.4329	9.4139
10	5.4277	5.4533	5.3442	5.3444	5.3819	5.4936
15	3.1248	3.1246	3.0180	3.0186	3.0188	*****
20	1.8425	1.8420	1.6958	1.6959	1.6959	*****
25	1.1475	1.1467	0.95144	0.95147	0.95123	*****
30	0.79215	0.79112	0.53493	0.60617	0.53365	*****

**Table 3.2.** RRMSE results of AMARES after preprocessing by PRO and HLSVD methods for Peak4 (But9), obtained for the model order values  $K = 10$ ,  $K = 11$  and  $K = 12$ .

### 3.6.4 HLSVD accuracy aspects

We examined several simulation runs in which HLSVD fails and noticed that the problem arises in step 3 of the HSVD method. More precisely, checking the singular values computed by the algorithm, we can observe the presence of multiple copies of the same singular value and, consequently, the same number of copies of the corresponding left singular vectors in the matrix  $\mathbf{U}_K$ . This implies that the LS solution  $\hat{\mathbf{E}}$  in step 4 has determinant equal to 0, i.e. at least one of its eigenvalues is equal to 0. In step 5 of HSVD, we extract frequency and damping factor estimates from the eigenvalues of  $\hat{\mathbf{E}}$ , the so-called signal poles. More precisely, if the  $k$ th

SNR	PRO( $K = 12$ )	HLSVD( $K = 12$ )
0	0.3622	0.6096
5	0.3884	0.6744
10	0.4050	0.7522
15	0.3582	0.7730
20	0.3246	0.8082
25	0.2624	0.7100
30	0.2284	0.5428

**Table 3.3.** Mean value of the computational times for 50 runs obtained for  $K = 12$

complex signal pole is indicated as  $z_k$ , we have:  $f_k = \text{imag}(\log(z_k))/2\pi\Delta t$  and  $d_k = -\text{real}(\log(z_k))/\Delta t$ , where the expression  $\log(z_k)$  can be evaluated only for  $z_k \neq 0$ . In order to overcome HLSVD failure, we tried to convert the code to double precision. In fact, as already specified in Section 3.6.1, the HLSVD code is partly implemented in single precision. Unfortunately, also after replacing the single precision, the code sometimes works and sometimes fails. In our investigation we noticed that the Kats – van der Vorst procedure, used to eliminate extra copies of converged singular values is not accurate enough to circumvent the numerical problems due to the loss of orthogonality among the Lanczos vectors. We can conclude that HLSVD failure is due to its inability to detect only one copy of the same singular value. As mentioned in Section 3.6.3, this problem only occurs at large SNR values when the model order is exact or overestimated, which is rarely the case in NMR practice.

### 3.7 Conclusions

In this chapter, several algorithms to compute the SVD of the Hankel matrix  $\mathbf{H}$ , occurring in the HSVD method, were introduced. The classical SVD method, based on the QR decomposition, was first described. The Lanczos bidiagonalization algorithm was then introduced in order to reduce the computation times needed by the first method. More robust variants of the Lanczos method, such as PRO, IRL and HLSVD, were then considered in order to avoid the problems occurring when working in finite precision arithmetic. The latter method, i.e. HLSVD, is very frequently used in NMR Spectroscopy for water suppression. In this chapter we proposed the use of two alternative methods, PRO and IRL, to compute the truncated SVD of a Hankel matrix, based on the Lanczos method with partial reorthogonalization or complete reorthogonalization on a small subspace. Via extensive simulation studies, we compared their performance in terms of accuracy and efficiency with the currently used HLSVD method. Our studies show that PRO and IRL outperform HLSVD in terms of computational efficiency and numerical reliability.



**SUBSPACE-BASED MRS  
DATA QUANTIFICATION OF  
MULTIPLETS USING PRIOR  
KNOWLEDGE**

As shown in Chapter 2, several subspace-based parameter estimators have been developed for quantification of MRS signals. These methods are efficient and accurate, but they suffer from a serious drawback: they allow only a limited inclusion of prior knowledge which is important for accuracy and resolution. In this chapter, the KNOB-SVD method is presented along with its improved variant KNOB-TLS. KNOB-SVD is a recently proposed method, based on the SVD, which allows the use of more prior knowledge about the signal parameters than previously published subspace-based methods. We compare its performance in terms of robustness and accuracy with the performance of three commonly used methods for signal parameter estimation that have been described in Chapter 2: HTLS, a subspace-based method which does not allow any inclusion of prior knowledge, except for the model order; HTLSPK( $\Delta fd_{eq}$ ), a subspace-based method obtained by incorporating in HTLS the prior information that the frequency differences between doublet components are known and the damping factors are equal; and AMARES, an interactive maximum likelihood method that allows the inclusion of a variety of prior knowledge. Extensive simulation and *in vivo* studies, using  $^{31}\text{P}$  as well as proton MRS signals, show that the new method outperforms HTLS and HTLSPK( $\Delta fd_{eq}$ ) in robustness and accuracy, and that it provides parameter estimates comparable to the AMARES estimates.

The chapter has the following structure: in Section 4.1 the KNOB-SVD/KNOB-TLS algorithm is described. In Section 4.2 the simulation studies are reported and the performances of KNOB-TLS, HTLS, HTLSPK( $\Delta fd_{eq}$ ) and AMARES are compared in terms of robustness and accuracy. In Section 4.3 *in vivo* studies, using  $^{31}\text{P}$  as well as  $^1\text{H}$  MRS signals, are described and the performances of KNOB-TLS, KNOB-SVD, HTLSPK( $\Delta fd_{eq}$ ), HTLS and AMARES are compared in terms of accuracy. Finally, in Section 4.4 we formulate the main conclusions.

## 4.1 KNOB-TLS algorithm for multiplet parameter estimation

In this section, we present a new subspace-based method, called *Knowledge Based Total Least Squares* (KNOB-TLS), which is an improved variant of *Knowledge Based Singular Value Decomposition* (KNOB-SVD). KNOB-SVD has recently been proposed in [58] and allows to include significantly more prior knowledge in MRS data quantification than the subspace-methods available in the MRS literature. More precisely, we assume that the function used to model the measured data points of an MRS signal is given by Eq.(2.2.1), i.e.

$$y_n = \sum_{k=1}^K a_k e^{j\phi_k} z_k^n + e_n, \quad n = 0, \dots, N-1, \quad (4.1.1)$$

where the number of components  $K$  is assumed to be known,  $z_k = e^{(-d_k + j2\pi f_k)\Delta t}$  represent the signal poles,  $(a_k, \phi_k, d_k, f_k)$  are the amplitude, phase, damping and frequency of the  $k$ th component,  $\Delta t$  is the data sampling period and  $e_n$  is the noise

term.

Our goal is to estimate the parameters  $(a_k, \phi_k, d_k, f_k)$  from  $N$  given data samples  $y_n$ ,  $n = 0, \dots, N-1$ . As prior knowledge, we assume that the amplitudes  $a_k$ , phases  $\phi_k$ , damping factors  $d_k$  and frequencies  $f_k$  of the components within multiplets satisfy the following relations

$$\begin{aligned} a_k &= c_k a \quad (a = \text{unknown}, \quad c_k = \text{known real constants}), \\ \phi_k &= \phi \quad (\phi = \text{unknown}), \\ d_k &= d \quad (d = \text{unknown}), \\ f_k &= f + (k-1)\Delta f \quad (f = \text{unknown}, \quad \Delta f = \text{known}), \end{aligned} \tag{4.1.2}$$

where  $k$  denotes the peak number in the considered multiplet components (e.g. doublet or triplet peaks) and  $\Delta f$  represents the frequency difference between the individual resonances within the considered multiplet.

In particular, the adenosine triphosphate complex, commonly called ATP, which has one triplet peak and two doublet peaks, the parameters of which are in some cases known to satisfy the above type of relations, will be considered as an example for the simulation and *in vivo* studies.

In order to explain the algorithm, we consider MRS signals characterized by one or more doublets and triplets. Without loss of generality, we focus on MRS signals with contribution from ATP, consisting of  $K$  components with  $K \geq 7$ , and containing one triplet and two doublets. The dampings and frequencies of the triplet peak satisfy the following relations:

$$\begin{aligned} d_1 &= d_2 = d_3 = d_t, \\ f_2 &= f_1 + \Delta f, \quad f_3 = f_1 + 2\Delta f; \end{aligned} \tag{4.1.3}$$

the dampings and frequencies of the doublet peaks satisfy:

$$\begin{aligned} d_4 &= d_5 = d_{d1}, \quad f_5 = f_4 + \Delta f, \\ d_6 &= d_7 = d_{d2}, \quad f_7 = f_6 + \Delta f. \end{aligned} \tag{4.1.4}$$

Finally, the amplitudes and phases of the triplet and doublet peaks satisfy:

$$\begin{aligned} 2a_1 &= a_2 = 2a_3 = a_4 = a_5 = a_6 = a_7 = a, \\ \phi_1 &= \phi_2 = \phi_3 = \phi_4 = \phi_5 = \phi_6 = \phi_7 = \phi, \end{aligned} \tag{4.1.5}$$

with  $d_t$  (damping for the triplet peak),  $d_{d1}$  (damping for the first doublet peak),  $d_{d2}$  (damping for the second doublet peak),  $a$  and  $\phi$  unknown and  $\Delta f$  known. We also assume, as prior knowledge, that the approximate frequency locations of the ATP peaks are known.

### 4.1.1 The KNOB-SVD algorithm

The algorithm KNOB-SVD has been described in [58] but is repeated here for clarity of exposition. It consists of the following steps:

- **Step 1** : Damping and frequency estimation of all peaks

Let  $\mathbf{H}$  denote the Hankel data matrix commonly used in SVD-based parameter estimation methods

$$\mathbf{H} = \begin{bmatrix} y_0 & y_1 & \cdots & y_{M-1} \\ \vdots & \vdots & \vdots & \vdots \\ y_{L-1} & y_L & \cdots & y_{N-1} \end{bmatrix}, \quad (4.1.6)$$

where  $L$  is a user parameter usually chosen less than but close to  $N/2$  in order to get the best possible parameter estimation accuracy ([11],[72],[59]). We suggest the value  $L = 2N/5$ .

For a noiseless signal, i.e.  $e_n = 0$  in Eq.(4.1.1), the matrix  $\bar{\mathbf{H}}$  can be written as

$$\bar{\mathbf{H}} = [\mathbf{a}_L(z_1) \dots \mathbf{a}_L(z_K)] \begin{bmatrix} a_1 e^{j\phi_1} & & 0 \\ & \ddots & \\ 0 & & a_K e^{j\phi_K} \end{bmatrix} \begin{bmatrix} \mathbf{a}_M^T(z_1) \\ \vdots \\ \mathbf{a}_M^T(z_K) \end{bmatrix}, \quad (4.1.7)$$

where  $M = N - L + 1$  and for  $P = L, M$  or  $N$

$$\mathbf{a}_P(z) = [1 \quad z \quad \cdots \quad z^{P-1}]^T. \quad (4.1.8)$$

We apply a standard subspace-based method, like HSVD/HTLS, to the  $K$  dominant left singular vectors of the data matrix  $\bar{\mathbf{H}}$  to compute the set of signal poles

$$Z = \{z_1, \dots, z_K\} \quad (4.1.9)$$

related to the  $K$  signal components. Since we know the approximate frequency locations for the triplet and the two doublets, we can identify which ones of the estimated signal poles correspond to the triplet peak and which ones to the doublet peaks. Then, we can define the following subsets of  $Z$  as

$$Z_2 = Z - \{\text{the doublet peaks } \{z_k\}\}, \quad (4.1.10)$$

$$Z_3 = Z - \{\text{the triplet peak } \{z_k\}\}, \quad (4.1.11)$$

where the set  $Z_2$  contains the  $z_k$  estimates with frequencies not close to any of the considered doublet peaks and  $Z_3$  contains the  $z_k$  estimates with frequencies not close to the triplet peak.

- **Step 2** : Removal of nuisance peaks prior to triplet peak estimation

Before estimating the triplet peak parameters, we have to eliminate the components corresponding to other peaks from the data since they may disturb the triplet peak estimation. Actually, this might be unnecessary for low noise levels provided there are no other triplet peaks in the data satisfying (4.1.3). However, for higher noise levels, large peaks in the data may disturb the triplet peak estimation and, therefore, we first eliminate the non-triplet components in  $Z_3$  from the data matrix by using the technique described in [11]. Specifically, we assume that  $Z_3$  contains  $\bar{m}$  elements, i.e.  $Z_3 = \{\bar{z}_1, \dots, \bar{z}_{\bar{m}}\}$ , and consider the QR decomposition of the following matrix

$$\begin{bmatrix} \mathbf{a}_M(\bar{z}_1) & \cdots & \mathbf{a}_M(\bar{z}_{\bar{m}}) \end{bmatrix} = \begin{bmatrix} \bar{\mathbf{X}} & \bar{\mathbf{Q}} \end{bmatrix} \begin{bmatrix} \bar{\mathbf{R}} \\ \mathbf{0} \end{bmatrix} \quad (4.1.12)$$

where  $\bar{\mathbf{X}}$ ,  $\bar{\mathbf{Q}}$ , and  $\bar{\mathbf{R}}$  have dimensions  $M \times \bar{m}$ ,  $M \times (M - \bar{m})$ ,  $\bar{m} \times \bar{m}$  respectively,  $\bar{\mathbf{Q}}^H \bar{\mathbf{Q}} = \mathbf{I}_{M - \bar{m}}$ .

As  $\bar{\mathbf{Q}}^H \bar{\mathbf{X}} = \mathbf{0}$  by definition, we have

$$\bar{\mathbf{Q}}^H \mathbf{a}_M(z) = \mathbf{0} \text{ for } z = \bar{z}_1, \dots, \bar{z}_{\bar{m}}, \quad (4.1.13)$$

which implies that

$$\begin{aligned} \tilde{\mathbf{H}} &\triangleq \tilde{\mathbf{H}}(\bar{\mathbf{Q}}^H)^T = [\mathbf{a}_L(\check{z}_1) \quad \dots \quad \mathbf{a}_L(\check{z}_{K - \bar{m}})] \cdot \\ &\begin{bmatrix} \check{a}_1 e^{j\check{\phi}_1} & & \mathbf{0} \\ & \ddots & \\ \mathbf{0} & & \check{a}_{K - \bar{m}} e^{j\check{\phi}_{K - \bar{m}}} \end{bmatrix} \begin{bmatrix} \mathbf{a}_M^T(\check{z}_1)(\bar{\mathbf{Q}}^H)^T \\ \vdots \\ \mathbf{a}_M^T(\check{z}_{K - \bar{m}})(\bar{\mathbf{Q}}^H)^T \end{bmatrix}, \end{aligned} \quad (4.1.14)$$

where  $\{\check{z}_1, \dots, \check{z}_{K - \bar{m}}\} = Z - Z_3$ . The matrix  $\tilde{\mathbf{H}}$  no longer contains the components in  $Z_3$ , i.e.  $\tilde{\mathbf{H}}$  only contains the components corresponding to the triplet peak and, possibly, other peaks that are very close to the triplet peak.

- **Step 3** : Damping and frequency estimation of the triplet peak

We compute the SVD of the matrix  $\tilde{\mathbf{H}}$

$$\tilde{\mathbf{H}} = \tilde{\mathbf{U}} \tilde{\mathbf{\Sigma}} \tilde{\mathbf{V}}^H, \quad (4.1.15)$$

where  $\tilde{\mathbf{\Sigma}} = \text{diag}(\tilde{\sigma}_1, \dots, \tilde{\sigma}_{K - \bar{m}})$ ,  $\tilde{\mathbf{U}}^H \tilde{\mathbf{U}} = \mathbf{I}_{K - \bar{m}}$  and  $\tilde{\mathbf{V}}^H \tilde{\mathbf{V}} = \mathbf{I}_{K - \bar{m}}$ .

We define the orthogonal projection matrix onto the nullspace of  $\tilde{\mathbf{U}}^H$

$$\tilde{\mathbf{\Pi}} = \mathbf{I} - \tilde{\mathbf{U}} \tilde{\mathbf{U}}^H. \quad (4.1.16)$$

It is well known that the vectors  $\{\mathbf{a}_L(\check{z}_k)\}_{k=1}^{K - \bar{m}}$  span the range space of  $\tilde{\mathbf{U}}$  (see, e.g., [59]) and hence

$$\sum_{k=1}^{K - \bar{m}} \mathbf{a}_L^H(\check{z}_k) \tilde{\mathbf{\Pi}} \mathbf{a}_L(\check{z}_k) = \mathbf{0}. \quad (4.1.17)$$

Since for the noise-free case  $\{z_1, z_2, z_3\} \subset \{\tilde{z}_1, \dots, \tilde{z}_{K-\bar{m}}\}$ , where  $\{z_1, z_2, z_3\}$  are the signal poles associated with the triplet peak, we have

$$\sum_{k=1}^3 \mathbf{a}_L^H(z_k) \tilde{\mathbf{\Pi}} \mathbf{a}_L(z_k) = 0. \quad (4.1.18)$$

Let

$$\tilde{\mathbf{\Gamma}} = \tilde{\mathbf{\Pi}} + \mathbf{D} \tilde{\mathbf{\Pi}} \mathbf{D}^H + \mathbf{D}^2 \tilde{\mathbf{\Pi}} (\mathbf{D}^H)^2, \quad (4.1.19)$$

where  $\mathbf{D}$  is defined as follows

$$\mathbf{D} = \text{diag} \left( 1, e^{-j2\pi\Delta f\Delta t}, \dots, e^{-j(L-1)2\pi\Delta f\Delta t} \right) \quad (4.1.20)$$

As

$$\mathbf{a}_L(z_2) = \mathbf{D}^H \mathbf{a}_L(z_1), \quad \mathbf{a}_L(z_3) = (\mathbf{D}^H)^2 \mathbf{a}_L(z_1),$$

it follows from (4.1.18) that

$$\mathbf{a}_L(z_1) \in \text{nullspace}(\tilde{\mathbf{\Gamma}}), \quad (4.1.21)$$

and it can be shown that

$$\dim[\text{nullspace}(\tilde{\mathbf{\Gamma}})] = 1. \quad (4.1.22)$$

Let  $\mathbf{w}$  denote the  $L \times 1$  vector that spans the null space of  $\tilde{\mathbf{\Gamma}}$ . In view of (4.1.21) and (4.1.22), we have that

$$\mathbf{a}_L(z_1) = \rho \mathbf{w}, \quad (4.1.23)$$

for some scalar  $\rho \neq 0$ . We define the following sub-vectors of  $\mathbf{a}_L(z)$

$$\mathbf{a}_\downarrow(z) = [\mathbf{I}_{L-1} \quad \mathbf{0}] \mathbf{a}_L(z), \quad (4.1.24)$$

$$\mathbf{a}^\uparrow(z) = [\mathbf{0} \quad \mathbf{I}_{L-1}] \mathbf{a}_L(z), \quad (4.1.25)$$

and similarly for  $\mathbf{w}$ . As  $\mathbf{a}^\uparrow(z) = z \mathbf{a}_\downarrow(z)$ , we derive from (4.1.23) that

$$\rho \mathbf{w}^\uparrow = z_1 \rho \mathbf{w}_\downarrow \iff \mathbf{w}^\uparrow = z_1 \mathbf{w}_\downarrow \quad (4.1.26)$$

and hence  $z_1$  can be obtained as

$$z_1 = \frac{\mathbf{w}_\downarrow^H \mathbf{w}^\uparrow}{\mathbf{w}_\downarrow^H \mathbf{w}_\downarrow}. \quad (4.1.27)$$

For noisy data, we compute the matrix  $\tilde{\mathbf{U}}$  made from the  $\max\{K - \bar{m}, 3\}$  left singular vectors of  $\tilde{\mathbf{H}}$  associated with the largest singular values. The vector  $\mathbf{w}$  is the eigenvector of the matrix  $\tilde{\mathbf{\Gamma}}$  associated with the smallest eigenvalue. We use the estimate  $z_1$  along with Eq.(4.1.3) to estimate  $z_2 = z_1 e^{j2\pi\Delta f\Delta t}$  and  $z_3 = z_1 e^{j4\pi\Delta f\Delta t}$ .

Note that the above value  $z_1$  was computed as the LS solution of Eq.(4.1.26). It is possible to solve Eq.(4.1.26) in the TLS sense [73], which results in more accurate final parameter estimates. For clarity of exposition, we show here how to compute  $z_1$  as the TLS solution of Eq.(4.1.26)

- arrange the vectors  $\mathbf{w}^\dagger$  and  $\mathbf{w}_\downarrow$  in matrix form

$$[\mathbf{w}_\downarrow, \mathbf{w}^\dagger]$$

- compute the SVD of the matrix  $[\mathbf{w}_\downarrow, \mathbf{w}^\dagger]$

$$[\mathbf{w}_\downarrow, \mathbf{w}^\dagger] = \mathbf{U}_w \mathbf{\Sigma}_w \mathbf{V}_w^H,$$

where  $\mathbf{V}_w$  has dimension  $2 \times 2$

- TLS solution:

$$z_1 = -\frac{\mathbf{V}_w(1, 2)}{\mathbf{V}_w(2, 2)},$$

where we used the Matlab notation to denote the  $\mathbf{V}_w$  matrix elements.

Using TLS instead of LS, as above, we obtain a variant of the KNOB–SVD method, called KNOB–TLS, which will be used in Section 4.2 and Section 4.3 for the simulation and *in vivo* studies.

- **Step 4** : Removal of nuisance peaks prior to doublet peak estimation

Before estimating the doublet peaks, we need to eliminate the triplet peak from the data since, in the theoretical development of the step dealing with the doublet peaks, we assume that there is no other doublet peak in the signal spectrum with the same damping and frequency separation. This assumption would be violated if the triplet peak was not eliminated. Also, for the noisy case, non–doublet peaks might disturb the estimation of the doublet peaks and, therefore, we want to eliminate those peaks as well. To eliminate the nuisance components from the data matrix  $\tilde{\mathbf{H}}$  prior to the doublet peak estimation, we use the same technique as for Step 2, but we replace  $Z_3$  by  $Z_2$  and we let  $\check{\mathbf{H}}$  denote the output matrix.

- **Step 5** : Damping and frequency estimation of the doublet peaks

We consider the SVD of the matrix  $\check{\mathbf{H}}$  provided by the previous step

$$\check{\mathbf{H}} = \check{\mathbf{U}} \check{\mathbf{\Sigma}} \check{\mathbf{V}}^H, \quad (4.1.28)$$

where  $\check{\Sigma} = \text{diag}(\check{\sigma}_1, \dots, \check{\sigma}_{K-\check{m}})$ ,  $\check{\mathbf{U}}^H \check{\mathbf{U}} = \mathbf{I}_{K-\check{m}}$  and  $\check{\mathbf{V}}^H \check{\mathbf{V}} = \mathbf{I}_{K-\check{m}}$ , and  $\check{m}$  represents the number of elements in  $\Lambda_2$ . Let

$$\check{\mathbf{\Pi}} = \mathbf{I} - \check{\mathbf{U}} \check{\mathbf{U}}^H. \quad (4.1.29)$$

A procedure similar to (4.1.18) – (4.1.21) shows that for the noise free case

$$\mathbf{a}_L(z_4), \mathbf{a}_L(z_6) \in \text{nullspace}(\check{\mathbf{\Gamma}}), \quad (4.1.30)$$

where

$$\check{\mathbf{\Gamma}} = \check{\mathbf{\Pi}} + \mathbf{D} \check{\mathbf{\Pi}} \mathbf{D}^H, \quad (4.1.31)$$

with

$$\dim[\text{nullspace}(\check{\mathbf{\Gamma}})] = 2. \quad (4.1.32)$$

Let  $\{\mathbf{w}_1, \mathbf{w}_2\}$  denote the  $L \times 1$  vectors that span the null space of  $\check{\mathbf{\Gamma}}$ . In view of [4.1.30], we have that

$$\begin{bmatrix} \mathbf{a}_L(z_4) & \mathbf{a}_L(z_6) \end{bmatrix} = \mathbf{W} \mathbf{P}, \quad (4.1.33)$$

where  $\mathbf{P}$  is a  $2 \times 2$  nonsingular matrix and

$$\mathbf{W} = \begin{bmatrix} \mathbf{w}_1 & \mathbf{w}_2 \end{bmatrix}. \quad (4.1.34)$$

We define:

$$\mathbf{W}_\downarrow = [\mathbf{I}_{L-1} \ \mathbf{0}] \mathbf{W}, \quad (4.1.35)$$

$$\mathbf{W}^\uparrow = [\mathbf{0} \ \mathbf{I}_{L-1}] \mathbf{W}. \quad (4.1.36)$$

Then, it follows from (4.1.33) that

$$\mathbf{W}^\uparrow \mathbf{P} = \mathbf{W}_\downarrow \mathbf{P} \begin{bmatrix} z_4 & 0 \\ 0 & z_6 \end{bmatrix} \iff \mathbf{W}^\uparrow = \mathbf{W}_\downarrow \mathbf{\Psi}, \quad (4.1.37)$$

where

$$\mathbf{\Psi} = \mathbf{P} \begin{bmatrix} z_4 & 0 \\ 0 & z_6 \end{bmatrix} \mathbf{P}^{-1}. \quad (4.1.38)$$

We can obtain  $\mathbf{\Psi}$  from (4.1.37) as follows

$$\mathbf{\Psi} = (\mathbf{W}_\downarrow^H \mathbf{W}_\downarrow)^{-1} \mathbf{W}_\downarrow^H \mathbf{W}^\uparrow, \quad (4.1.39)$$

and, then, obtain  $z_4$  and  $z_6$  as the eigenvalues of  $\mathbf{\Psi}$ .

As in Step 3, we can solve Eq.(4.1.37) in the TLS sense

- arrange the matrices  $\mathbf{W}^\dagger$  and  $\mathbf{W}_\downarrow$  in a new matrix, i.e.

$$[\mathbf{W}_\downarrow, \mathbf{W}^\dagger]$$

- compute the SVD of the matrix  $[\mathbf{W}_\downarrow, \mathbf{W}^\dagger]$

$$[\mathbf{W}_\downarrow, \mathbf{W}^\dagger] = \mathbf{U}_\mathbf{W} \mathbf{\Sigma}_\mathbf{W} \mathbf{V}_\mathbf{W}^H,$$

where  $\mathbf{V}_\mathbf{W}$  has dimension  $4 \times 4$

- TLS solution:

$$\mathbf{\Psi} = -\mathbf{V}_\mathbf{W}(1:2, 3:4)(\mathbf{V}_\mathbf{W}(3:4, 3:4))^{-1},$$

where we used the Matlab notation to denote the  $\mathbf{V}_\mathbf{W}$  matrix blocks.

For noisy data we compute the matrix  $\check{\mathbf{U}}$  made from the  $\max\{K - \check{m}, 4\}$  left singular vectors of  $\check{\mathbf{H}}$  associated with the largest singular values. The vectors  $\{\mathbf{w}_1, \mathbf{w}_2\}$  are the eigenvectors of the matrix  $\check{\mathbf{I}}$  associated with the smallest eigenvalues. We use the estimates of  $z_4$  and  $z_6$  along with (4.1.4) to estimate  $z_5 = z_4 e^{j2\pi\Delta f\Delta t}$  and  $z_7 = z_6 e^{j2\pi\Delta f\Delta t}$ .

- **Step 6** : Removal of the estimated multiplet peaks

As already specified, the signal we are considering may contain other peaks besides the seven ATP peaks (the triplet and two doublets) we have already estimated. In order to improve the estimation of the remaining  $K - 7$  peaks, we eliminate the 7 estimated peaks from the original data matrix  $\check{\mathbf{H}}$  and re-estimate the parameters of the remaining peaks.

Once again we apply the same technique used in Step 2 by replacing  $Z_3$  with

$$Z_{known} = \{z_1, \dots, z_7\} \quad (4.1.40)$$

and denoting the output data matrix as  $\check{\mathbf{H}}_{K-7}$ .

- **Step 7** : Damping and frequency estimation of the remaining  $K - 7$  peaks

Similarly to Step 1, we apply a standard HSVD/HTLS method to the  $K - 7$  dominant left singular vectors of the data matrix  $\check{\mathbf{H}}_{K-7}$  to re-estimate  $\{z_8, \dots, z_K\}$ .

- **Step 8** : Amplitude estimation

Once the signal poles  $z_k$ ,  $k = 1, \dots, K$ , have been estimated, we can compute the amplitude estimates. Let

$$\mathbf{y} = [y_0 \quad \dots \quad y_{N-1}]^T \quad (4.1.41)$$

denote the data vector.

By using the amplitude and phase constraints (4.1.5) into the model equation Eq.(4.1.1), we obtain (in the noise-free case)

$$\begin{aligned}
\mathbf{y} &= [\mathbf{a}_N(z_1) \dots \mathbf{a}_N(z_K)] \begin{bmatrix} a_1 e^{j\phi_1} \\ \vdots \\ a_K e^{j\phi_K} \end{bmatrix} \\
&= \left[ \left\{ \frac{1}{2} \mathbf{a}_N(z_1) + \mathbf{a}_N(z_2) + \frac{1}{2} \mathbf{a}_N(z_3) + \mathbf{a}_N(z_4) + \dots + \mathbf{a}_N(z_7) \right\}, \mathbf{a}_N(z_8), \dots, \mathbf{a}_N(z_K) \right] \begin{bmatrix} a e^{j\phi} \\ a_8 e^{j\phi_8} \\ \vdots \\ a_K e^{j\phi_K} \end{bmatrix} \\
&\triangleq \mathbf{A} \Theta.
\end{aligned} \tag{4.1.42}$$

From the least-squares estimate of  $\Theta$  above

$$\Theta = (\mathbf{A}^H \mathbf{A})^{-1} \mathbf{A}^H \mathbf{y}, \tag{4.1.43}$$

we directly obtain the estimates for the amplitudes  $\{a_k\}_{k=1}^K$  and phases  $\{\phi_k\}_{k=1}^K$ .

#### 4.1.2 Outline of the KNOB-TLS algorithm

Here we summarize the computations required by KNOB-TLS.

##### Outline of the KNOB – TLS algorithm

- **Step 1** : Damping and frequency estimation of all peaks
  - Compute  $Z$  defined in (4.1.9) using a standard HTLS method.
  - Extract  $Z_2$  and  $Z_3$  from the signal pole estimates in  $Z$ .
- **Step 2** : Removal of nuisance peaks prior to triplet peak estimation
  - Use the estimates  $\{\bar{z}_1, \dots, \bar{z}_{\bar{m}}\} = Z_3$ , obtained in Step 1, to compute the QR decomposition in (4.1.12) and hence obtain  $\bar{\mathbf{Q}}$ .
  - Compute the  $L \times (M - \bar{m})$  matrix  $\tilde{\mathbf{H}}$ , as in (4.1.14), from which the components outside the triplet region have been eliminated.
- **Step 3** : Damping and frequency estimation of the triplet peak
  - Compute the matrix  $\tilde{\mathbf{U}}$  consisting of the  $\max\{K - \bar{m}, 3\}$  left singular vectors of  $\tilde{\mathbf{H}}$  associated with the largest singular values.
  - Compute  $\tilde{\mathbf{\Gamma}}$  defined in (4.1.19) and its eigenvector  $\mathbf{w}$  associated with the smallest eigenvalue.

- Solve Eq.(4.1.26) in a TLS sense to obtain  $z_1$ . Use the estimate of  $z_1$  along with (4.1.3) to estimate  $z_2 = z_1 e^{j2\pi\Delta f\Delta t}$  and  $z_3 = z_1 e^{j4\pi\Delta f\Delta t}$ .
- **Step 4** : Removal of nuisance peaks prior to doublet peak estimation
  - Use the estimates  $\{\check{z}_1, \dots, \check{z}_{\check{m}}\} = Z_2$ , obtained in Step 1, to compute a QR decomposition similar to (4.1.12) and hence obtain  $\check{\mathbf{Q}}$ .
  - Compute the  $L \times (M - \check{m})$  matrix  $\check{\mathbf{H}}$  from which the components outside the doublet regions have been eliminated.
- **Step 5** : Damping and frequency estimation of the doublet peaks
  - Compute the matrix  $\check{\mathbf{U}}$  consisting of the  $\max\{K - \check{m}, 4\}$  left singular vectors of  $\check{\mathbf{H}}$  associated with the largest singular values.
  - Compute  $\check{\mathbf{\Gamma}}$  defined in (4.1.31) and its eigenvectors  $\mathbf{w}_1, \mathbf{w}_2$  associated with the two smallest eigenvalues.
  - Solve Eq.(4.1.37) in a TLS sense to obtain the  $2 \times 2$  matrix  $\Psi$  and take its two eigenvalues as estimates of  $z_4$  and  $z_6$ . Use the estimates of  $z_4$  and  $z_6$  along with (4.1.4) to estimate  $z_5 = z_4 e^{j2\pi\Delta f\Delta t}$  and  $z_7 = z_6 e^{j2\pi\Delta f\Delta t}$ .
- **Step 6** : Removal of the estimated multiplet peaks
  - Use the estimates of  $\{z_k\}_{k=1}^7$ , obtained in Step 3 and 5, to compute a QR decomposition as in (4.1.12) and, hence, to compute the  $L \times (M - 7)$  matrix  $\check{\mathbf{H}}_{K-7}$  from which the ATP peak components have been eliminated.
- **Step 7** : Damping and frequency estimation of the remaining  $K - 7$  peaks
  - Similarly to Step 1, apply a standard HTLS method to the  $K - 7$  dominant left singular vectors of the data matrix  $\check{\mathbf{H}}_{K-7}$  to re-estimate  $\{z_k\}_{k=8}^K$ .
- **Step 8** : Amplitude estimation
  - Use the amplitude and phase constraints (4.1.5) into the model equation to obtain the system of linear equations  $\mathbf{A}\Theta = \mathbf{y}$ , as defined in (4.1.42), where  $\mathbf{y}$  represents the data vector.
  - Compute the least-squares solution of the system  $\mathbf{A}\Theta = \mathbf{y}$  in order to obtain the amplitude and phase estimates.

**Remark** : This algorithm can be easily adapted for quantification of other signals with multiplet structure by combining, modifying and deleting the above steps in an appropriate way. For example, quantification of a proton MRS signal exhibiting

a lactate doublet involves the execution of Steps 1, 4 (restricted to one doublet), 5, 6 and 7 with proper specification of the amplitude and phase constraints.

## 4.2 Quantification of a simulated MRS signal

We consider the simulated signal introduced in Section 3.6.1. It is derived from an *in vivo*  $^{31}\text{P}$  spectrum measured in the human brain and consists of 256 complex data points and 11 exponentials, as defined in [69]. In Table 5.1 the parameters of the noiseless simulated signal are displayed and Figure 3.1 shows the real part of the Discrete Fourier Transform (DFT) of the simulated signal when it is perturbed by additive complex white noise with a circular Gaussian distribution with standard deviation  $\sigma = 15$ . The first seven peaks (denoted by  $\beta$ -ATP,  $\alpha$ -ATP and

peak $k$	$f_k(\text{Hz})$	$f_k(\text{ppm})$	$d_k(\text{Hz})$	$a_k(\text{a.u.})$	$\phi_k(^{\circ})$
1	-86	-17.2	50	75	135
2	-70	-16.6	50	150	135
3	-54	-16.0	50	75	135
4	152	-8.0	50	150	135
5	168	-7.4	50	150	135
6	292	-2.6	50	150	135
7	308	-2.0	50	150	135
8	360	0.0	25	150	135
9	440	3.1	285.7	1400	135
10	490	5.0	25	60	135
11	530	6.6	200	500	135

**Table 4.1.** True parameter values of the simulated  $^{31}\text{P}$  MRS signal.

$\gamma$ -ATP, respectively, in Figure 3.1) represent the ATP complex. We note that the ATP complex contains one triplet peak,  $\beta$ -ATP, and two doublet peaks,  $\alpha$ -ATP and  $\gamma$ -ATP, which clearly satisfy the aforementioned properties (4.1.3), (4.1.4) and (4.1.5). The  $\beta$ -ATP peak was approximated as a triplet in our *in vivo* examples. For highly-resolved signals of tissues with known differences in the ATP phosphorus  $\alpha - \beta$  and  $\gamma - \beta$  coupling constants, the  $\beta$ -ATP peak should be treated as a doublet of a doublet with the appropriate prior knowledge concerning the coupling constants, insofar available. The sampling frequency is  $f_s = 3\text{kHz}$  and the frequency separation of the ATP peaks is  $\Delta f = 16\text{Hz}$ . In this section we compare the performances of the subspace-based methods KNOB-TLS, HTLS, HTLSPK( $\Delta f_{dq}$ ) and the optimization-based method AMARES when considering the full  $^{31}\text{P}$  signal, whose first seven peaks, i.e. the ATP complex, satisfy the prior knowledge specified by the relations (4.1.3), (4.1.4) and (4.1.5). Before describing the simulation studies, we would like to remind the reader that the method AMARES is initialized by using the “peak picking” technique, as already pointed out in Section

2.4. Moreover, it is important to note that the method HTLSPK( $\Delta fd_{eq}$ ) can only exploit the type of prior knowledge considered in (4.1.2) for the doublet peaks, but not for triplet peaks. However, the method can be applied to the given signal by modelling the ATP triplet peak as two doublet peaks sharing the center peak. In the following, the method HTLSPK( $\Delta fd_{eq}$ ) will be denoted by HTLSPK to simplify the notation.

We consider Eq.(4.1.1) with  $a_k$ ,  $\phi_k$ ,  $d_k$  and  $f_k$ ,  $k = 1, \dots, 11$ , as given in Table 4.1, and perturb the signal by adding white Gaussian noise with standard deviation  $\sigma$  on the real and the imaginary components separately. Our goal is to recover the parameters  $a_k$ ,  $\phi_k$ ,  $d_k$  and  $f_k$ ,  $k = 1, \dots, 11$ , characterizing the signal  $\{y_n\}_{n=0}^{N-1}$ , and compare the performances of KNOB-TLS, HTLS, HTLSPK and AMARES in terms of robustness and statistical accuracy. The robustness of each method is evaluated by computing its success rate, i.e. the number of times, out of the total number of simulation runs, the method is able to resolve the 11 peaks within specific intervals lying symmetrically around the true frequencies of the peaks. The halfwidths of these intervals are set to 8Hz, i.e. half the separation of the closest peaks in the data. Concerning the statistical accuracy, this is measured as the mean Relative Root Mean Squared Error (mean RRMSE):

$$\text{mean RRMSE} \equiv \frac{100}{K} \sum_{k=1}^K \sqrt{\frac{1}{J} \sum_{j=1}^J \frac{(\hat{p}_{k,j} - p_k)^2}{p_k^2}} \quad (\%) \quad (4.2.44)$$

for the amplitude and damping estimates, and as the mean Root Mean Squared Error (mean RMSE):

$$\text{mean RMSE} \equiv \frac{1}{K} \sum_{k=1}^K \sqrt{\frac{1}{J} \sum_{j=1}^J (\hat{p}_{k,j} - p_k)^2} \quad (4.2.45)$$

for the frequency and phase estimates, where  $K$  is the total number of peaks ( $K = 11$ ),  $J$  is the number of simulation runs in which the method was able to find every peak within the corresponding frequency interval,  $\hat{p}_{k,j}$  denotes the parameter estimate of the  $k$ th peak obtained in simulation run  $j$ , and  $p_k$  denotes the true parameter value of the  $k$ th peak. We only take into account the results related to those cases for which we have a success rate of at least 5% (i.e.  $J \geq 50$  when performing 1000 simulation runs), in order to prevent showing mean RRMSE and mean RMSE values which are based on too few estimates. In Figure 4.1 the success rate and the amplitude mean RRMSE values for the ATP complex for different noise levels are displayed.

We can observe that the method KNOB-TLS is much more robust than the other two subspace-based methods HTLS and HTLSPK, and it also provides amplitude estimates whose quality is much better than that of the HTLS estimates. Note that HTLSPK seems better than KNOB-TLS in accuracy, but this is due to the fact that only the successful runs (much fewer for HTLSPK) have been considered in the

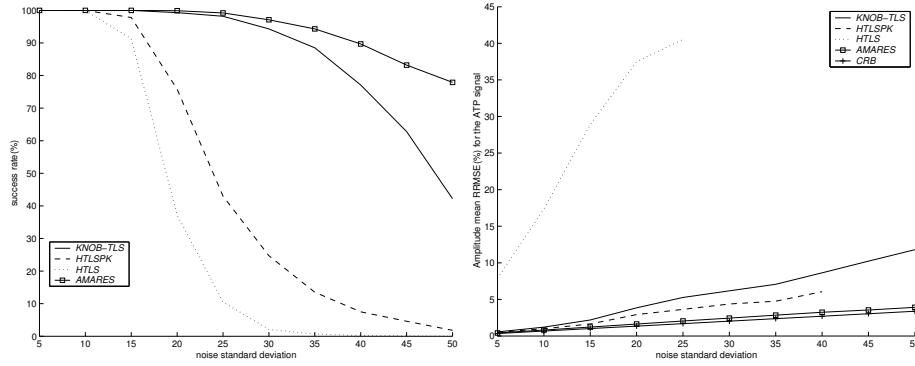


**Figure 4.1.** Left: success rate as a function of the noise standard deviation  $\sigma$  for the  $^{31}\text{P}$  signal. Right: mean RRMSE of amplitude estimates as a function of the noise standard deviation  $\sigma$  for the ATP complex.

plot. Moreover, we can also observe that KNOB-TLS is not able to outperform the optimization-based method AMARES, whose success rate is the highest and whose mean RRMSEs more closely approach the CRBs. In Figures 4.2 and 4.3 the mean RMSE values for the frequency estimates, the mean RRMSE values for damping factor estimates and the mean RMSE values for phase estimates are shown.

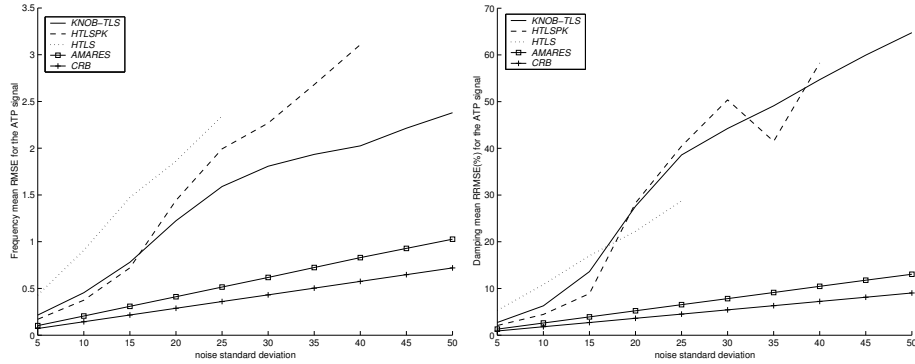


**Figure 4.2.** Left: mean RMSE of frequency estimates as a function of the noise standard deviation  $\sigma$  for the ATP complex. Right: mean RRMSE of damping factor estimates as a function of the noise standard deviation  $\sigma$  for the ATP complex.

From Figure 4.2 (left) we can notice that the frequency estimates are characterized by low mean RMSE values for all considered methods and that, in particular, KNOB-TLS is more accurate than HTLSPK and HTLS. Similar results can be observed for phases in Figure 4.3, where we can also notice that the performance of the HTLS method gets even worse. Finally, in Figure 4.2 (right) we can see that

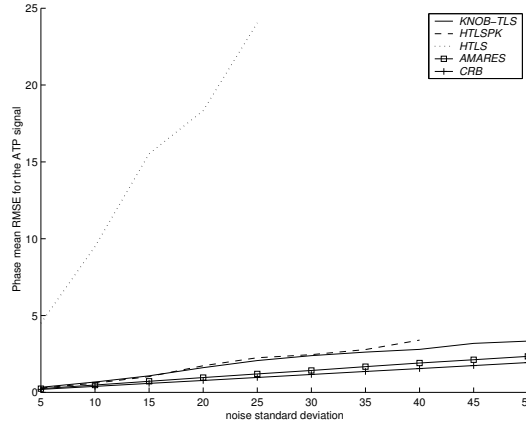


**Figure 4.3.** Mean RMSE of phase estimates as a function of the noise standard deviation  $\sigma$  for the ATP complex.

KNOB-TLS and HTLSPK damping factor estimates are characterized by large variances (high mean RRMSEs) compared to AMARES, which points out a loss of accuracy for both methods when estimating the damping factors.

Concerning the computational efficiency, the average number of flops over 1000 simulation runs for the considered subspace-based methods was computed for different lengths of the signal, as given by the number of data points  $N$ . The noise standard deviation was set to  $\sigma = 15$ . The method AMARES has not been taken into account in the present comparison since the available code is written in Fortran, which does not allow the count of the number of flops. In Table 4.2 the ratio between the average number of flops of the two methods KNOB-TLS, HTLSPK and the average number of flops of HTLS is reported.

$N$	$\frac{\text{KNOB-TLS}}{\text{HTLS}}$	$\frac{\text{HTLSPK}}{\text{HTLS}}$
256	9.3651	6.6832
1024	9.7731	6.8342
2048	9.7852	6.8491

**Table 4.2.** Ratio between the average number of flops over 1000 simulation runs for different lengths of the signal.

We observe that KNOB-TLS is about 1.5 times computationally more intensive than HTLSPK and that for all methods the ratio slightly increases with the length of the signal  $N$ . The efficiency of KNOB-TLS can be improved by using the Lanczos algorithm with partial reorthogonalization or the implicitly restarted Lanczos algorithm, introduced in Chapter 3 [35], in order to compute the truncated SVDs, which represent the computationally most intensive part of the algorithm.

We would like to conclude this section by describing the performance improvements which one can expect by using the TLS-based variant KNOB-TLS of the originally proposed method KNOB-SVD. We remind the reader that the difference between the two versions consists of computing the TLS solutions of Eq.(4.1.26) and Eq.(4.1.37) instead of the LS solutions. In Figure 4.4 the amplitude (left) and damping (right) mean RRMSE values for the proposed method are reported when considering the two different variants: KNOB-SVD and KNOB-TLS. We can observe that the TLS variant provides amplitude and damping factor estimates whose quality is slightly better than that of the LS variant.

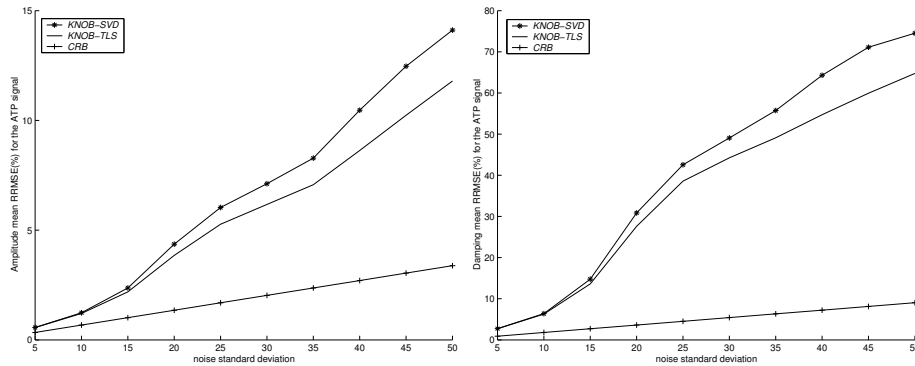


**Figure 4.4.** Mean RRMSE of amplitude estimates (left) and damping estimates (right) as computed by KNOB-SVD and its TLS variant KNOB-TLS, as a function of the noise standard deviation  $\sigma$  for the ATP complex.

### 4.3 Quantification of *In vivo* MRS signals

#### 4.3.1 *In vivo* $^{31}\text{P}$ signals

As a first example of quantification of *in vivo* MRS signals, we consider 21  $^{31}\text{P}$  signals, which are free-induction decay signals acquired after a single pulse (64 averages), obtained from the resting calf muscle of healthy humans and recorded at 81.1MHz (4.7T Bruker Biospec) using a 5cm diameter surface coil positioned against the calf muscle. Each signal consists of 2048 complex data points in the time domain and is assumed to be modeled by Eq.(4.1.1) with model order  $K = 9$ . The sampling time is 0.25ms and only 512 data samples are considered (the remaining ones contain only noise), starting from the 5th point of the signal (the first 4 data samples are excluded in order to eliminate the hump characterizing the original spectra). The same data samples are used in the KNOB-TLS, KNOB-SVD, HTLSPK, HTLS and AMARES estimation algorithms for the quantification of the given signals. The method AMARES is initialized by using the “peak picking” technique applied

to one of the available signals. The prior knowledge about amplitudes and phases we assume in this section slightly differs from (4.1.5) since the signals also contain the adenosine diphosphate complex, commonly called ADP, which distorts the original ATP signal. More precisely, we consider as prior knowledge for the  $\beta$ -ATP triplet peak:

$$2a_1 = a_2 = 2a_3, \quad \phi_1 = \phi_2 = \phi_3, \quad (4.3.46)$$

for the first  $\alpha$ -ATP doublet peak:

$$a_4 = a_5, \quad \phi_4 = \phi_5, \quad (4.3.47)$$

and for the second  $\gamma$ -ATP doublet peak:

$$a_6 = a_7, \quad \phi_6 = \phi_7. \quad (4.3.48)$$

Regarding the prior knowledge in (4.1.3) and (4.1.4), here  $\Delta f$  is equal to 16Hz. The approximate frequency locations for all ATP peaks are known as well:  $\beta$ -ATP (-1129Hz, -16.2ppm; -1113Hz, -16.0ppm; -1097Hz, -15.8ppm),  $\alpha$ -ATP(-426Hz, -7.6ppm; -410Hz, -7.4ppm) and  $\gamma$ -ATP(-20Hz, -2.6ppm; -4Hz, -2.4ppm). In order to compare the performance of various methods in terms of accuracy, we need the true parameter values which, unfortunately, are not known in practical applications. However, we can consider as accurate estimates of the true parameters those determined by AMARES. Our studies show that the parameter estimates provided by the method KNOB-TLS are the closest to the AMARES estimates. More precisely, the methods KNOB-TLS and KNOB-SVD are always able to resolve correctly the first 8 peaks ( $\beta$ -ATP,  $\alpha$ -ATP,  $\gamma$ -ATP and PCr), but not always the 9th one (Pi), the reason being that the Pi peak was almost inexistent in some of the spectra, while prominent in others, reflecting the biological variation of the concentration of muscle Pi in individuals. The methods HTLSPK and HTLS are not able to provide acceptable estimates, i.e., their frequency estimates do not fall within the frequency intervals lying symmetrically around the AMARES estimates and with halfwidths equal to 8Hz. The method HTLSPK is sometimes able to resolve the  $\alpha$ -ATP and  $\gamma$ -ATP doublets and the PCr peak, but never the  $\beta$ -ATP triplet and the Pi peak; HTLS never resolves the triplet and doublets. Figure 4.5 shows results of quantifying one of the available  $^{31}\text{P}$  MRS signals by AMARES and KNOB-TLS. In Tables 4.3 and 4.4 the mean Relative Root Mean Square Difference values (mean RRMSD) for the amplitude and the damping parameter estimates, and the mean Root Mean Square Difference (mean RMSD) values for the frequency and phase parameter estimates are reported. They are obtained for the ATP triplet and doublets by processing the available 21 signals. The formulas used to compute the mean RRMSDs and the mean RMSDs are respectively:

$$\text{mean RRMSD} \equiv \frac{100}{K} \sum_{k=1}^K \sqrt{\frac{1}{J} \sum_{j=1}^J \frac{(\hat{p}_{k,j} - p_{k,j})^2}{p_{k,j}^2}} \quad (\%) \quad (4.3.49)$$

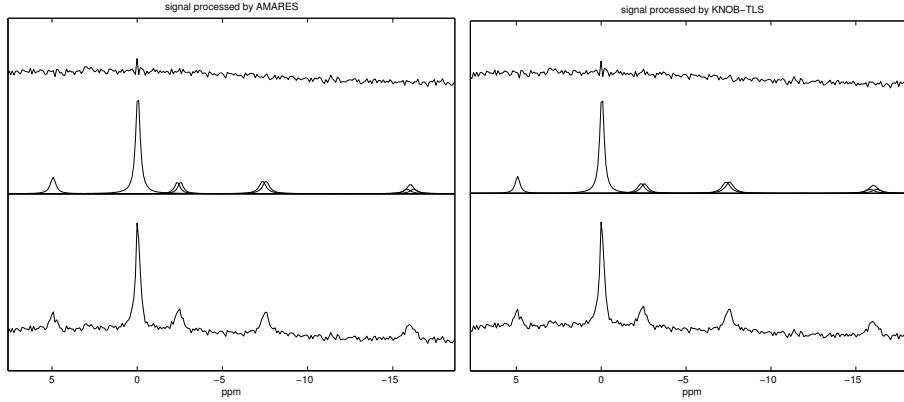


**Figure 4.5.** Bottom: real part of the original  $^{31}\text{P}$  signal spectrum; middle: real part of the spectra of the individual peaks estimated by AMARES (left) and KNOB-TLS (right); top: real part of the residual signal spectrum after estimation with AMARES (left) and KNOB-TLS (right).

and

$$\text{mean RMSD} \equiv \frac{1}{K} \sum_{k=1}^K \sqrt{\frac{1}{J} \sum_{j=1}^J (\hat{p}_{k,j} - p_{k,j})^2}, \quad (4.3.50)$$

where  $K$  is the number of peaks,  $J$  is the total number of processed *in vivo* signals ( $J = 21$ ),  $\hat{p}_{k,j}$  denotes the parameter estimate of the  $k$ th peak obtained when processing the  $j$ th signal by one of the blackbox methods, and  $p_{k,j}$  denotes the AMARES parameter estimate of the  $k$ th peak for the  $j$ th signal. The tables also report the minimum (m) and maximum (M) relative difference values (for the amplitude and the damping estimates) and the minimum (m) and maximum (M) difference values (for the frequency and phase estimates) for each method. It is observed that KNOB-TLS is more accurate than KNOB-SVD, HTLSPK and HTLS: its mean RRMSD and mean RMSD values are generally the smallest.

### 4.3.2 *In vivo* $^1\text{H}$ signals

As a second example of quantification of *in vivo* MRS signals, we consider a long echo-time proton signal from a  $7.5\text{cm}^3$  volume in the white matter of the brain of a 3.5 years old child with leukodystrophy, acquired at 63.6MHz on a 1.5T Siemens Sonata scanner using the STEAM sequence (TR/TE/TM=2000/135/30ms) and CHES water suppression. The data consist of 1024 complex points in the time domain and the sampling time is 1ms. Only 512 data points are considered in the analysis (the remaining ones contain only noise) starting from the second one (the first one is excluded to eliminate the hump characterizing the original spectrum).

peak	Method	$f_k$ mean RMSD [m,M]	$d_k$ mean RRMSD [m,M] (%)
$\beta$ -ATP	KNOB-TLS	0.64 [0.03, 1.45]	33.91 [20.49, 50.73]
	KNOB-SVD	0.88 [0.07, 2.29]	35.95 [21.88, 53.56]
	HTLSPK	323.66 [5.65, 393.28]	23.94 [8.23, 34.11]
	HTLS	529.61 [0.07, 1085.31]	60.46 [3.14, 111.98]
$\alpha$ -ATP	KNOB-TLS	0.75 [0.02, 1.55]	15.58 [8.10, 27.13]
	KNOB-SVD	0.74 [0.06, 1.53]	16.39 [8.81, 29.48]
	HTLSPK	346.85 [6.81, 424.20]	12.73 [2.24, 30.36]
	HTLS	307.15 [6.52, 612.93]	36.59 [0.13, 101.09]
$\gamma$ -ATP	KNOB-TLS	2.48 [0.12, 6.05]	51.38 [5.01, 91.78]
	KNOB-SVD	2.30 [0.13, 5.38]	59.41 [11.19, 102.54]
	HTLSPK	908.64 [2.80, 1710.04]	449.61 [15.60, 1892.90]
	HTLS	278.85 [179.38, 590.50]	55.42 [2.01, 103.32]

**Table 4.3.** Mean RMSD values and minimum and maximum difference values of the frequency and phase estimates for *in vivo*  $^{31}\text{P}$  MRS signals measured from the calf muscle of healthy humans.

peak	Method	$a_k$ mean RRMSD [m,M] (%)	$\phi_k$ mean RMSD [m,M]
$\beta$ -ATP	KNOB-TLS	16.52 [9.13, 23.07]	1.23 [0.09, 2.67]
	KNOB-SVD	17.61 [10.32, 24.56]	1.36 [0.07, 2.83]
	HTLSPK	72.81 [8.57, 99.26]	126.69 [8.88, 169.75]
	HTLS	213.51 [87.62, 460.38]	66.08 [0.02, 207.52]
$\alpha$ -ATP	KNOB-TLS	8.68 [2.33, 13.49]	2.34 [0.02, 4.66]
	KNOB-SVD	9.11 [3.02, 14.40]	2.45 [0.03, 4.70]
	HTLSPK	19.47 [0.33, 50.09]	15.87 [0.38, 39.90]
	HTLS	185.51 [10.24, 555.47]	39.72 [0.11, 210.73]
$\gamma$ -ATP	KNOB-TLS	27.98 [3.52, 54.47]	5.93 [0.19, 12.60]
	KNOB-SVD	31.60 [5.58, 56.60]	5.65 [0.10, 13.27]
	HTLSPK	118.74 [23.20, 413.71]	97.32 [5.20, 231.77]
	HTLS	344.52 [6.42, 799.84]	41.12 [0.11, 163.09]

**Table 4.4.** Mean RRMSD values and minimum and maximum relative difference values of the amplitude and damping estimates for *in vivo*  $^{31}\text{P}$  MRS signals measured from the calf muscle of healthy humans.

The signal is characterized by the presence of the following compounds: inverted Lactate doublet (Lac), N-Acetyl Aspartate (NAA), Creatine (Cr), Choline (Cho) and the water resonance whose magnitude, as is well-known, is much larger than the magnitude of the metabolites of interest. The available prior knowledge is related to the Lactate doublet with  $\Delta f$  known and equal to 7Hz. The approximate frequency locations for all peaks of interest are known as well: Lac (-215Hz, 1.3ppm; -208Hz, 1.4ppm), NAA (-169Hz, 2.1ppm), Cr (-104Hz, 3.1ppm) and Cho (-92Hz,

3.3ppm). The choice of the model order  $K$ , which characterizes Eq.(4.1.1), represents an important step since we have to take into account the contribution of the residual water signal: a too small value of  $K$  could result in information loss, while a too large value could incorporate too much noise and generate spurious spectral features. Several criteria, which estimate the model order when unknown, are available in the literature. We chose to apply the minimum description length (MDL) criterion ([50],[53]), which estimates the best model order by minimizing a discrete function of the singular values of the Hankel matrix (4.1.6). We obtained the value  $K = 7$ , which means that the residual water resonance is modeled by two exponentially damped complex sinusoids. In Table 4.5 the parameter estimates obtained when processing the signal by AMARES (after water removal by HSVD) and the four blackbox methods are displayed. Notice that the methods

peak	Method	$f_k(\text{Hz})$	$d_k(\text{Hz})$	$a_k(\text{a.u.})$	$\phi_k(^{\circ})$
1 Lac (-215Hz)	AMARES	$-215.22 \pm 0.08$	$4.97 \pm 0.52$	$13.90 \pm 0.96$	$55.07 \pm 0.07$
	KNOB-TLS	$-214.97 \pm 0.08$	$4.87 \pm 0.52$	$13.62 \pm 0.96$	$65.77 \pm 0.07$
	KNOB-SVD	$-214.97 \pm 0.08$	$5.07 \pm 0.53$	$13.86 \pm 0.96$	$65.57 \pm 0.07$
	HTLSPK	$-215.02 \pm 0.10$	$6.32 \pm 0.63$	$15.31 \pm 1.03$	$63.29 \pm 0.07$
	HTLS	$-215.04 \pm 0.08$	$2.94 \pm 0.52$	$8.71 \pm 1.03$	$57.71 \pm 0.06$
2 Lac (-208Hz)	AMARES	$-208.22 \pm 0.08$	$4.97 \pm 0.52$	$13.90 \pm 0.96$	$55.07 \pm 0.07$
	KNOB-TLS	$-207.97 \pm 0.08$	$4.87 \pm 0.52$	$13.62 \pm 0.96$	$65.77 \pm 0.07$
	KNOB-SVD	$-207.97 \pm 0.08$	$5.07 \pm 0.53$	$13.86 \pm 0.96$	$65.57 \pm 0.07$
	HTLSPK	$-208.02 \pm 0.10$	$6.32 \pm 0.63$	$15.31 \pm 1.03$	$63.29 \pm 0.07$
	HTLS	$-208.07 \pm 0.08$	$6.38 \pm 0.52$	$18.53 \pm 1.03$	$73.59 \pm 0.06$
3 NAA	AMARES	$-168.09 \pm 0.16$	$7.80 \pm 1.01$	$19.40 \pm 1.80$	$-124.93 \pm 0.09$
	KNOB-TLS	$-168.36 \pm 0.16$	$7.75 \pm 1.01$	$19.12 \pm 1.79$	$-137.65 \pm 0.09$
	KNOB-SVD	$-168.36 \pm 0.17$	$7.95 \pm 1.04$	$19.37 \pm 1.81$	$-137.43 \pm 0.09$
	HTLSPK	$-168.34 \pm 0.16$	$7.66 \pm 1.01$	$18.92 \pm 1.78$	$-136.63 \pm 0.09$
	HTLS	$-168.34 \pm 0.16$	$7.58 \pm 0.99$	$18.84 \pm 1.77$	$-137.37 \pm 0.09$
4 Cr	AMARES	$-103.62 \pm 0.19$	$8.91 \pm 1.19$	$21.02 \pm 2.15$	$-124.93 \pm 0.10$
	KNOB-TLS	$-103.13 \pm 0.18$	$8.65 \pm 1.15$	$20.93 \pm 2.13$	$-108.78 \pm 0.10$
	KNOB-SVD	$-103.12 \pm 0.19$	$8.94 \pm 1.19$	$21.32 \pm 2.18$	$-108.66 \pm 0.10$
	HTLSPK	$-103.13 \pm 0.18$	$8.58 \pm 1.15$	$20.75 \pm 2.12$	$-108.57 \pm 0.10$
	HTLS	$-103.13 \pm 0.18$	$8.50 \pm 1.14$	$20.71 \pm 2.11$	$-108.83 \pm 0.10$
5 Cho	AMARES	$-92.00 \pm 0.10$	$9.35 \pm 0.61$	$44.09 \pm 2.20$	$-124.93 \pm 0.05$
	KNOB-TLS	$-92.02 \pm 0.10$	$9.52 \pm 0.61$	$45.79 \pm 2.24$	$-126.79 \pm 0.05$
	KNOB-SVD	$-92.03 \pm 0.10$	$9.58 \pm 0.61$	$45.96 \pm 2.26$	$-127.05 \pm 0.05$
	HTLSPK	$-92.02 \pm 0.10$	$9.49 \pm 0.61$	$45.67 \pm 2.24$	$-126.59 \pm 0.05$
	HTLS	$-92.01 \pm 0.10$	$9.48 \pm 0.60$	$45.69 \pm 2.23$	$-126.62 \pm 0.05$

**Table 4.5.** Parameter estimates and their CRBs for an *in vivo* proton MRS signal measured from the human brain.

KNOB-TLS, KNOB-SVD and HTLSPK provide estimates that are very close to

the AMARES estimates. However, KNOB-TLS and KNOB-SVD are more accurate than HTLSPK. In the present case, also HTLS seems to provide acceptable parameter estimates, but it is important to note that the imposed prior knowledge concerning the Lactate doublet is not satisfied, especially for the damping factor, amplitude and phase estimates. Fig. 4.6 shows the results of the quantification of the proton MRS signal for AMARES and KNOB-TLS. Similar results are obtained when quantifying other *in vivo* proton MRS signals.

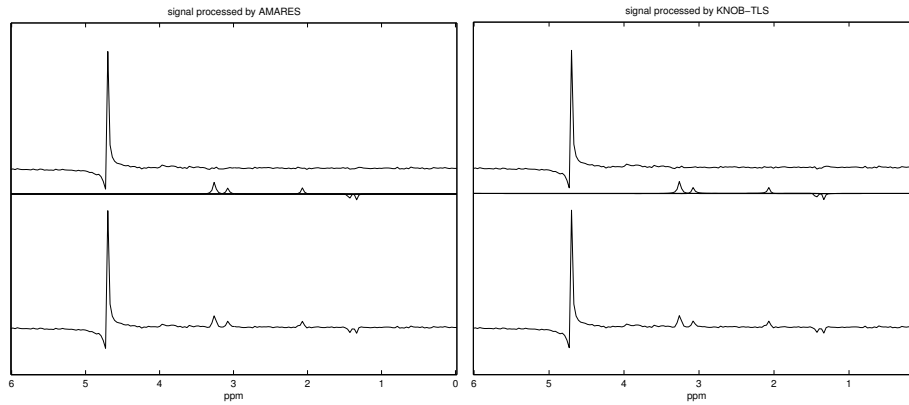


**Figure 4.6.** Bottom: real part of the original proton signal spectrum; middle: real part of the spectra of the individual peaks estimated by AMARES (left) and KNOB-TLS (right); top: real part of the residual signal spectrum after estimation with AMARES (left) and KNOB-TLS (right).

## 4.4 Conclusions

In this chapter a subspace-based parameter estimation method, called KNOB-SVD, and its improved TLS variant KNOB-TLS have been described. They are able to exploit biochemical prior knowledge, which is often available when considering MRS signals and whose use is important for accuracy and resolution. The performance of the proposed methods has been compared, in terms of robustness and accuracy, to that of three well known estimation methods: the interactive method AMARES and the two subspace-based methods HTLS and HTLSPK( $\Delta fd_{eq}$ ). Our extensive simulation and *in vivo* studies show that, in general, the inclusion of prior knowledge in estimation algorithms improves both robustness and accuracy of the parameter estimates. Indeed, the methods KNOB-TLS, KNOB-SVD, HTLSPK( $\Delta fd_{eq}$ ) and AMARES outperform the method HTLS which does not allow the inclusion of any prior knowledge. Moreover, KNOB-TLS is more accurate than KNOB-SVD, and is able to outperform the method HTLSPK( $\Delta fd_{eq}$ ), especially in terms of robustness, and to provide parameter estimates which are comparable to the AMARES ones.

However, it is not able to outperform the interactive method AMARES, which is the most robust and accurate method.

Since AMARES is an optimization-based method that requires good initial parameter estimates to converge properly, the proposed method KNOB-SVD/TLS can be used to provide good starting values to the interactive AMARES method, hence decreasing the need for human interaction.

# **TISSUE SEGMENTATION AND CLASSIFICATION OF MRSI DATA USING CCA**

*In this chapter, a fast and reliable tissue segmentation technique, based on a statistical method called Canonical Correlation Analysis (CCA), is proposed. This method is the multivariate variant of the ordinary correlation analysis and has already been successfully applied to functional Magnetic Resonance Imaging data in order to map sensor, motor and cognitive functions to specific areas in the brain [22]. Here CCA is adapted for MRSI data processing in order to detect possible homogeneous tissue regions, such as tumor regions, characterizing the considered sample. Extensive studies, performed on simulated as well as in vivo prostate MRSI data, were carried out in order to explore the properties of the proposed method. Moreover, the performance of CCA and ordinary correlation analysis were compared. The aforementioned studies are reported here and show that CCA significantly outperforms ordinary correlation analysis in terms of accuracy and robustness.*

*The chapter is organized as follows. Section 5.1 introduces the reader to the area of tissue segmentation techniques. In Section 5.2 the basic definition of CCA is introduced and three possible implementations are outlined. In Section 5.3 the application of CCA to MRSI data is described. In Section 5.4 the set up for the simulation studies is defined and the results are reported and discussed. In Section 5.5 the acquisition environment of the in vivo studies is defined and the results are described. Finally, in Section 5.6 the main conclusions are formulated.*

## 5.1 Tissue segmentation of MRSI data

As already shown in the previous chapters, MRSI is a powerful non-invasive diagnostic tool since it provides significant biochemical information on the molecules of the organism under investigation. MRSI data can also be exploited in tissue segmentation techniques, which play a crucial role in many biomedical applications such as the quantification of tissue volumes, localization of possible pathologies, improvement of pre-surgical diagnosis and optimization of the surgical approach, therapy planning, etc. A variety of methods are available in the literature. They are often used in combination in order to solve different segmentation problems.

They can be divided into several categories: thresholding techniques [51]; region growing techniques [39]; clustering techniques [14]; Markov random field models [30]; classifiers [4]; artificial neural networks [49]; etc. In this thesis, a fast and reliable tissue segmentation technique, based on a statistical method called Canonical Correlation Analysis (CCA), is proposed. This method is the multivariate variant of the ordinary correlation analysis and has already been successfully applied to functional Magnetic Resonance Imaging data in order to map sensor, motor and cognitive functions to specific areas in the brain [22]. Here CCA is adapted for MRSI data processing in order to detect possible homogeneous tissue regions, such as tumor regions, characterizing the considered sample. The goal is achieved by combining the spectral-spatial information provided by the MRSI data set and a signal subspace that models the spectrum of a characteristic tissue type, which may be present in the organ under investigation and, therefore, needs to be detected. More precisely, CCA quantifies the relationship between two sets of variables, mag-

nitude spectra of the measured data and signal subspace, by means of correlation coefficients. These coefficients are then exploited in order to construct nosologic images [62] in which all the detected tissues are visualized. Such images can be easily interpreted by radiologists and physicians and, along with clinical and radiological information, can improve the accuracy of the diagnosis.

## 5.2 Canonical Correlation Analysis

CCA is a statistical technique developed by Hotelling in 1936 in order to assess the relationship between two sets of variables [31]. It is a multichannel generalization of ordinary correlation analysis, which quantifies the relationship between two random variables  $x$  and  $y$  by means of the so-called correlation coefficient

$$\rho = \frac{Cov[x, y]}{\sqrt{V[x] V[y]}}, \quad (5.2.1)$$

where  $Cov$  and  $V$  stand for covariance and variance, respectively. The correlation coefficient is a scalar with value between -1 and 1 that measures the degree of linear dependence between  $x$  and  $y$ . For zero-mean variables Eq.(5.2.1) is replaced by

$$\rho = \frac{E[xy]}{\sqrt{E[x^2] E[y^2]}}. \quad (5.2.2)$$

where  $E$  stands for expected value. Canonical correlation analysis can be applied to multichannel signal processing as follows: consider two zero-mean multivariate random vectors  $\mathbf{x} = [x_1(t), \dots, x_m(t)]^T$  and  $\mathbf{y} = [y_1(t), \dots, y_n(t)]^T$ , with  $t = 1, \dots, N$ , where the superscript  $T$  denotes the transpose. The following linear combinations of the components in  $\mathbf{x}$  and  $\mathbf{y}$  are defined, which respectively represent two new scalar random variables  $X$  and  $Y$

$$X = \omega_{x_1}x_1 + \dots + \omega_{x_m}x_m = \omega_x^T \mathbf{x}, \quad (5.2.3)$$

$$Y = \omega_{y_1}y_1 + \dots + \omega_{y_n}y_n = \omega_y^T \mathbf{y}. \quad (5.2.4)$$

CCA computes the linear combination coefficients  $\omega_x = [\omega_{x_1}, \dots, \omega_{x_m}]^T$  and  $\omega_y = [\omega_{y_1}, \dots, \omega_{y_n}]^T$ , called regression weights, so that the correlation between the new variables  $X$  and  $Y$  is maximum. The solution  $\omega_x = \omega_y = \mathbf{0}$  is not allowed and the new variables  $X$  and  $Y$  are called canonical variates. The regression weights are found by solving the maximization problem obtained by substituting Eqs.(5.2.3) into Eq.(5.2.2), i.e.

$$\max_{\omega_x, \omega_y} \rho(\omega_x, \omega_y) = \frac{\omega_x^T \mathbf{C}_{xy} \omega_y}{\sqrt{(\omega_x^T \mathbf{C}_{xx} \omega_x)(\omega_y^T \mathbf{C}_{yy} \omega_y)}}, \quad (5.2.5)$$

where  $\mathbf{C}_{xx}$  and  $\mathbf{C}_{yy}$  are the within-set covariance matrices of  $\mathbf{x}$  and  $\mathbf{y}$ , respectively, and  $\mathbf{C}_{xy}$  is the between-sets covariance matrix. In practice, estimated covariance matrices are used

$$\hat{\mathbf{C}}_{xx} = \frac{1}{N} \sum_{t=1}^N x(t)x(t)^T, \quad (5.2.6)$$

$$\hat{\mathbf{C}}_{yy} = \frac{1}{N} \sum_{t=1}^N y(t)y(t)^T, \quad (5.2.7)$$

$$\hat{\mathbf{C}}_{xy} = \frac{1}{N} \sum_{t=1}^N x(t)y(t)^T. \quad (5.2.8)$$

The maximization problem is solved by setting the derivatives of Eq.(5.2.5), with respect to  $\omega_x$  and  $\omega_y$ , equal to zero, resulting in the following system of equations

$$\begin{cases} \hat{\mathbf{C}}_{xy}\hat{\omega}_y = \rho\lambda_x\hat{\mathbf{C}}_{xx}\hat{\omega}_x \\ \hat{\mathbf{C}}_{yx}\hat{\omega}_x = \rho\lambda_y\hat{\mathbf{C}}_{yy}\hat{\omega}_y, \end{cases} \quad (5.2.9)$$

where  $\lambda_x = \lambda_y^{-1} = \sqrt{(\hat{\omega}_y^T \hat{\mathbf{C}}_{yy} \hat{\omega}_y) / (\hat{\omega}_x^T \hat{\mathbf{C}}_{xx} \hat{\omega}_x)}$  are scaling factors. By combining the two equations in Eq.(5.2.9), the following eigenvalue problems are obtained

$$\begin{cases} \hat{\mathbf{C}}_{xx}^{-1} \hat{\mathbf{C}}_{xy} \hat{\mathbf{C}}_{yy}^{-1} \hat{\mathbf{C}}_{yx} \hat{\omega}_x = \rho^2 \hat{\omega}_x \\ \hat{\mathbf{C}}_{yy}^{-1} \hat{\mathbf{C}}_{yx} \hat{\mathbf{C}}_{xx}^{-1} \hat{\mathbf{C}}_{xy} \hat{\omega}_y = \rho^2 \hat{\omega}_y, \end{cases} \quad (5.2.10)$$

whose common eigenvalues  $\rho^2$  represent the squared canonical coefficients between  $\mathbf{x}$  and  $\mathbf{y}$ . The first pair of canonical variates correspond to the eigenvectors  $\hat{\omega}_x$  and  $\hat{\omega}_y$  associated with the largest eigenvalue. The remaining canonical variates correspond to the remaining eigenvectors and the associated eigenvalues are the squared canonical coefficients. It can be shown that the canonical variates are maximally correlated and, at the same time, uncorrelated with the previous pairs. As can be observed in Eq.(5.2.10), matrix inversions need to be performed. These operations could lead to numerical instability if  $\hat{\mathbf{C}}_{xx}$  and  $\hat{\mathbf{C}}_{yy}$  are almost rank deficient. Two more reliable algorithms are described in [28] and [74]. The first algorithm computes the canonical coefficients and the corresponding regression weights by solving a generalized symmetric eigenvalue problem. The second algorithm is based on the computation of the principal angles. In fact, canonical correlation analysis is the statistical interpretation of the geometric concept of principal angles between linear subspaces and associated principal directions [31]. Here, an outline for both algorithms is provided.

### 5.2.1 Algorithm CCA–GEP: CCA by solving a Generalized Eigenvalue Problem (GEP)

Given the zero-mean multivariate random vectors  $\mathbf{x} = [x_1(t), \dots, x_m(t)]$  and  $\mathbf{y} = [y_1(t), \dots, y_n(t)]$ , with  $t = 1, \dots, N$ ,

- **Step 1 :**

Compute the estimated covariance matrices  $\hat{\mathbf{C}}_{xx}$ ,  $\hat{\mathbf{C}}_{yy}$  and  $\hat{\mathbf{C}}_{xy}$ .

- **Step 2 :**

Solve the following generalized symmetric eigenvalue problem

$$\begin{bmatrix} \mathbf{0} & \hat{\mathbf{C}}_{xy} \\ \hat{\mathbf{C}}_{xy}^T & \mathbf{0} \end{bmatrix} \begin{bmatrix} \hat{\omega}_x \\ \hat{\omega}_y \end{bmatrix} = \begin{bmatrix} \hat{\mathbf{C}}_{xx} & \mathbf{0} \\ \mathbf{0} & \hat{\mathbf{C}}_{yy} \end{bmatrix} \begin{bmatrix} \hat{\omega}_x \\ \hat{\omega}_y \end{bmatrix} \rho, \quad (5.2.11)$$

subject to  $\hat{\omega}_x^T \hat{\mathbf{C}}_{xx} \hat{\omega}_x = 1$  and  $\hat{\omega}_y^T \hat{\mathbf{C}}_{yy} \hat{\omega}_y = 1$ .

- **Step 3 :**

Set the canonical coefficients equal to the eigenvalues  $\rho$ , and the regression weights equal to the corresponding eigenvectors  $\hat{\omega}_x$  and  $\hat{\omega}_y$ .

### 5.2.2 Algorithm CCA-PA: CCA by computing Principal Angles (PA)

Given the zero-mean multivariate random vectors  $\mathbf{x} = [x_1(t), \dots, x_m(t)]$  and  $\mathbf{y} = [y_1(t), \dots, y_n(t)]$ , with  $t = 1, \dots, N$ ,

- **Step 1 :**

Consider the matrices  $\tilde{\mathbf{X}}$  and  $\tilde{\mathbf{Y}}$ , defined as follows

$$\tilde{\mathbf{X}} = \begin{bmatrix} x_1(1) & \cdots & x_m(1) \\ \vdots & & \vdots \\ x_1(N) & \cdots & x_m(N) \end{bmatrix}, \quad \tilde{\mathbf{Y}} = \begin{bmatrix} y_1(1) & \cdots & y_n(1) \\ \vdots & & \vdots \\ y_1(N) & \cdots & y_n(N) \end{bmatrix} \quad (5.2.12)$$

- **Step 2 :**

Compute the QR decompositions of  $\tilde{\mathbf{X}}$  and  $\tilde{\mathbf{Y}}$

$$\begin{cases} \tilde{\mathbf{X}} = \mathbf{Q}_{\tilde{\mathbf{X}}} \mathbf{R}_{\tilde{\mathbf{X}}} \\ \tilde{\mathbf{Y}} = \mathbf{Q}_{\tilde{\mathbf{Y}}} \mathbf{R}_{\tilde{\mathbf{Y}}}, \end{cases} \quad (5.2.13)$$

where  $\mathbf{Q}_{\tilde{\mathbf{X}}}$  and  $\mathbf{Q}_{\tilde{\mathbf{Y}}}$  are orthogonal matrices and  $\mathbf{R}_{\tilde{\mathbf{X}}}$  and  $\mathbf{R}_{\tilde{\mathbf{Y}}}$  are upper triangular matrices.

- **Step 3 :**

Compute the SVD of  $\mathbf{Q}_{\tilde{\mathbf{X}}}^T \mathbf{Q}_{\tilde{\mathbf{Y}}}$

$$\mathbf{Q}_{\tilde{\mathbf{X}}}^T \mathbf{Q}_{\tilde{\mathbf{Y}}} = \mathbf{U} \mathbf{S} \mathbf{V}^T, \quad (5.2.14)$$

where  $\mathbf{S}$  is a diagonal matrix and  $\mathbf{U}$  and  $\mathbf{V}$  are orthogonal matrices. The cosines of the principal angles are given by the diagonal elements of  $\mathbf{S}$ .

- **Step 4 :**

Set the canonical coefficients equal to the diagonal elements of the matrix  $\mathbf{S}$  and compute the corresponding regression weights as  $\omega_{\tilde{\mathbf{X}}} = \mathbf{R}_{\tilde{\mathbf{X}}}^{-1} \mathbf{U}$  and  $\omega_{\tilde{\mathbf{Y}}} = \mathbf{R}_{\tilde{\mathbf{Y}}}^{-1} \mathbf{V}$ .

The computation of the principal angles yields the most robust implementation of CCA, since it is able to provide reliable results even when the matrices  $\tilde{\mathbf{X}}$  and  $\tilde{\mathbf{Y}}$  are singular. A comparison of the two implementations in terms of computational efficiency is reported in Section 5.3.1.

### 5.3 CCA applied to MRSI data

During the MRSI data acquisition procedure, a number of image slices is acquired. Each image can be partitioned into a certain number of volume elements, called voxels, each characterized by a time-domain signal of length  $N$ . In the proposed tissue segmentation approach, the aim is to detect those voxels whose spectra correlate best with model tissue spectra, which are defined a priori. When applying correlation analysis to MRSI data, the variables  $\mathbf{x}$  and  $\mathbf{y}$  need to be specified. In ordinary correlation analysis  $\mathbf{x}$  and  $\mathbf{y}$  are univariate variables and, specifically, the  $\mathbf{x}$  variable consists of the magnitude spectrum of the measured signal contained in each voxel, while the  $\mathbf{y}$  variable consists of the model tissue magnitude spectrum. The correlation coefficient between  $\mathbf{x}$  and  $\mathbf{y}$  is computed and assigned to the voxel under investigation. Once each voxel has been processed, a new grid of voxels, of the same size of the original image, is obtained, which contains correlation coefficients instead of MRSI signals. This new grid is called correlation map.

The difference between ordinary correlation analysis and CCA mainly consists in a different choice of the variables  $\mathbf{x}$  and  $\mathbf{y}$ . In fact, in order to compute the correlation maps, it is possible to exploit the spatial information characterizing the MRSI data set by considering, as variable  $\mathbf{x}$ , a multivariate vector with components representing the magnitude spectrum characterizing the considered voxel as well as the magnitude spectra contained in the neighbor voxels. Several spatial models can be adopted for choosing the neighbor voxels, typical examples of which are described in [22]. The variable  $\mathbf{y}$  also consists of a multivariate vector. Its components represent the basis functions of a signal subspace, that models the characteristic tissue

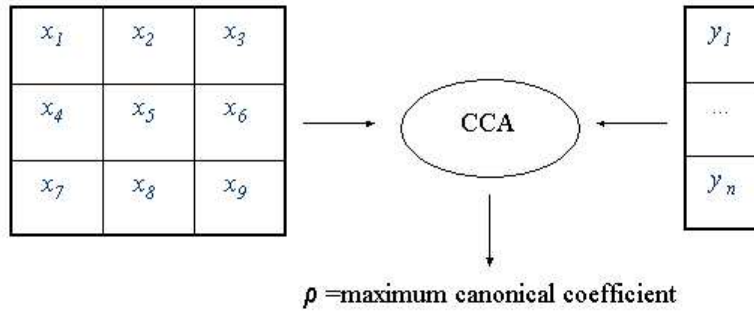


**Figure 5.1.** CCA applied to a  $3 \times 3$  region of voxels in the MRS image and a set of  $n$  spectral basis functions.

magnitude spectrum we are looking for and its possible variations (in amplitudes, frequency shifts and damping factors) that normally affect realistic MRSI data. Several approaches can be adopted in order to model a proper signal subspace; an exhaustive overview is given in [22]. Once the  $\mathbf{x}$  and  $\mathbf{y}$  variables have been defined, CCA is applied voxel by voxel and the largest canonical coefficient is assigned to the voxel under investigation, so that a correlation map is obtained as in the ordinary correlation analysis case. Figure 5.1 schematically shows the CCA approach when processing a  $3 \times 3$  voxel region containing the magnitude spectrum along with its neighbor magnitude spectra. In this particular spatial model, called the “ $3 \times 3$  model”, the variable  $\mathbf{x}$  contains nine components, namely  $\mathbf{x} = [\mathbf{x}_1, \dots, \mathbf{x}_9]$ .

### 5.3.1 Choice of the spatial model

As already mentioned in the previous section, several spatial models can be chosen when applying CCA. As a particular case, the ordinary correlation analysis can be considered as a single-voxel model. The performance of the following spatial models was investigated:

- the single-voxel model
- the  $3 \times 3$  model (Figure 5.1):  
 $\mathbf{x} = [\mathbf{x}_1, \dots, \mathbf{x}_9]$
- the  $3 \times 3$  model without corner voxels:  
 $\mathbf{x} = [\mathbf{x}_2, \mathbf{x}_4, \mathbf{x}_5, \mathbf{x}_6, \mathbf{x}_8]^T$
- the symmetric  $3 \times 3$  model:  
 $\mathbf{x} = [\mathbf{x}_5, (\mathbf{x}_1 + \mathbf{x}_9)/2, (\mathbf{x}_2 + \mathbf{x}_8)/2, (\mathbf{x}_3 + \mathbf{x}_7)/2, (\mathbf{x}_4 + \mathbf{x}_6)/2]^T$
- the symmetric  $3 \times 3$  model without corner voxels:  
 $\mathbf{x} = [\mathbf{x}_5, (\mathbf{x}_2 + \mathbf{x}_8)/2, (\mathbf{x}_4 + \mathbf{x}_6)/2]^T$

The obtained results are described in Section 5.4.

### 5.3.2 Choice of the subspace model

Concerning the choice of the  $\mathbf{y}$  variable, two different approaches were considered in order to define the proper signal subspace able to model the characteristic tissue spectra and their possible variations. Specifically, the Taylor model and the Principal Component Analysis model (PCA) were considered and compared. In order to define the first component of the variable  $\mathbf{y}$ , two thousand signals, characterized by realistic variations of the noiseless simulated signal parameters, were generated. The first component of the  $\mathbf{y}$  variable was then defined as the mean of the magnitude spectra of the generated signals for both approaches. In the Taylor approach, the second component of  $\mathbf{y}$  was obtained as the first-order derivative of the first component, approximated by first-order finite differences. The first principal component of the matrix containing the mean-centered magnitude spectra of the signals, was chosen as second component for the PCA model. For the sake of clarity, the procedure to compute the aforementioned subspace models is here outlined.

#### The Taylor subspace model

- **Step 1 :**

Compute the simulated noiseless signal corresponding to the considered tissue type (with parameters reported in Table 5.1) and its magnitude spectrum  $S(\omega_n)$ , where  $\omega_n$  represents the frequency and  $n = 1, \dots, N$ .

- **Step 2 :**

Produce a large number  $M$  of signals by introducing realistic variations on the noiseless signal parameters of the chosen tissue type.

- **Step 3 :**

Compute the magnitude spectra  $S_i(\omega_n)$ ,  $i = 1, \dots, M$ , of the  $M$  signals produced in the previous step.

- **Step 4 :**

Set the components of the variable  $\mathbf{y}$  as:

$$\begin{cases} y_1(n) = \frac{1}{M} \sum_{i=1}^M S_i(\omega_n) \\ y_2(n) = \frac{S(\omega_{n+1}) - S(\omega_n)}{\Delta\omega} \end{cases} \quad (5.3.15)$$

where  $\Delta\omega$  is the sampling frequency.

### The PCA subspace model

- **Step 1 :**

Compute the simulated noiseless signal corresponding to the considered tissue type (with parameters reported in Table 5.1) and its magnitude spectrum  $S(\omega_n)$ , where  $\omega_n$  represents the frequency and  $n = 1, \dots, N$ .

- **Step 2 :**

Produce a large number  $M$  of signals by introducing realistic variations on the noiseless signal parameters of the chosen tissue type.

- **Step 3 :**

Compute the magnitude spectra  $S_i(\omega_n)$ ,  $i = 1, \dots, M$ , of the  $M$  signals produced in the previous step and arrange them as rows into a matrix  $\mathbf{D}$ .

- **Step 4 :**

Perform Principal Component Analysis on the matrix  $\mathbf{D}$  and denote the first Principal Component as 1<sup>st</sup> PC.

- **Step 5 :**

Set the components of the variable  $\mathbf{y}$  as:

$$\begin{cases} y_1(n) = \frac{1}{M} \sum_{i=1}^M S_i(\omega_n) \\ y_2(n) = 1^{\text{st}} \text{PC} \end{cases} \quad (5.3.16)$$

For the single voxel approach, only one component was considered and set equal to the first component of the Taylor and PCA subspace models, namely  $\mathbf{y} = \mathbf{y}_1$ .

## 5.4 Simulation studies

Figure 5.2 shows the magnitude spectra of four different simulated signals, derived from in vivo data measured in the human prostate, representing, from top to bottom, very aggressive tumor tissue, moderately aggressive tumor tissue, mixed tumor tissue, and healthy peripheral zone tissue.

As can be observed in the above mentioned figure, the spectra are characterized by the presence of three metabolite peaks: Choline, Creatine and Citrate doublet. In particular, aggressive tumor tissue is characterized by a strong contribution of Choline, while healthy tissue exhibits a higher contribution of Citrate. In general, prostate tumor regions are characterized by higher levels of Choline and reduced levels of Citrate. The spectra represent the Discrete Fourier Transform of four

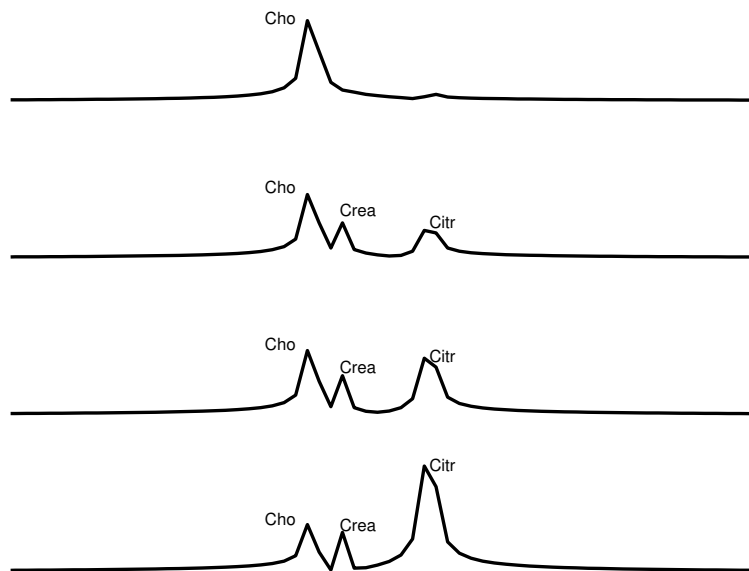


**Figure 5.2.** Magnitude spectra of characteristic prostate signals. From top to bottom: aggressive tumor tissue spectrum; moderately aggressive tumor tissue spectrum; mixed tumor tissue spectrum; healthy tissue spectrum. The spectra contain the following compounds: Choline (Cho), Creatine (Crea), Citrate doublet (Citr).

signals consisting of 256 complex data points ( $N = 256$ ) modelled as the sum of  $K = 4$  exponentially damped complex sinusoids, as in Eq.(2.2.1)

$$y_n = \sum_{k=1}^K a_k e^{j\phi_k} e^{(-d_k + j2\pi f_k)n\Delta t} + e_n, \quad n = 0, \dots, N - 1. \quad (5.4.17)$$

The parameter values of the noiseless simulated signals are reported in Table 5.1.

Parameters	Choline	Creatine	Citrate1	Citrate2
Frequency	-49.3Hz	-38.9Hz	-12.1Hz	-9.6Hz
Damping	2Hz	2Hz	2Hz	2Hz
Phase	0°	0°	0°	0°
Amplitude aggressive tumor	4.3e6a.u.	0.2e6a.u.	0.2e6a.u.	0.2e6a.u.
Amplitude tumor	3.3e6a.u.	1.6e6a.u.	1.2e6a.u.	1.2e6a.u.
Amplitude mixed tissue	3.3e6a.u.	1.8e6a.u.	2.4e6a.u.	2.4e6a.u.
Amplitude healthy tissue	2.3e6a.u.	1.8e6a.u.	4.4e6a.u.	4.4e6a.u.

**Table 5.1.** Parameter values of the noiseless simulated prostate signals.

The dampings and frequencies were selected based on in vivo prostate data acquired at 1.5T. The Citrate was modeled as a doublet with frequency split equal to 2.5Hz. The amplitude values are expressed in arbitrary units (a.u.).

A simulated MRSI data set was produced, consisting of a 14x14 grid of voxels, in which four different and well localized regions of tissue spectra were inserted. The grid is shown in Figure 5.3 and the tissue regions are indicated by different colors: black for aggressive tumor tissue, dark gray for tumor tissue, gray for mixed tissue and light gray for healthy tissue.

Figure 5.4 shows the magnitude spectra contained in the previous grid. In order to simulate a realistic MRSI data set, variations were introduced on the signal parameters displayed in Table 5.1. More precisely, spectra for each type of tissue were generated, randomly characterized by variations up to 20% for amplitudes, up to forty times the given value for the damping factors, up to a shift of 1.25Hz for the frequencies. The magnitude spectra of the simulated signals were perturbed by adding Gaussian noise with standard deviation  $\sigma$ . Figure 5.5 shows the magnitude spectra of the same signals displayed in Figure 5.4 perturbed by Gaussian noise with  $\sigma = 80 \times 10^6$ . Ordinary correlation analysis and CCA were then applied in order to detect the four tissue regions.

#### 5.4.1 Simulation results

In the simulation studies, 300 simulation runs were performed for different noise standard deviation values. Before applying the proposed tissue segmentation method, four different  $\mathbf{y}$  variables were defined, one for each prostate tissue type. CCA was

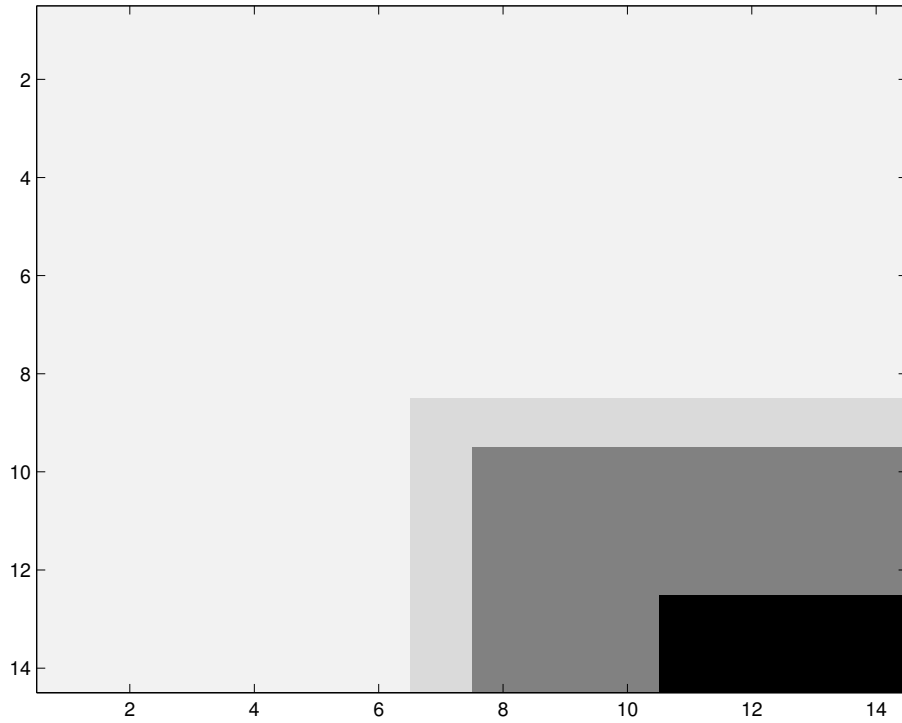


**Figure 5.3.** Original tissue grid. Black region: aggressive tumor voxels; dark gray region: moderately aggressive tumor voxels; gray region: mixed tissue voxels; light gray region: healthy tissue voxels.

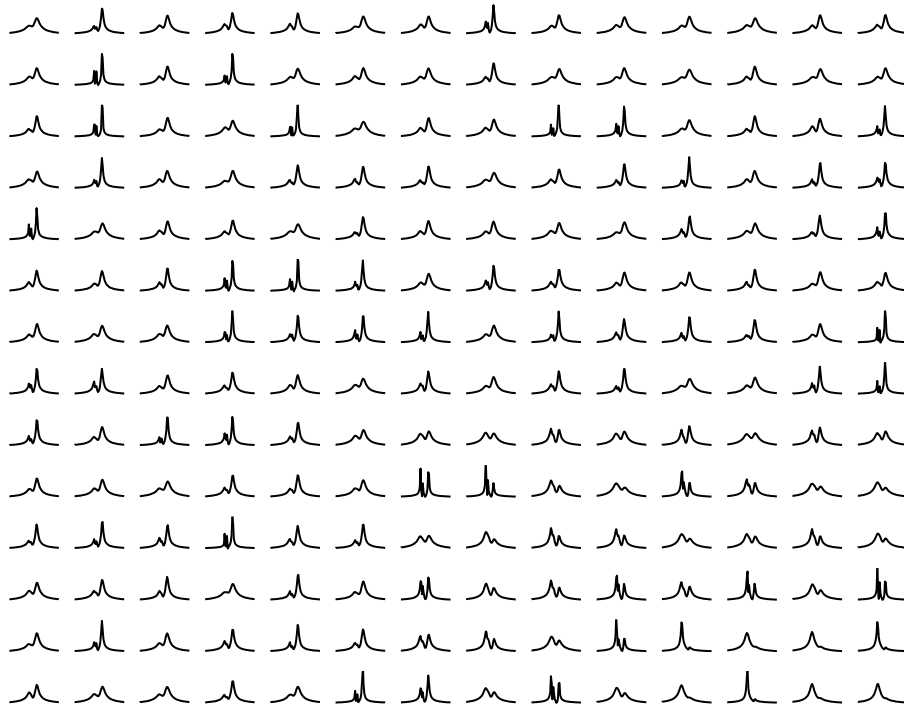


**Figure 5.4.** Magnitude spectra of the noiseless simulated MRSI data.

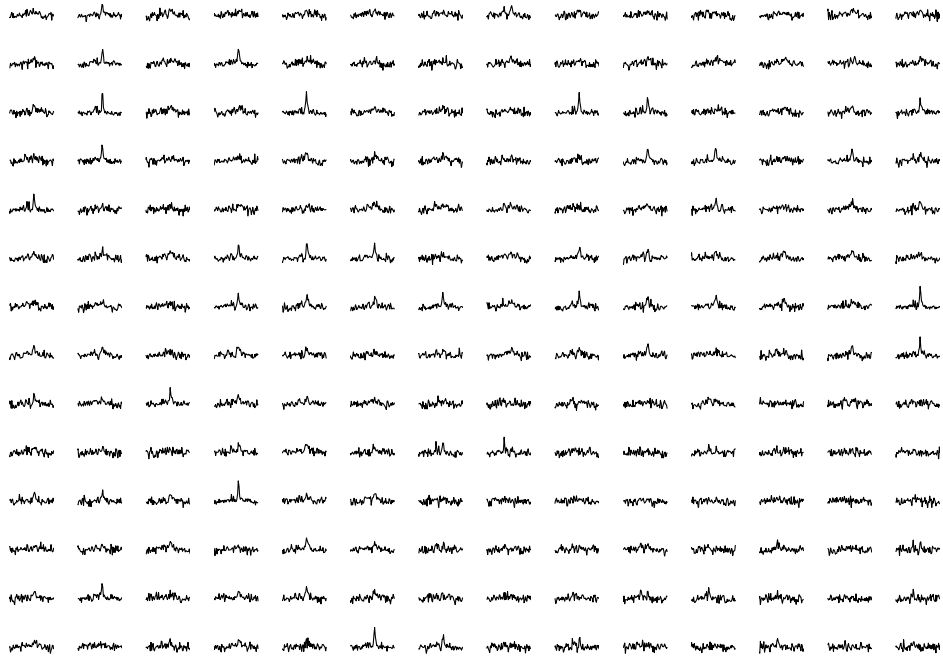


**Figure 5.5.** Magnitude spectra of the noisy simulated MRSI data when considering a high noise level, with standard deviation equal to  $80 \times 10^6$ .

then applied between the noisy data set and the above mentioned  $\mathbf{y}$  variables, and four correlation maps were obtained. The nosologic image, as defined in [62], consisting of one single image in which all the detected tissue types are visualized, was obtained by comparing, voxel by voxel, the four canonical coefficients characterizing the different correlation maps. The considered voxel was then assigned to the tissue with largest canonical coefficient and labelled by the corresponding tissue color.

In order to compare the performance of CCA when applying different spatial models and/or different subspace models, the correlation coefficients between the original and the detected tissue regions were estimated for each simulation run. Figure 5.6 shows the mean value of these correlation coefficients, over the total number of simulation runs and for each noise level, when considering the PCA subspace model. Different spatial models were applied, namely the single voxel approach (sv), the symmetric  $3 \times 3$  model (sym $3 \times 3$ ), the  $3 \times 3$  model ( $3 \times 3$ ), the  $3 \times 3$  model without corner voxels ( $3 \times 3$ wcv), and the symmetric  $3 \times 3$  model without corner voxels (sym $3 \times 3$ wcv).

As can be observed in the figure, the best performance is obtained for the symmetric  $3 \times 3$  model, while the single voxel model is least accurate, especially for high noise levels. In general, the performance of all models is sensitive to the number of voxels characterizing the original tissue region as well as to the shape of the spectra. In fact, the quality of the performance for the mixed tissue region is much poorer with respect to the performance shown for the other tissue regions, since little spatial information can be exploited and since the level of the different metabolites in the spectra is not as discriminating as in the other tissue spectra.

In Figure 5.7 (left) the mean value of the computation time (in seconds), as a function of the noise standard deviation and over the total number of simulation runs, is displayed.

The single voxel model is the most efficient, but the other models can be considered efficient as well since they need less than 1 second for processing the whole simulated MRSI data set.

Extensive studies were also carried out in order to compare the performance of the PCA and Taylor subspace models. The two approaches showed a similar behavior in terms of accuracy as well as in terms of computational efficiency, since they exploit the same number of components in the variable  $\mathbf{x}$  and  $\mathbf{y}$ .

Figure 5.7 (right) shows the computation time versus the noise standard deviation, over the total number of simulation runs, of the CCA implementations based on solving a symmetric generalized eigenvalue problem (CCA-GEP, Eq.(5.2.11)) and on computing principal angles (CCA-PA, Eq.(5.2.14)), respectively. As can be observed in the figure, the latter implementation is faster and, as already described in Section 5.2, is the most robust since it is able to provide the canonical coefficients even when the  $\mathbf{x}$  and  $\mathbf{y}$  variables are almost rank deficient or singular matrices. In particular, such a situation occurs when applying the multi-voxel approach to the edge voxels of the MRSI grid. In fact, two rows and two columns of dummy voxels need to be introduced. Practically, the additional rows and columns of dummy voxels are simply obtained by producing a copy of the first (last) row of voxels

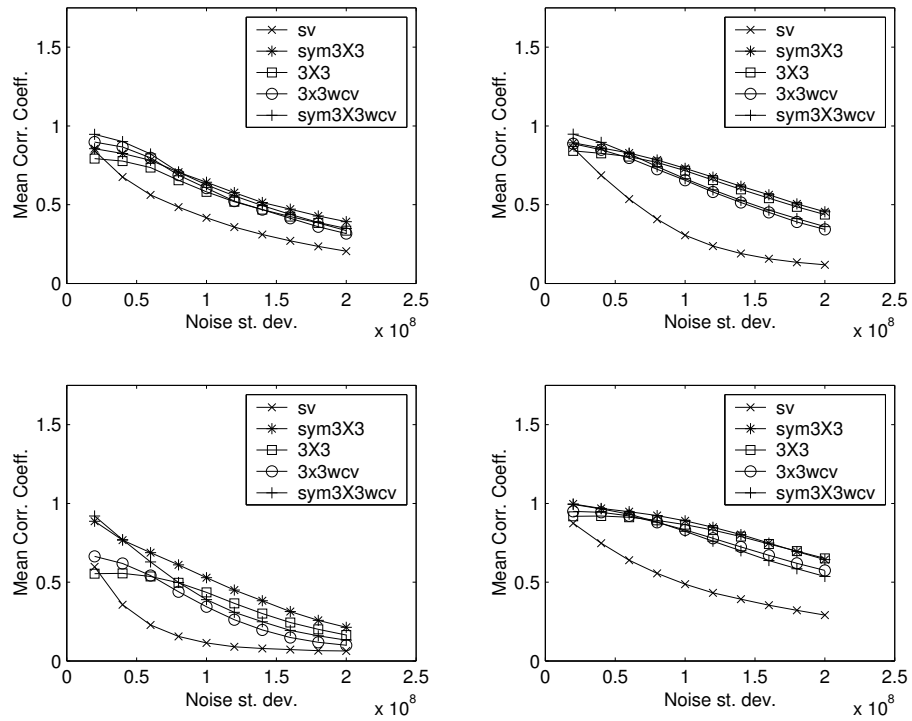


**Figure 5.6.** Mean of the correlation coefficients, over 300 simulation runs, between the detected regions and the original tissue regions as a function of the standard deviation, when considering different spatial models. Subspace model: PCA. Top: aggressive tumor (left), moderately aggressive tumor (right). Bottom: mixed tissue (left), healthy tissue (right).

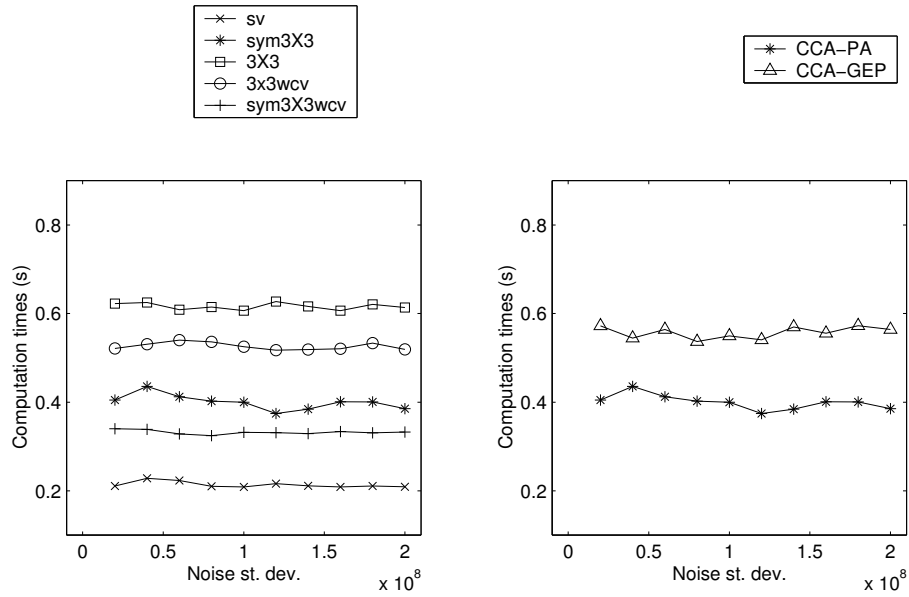


**Figure 5.7.** Mean of the computation times (in seconds), over 300 simulation runs and as a function of the standard deviation. Left: the PCA subspace model and different spatial models are applied. Right: the CCA implementations based on the computation of the principal angles (CCA-PA) and on solving a generalized eigenvalue problem (CCA-GEP) are applied. Spatial model: symmetric 3x3. Subspace model: PCA.

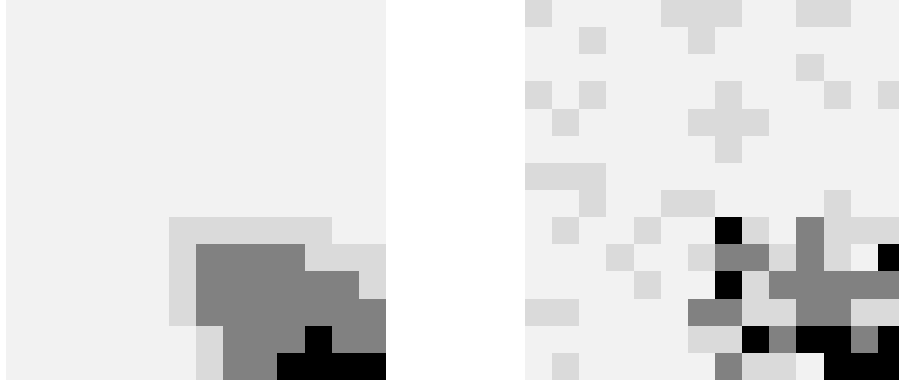


**Figure 5.8.** Nosologic images obtained by the symmetric  $3 \times 3$  multi-voxel model (left) and the single voxel model (right), for a noise standard deviation equal to  $80 \times 10^6$ . Subspace model: PCA. Black region: aggressive tumor voxels; dark gray region: moderately aggressive tumor voxels; gray region: mixed tissue voxels; light gray: healthy tissue voxels.

of the original grid at the top (bottom), and a copy of the first (last) column of voxels at the left (right) hand-side of the given grid. In the example under investigation, the resulting grid has dimensions  $16 \times 16$  instead of  $14 \times 14$ . The dummy voxels allow the application of any multi-voxel spatial model, but the  $\mathbf{x}$  vector will now contain some components that are equal to each other (as for the  $3 \times 3$  model and  $3 \times 3$  model without corner voxels) or linearly dependent (symmetric  $3 \times 3$  model), thereby resulting in a singular matrix. The CCA implementation based on Eq.(5.2.10) is not able to provide a solution, since the computation of the inverse of the matrix  $\mathbf{C}_{xx}$  is not possible. The implementation CCA-GEP based on solving the symmetric generalized eigenvalue problem (Eq.(geneigpr)) is able to provide a solution, but it may not be accurate since the matrix  $\mathbf{C}_{xx}$  has a large condition number. Such problems are overcome by the implementation CCA-PA based on computing principal angles, which then yields the most robust results. As final result, in Figure 5.8, the nosologic images obtained by the symmetric  $3 \times 3$  model (left) and the single voxel model (right), when considering a high noise level, with standard deviation equal to  $80 \times 10^6$ , are shown. The PCA subspace model was used. The images clearly show that the multi-voxel approach significantly outperforms the ordinary correlation analysis approach. In fact, the tissue regions detected by CCA are well localized, despite their irregular edges. On the other hand, the single voxel approach detects the presence of aggressive tumor and mixed tissue voxels in parts of the grid where other types of tissue spectra were originally inserted.

## 5.5 *In vivo* studies

CCA and ordinary correlation analysis were applied to *in vivo* prostate MRSI data. The data were acquired in the Radiology Department of the K.U.Leuven University Hospital, as part of the routine clinical preoperative MR imaging and spectroscopy protocol for the prostate. They were acquired at 63.6 MHz on a 1.5T Siemens Sonata scanner, using a 3D PRESS CSI sequence (TR = 600 ms, TE = 100 ms). The FOV was adapted to the PRESS box surrounding the prostate that was positioned such as to suppress unwanted fat signals around the prostate. The CSI FOV and matrix size were set to obtain isotropic voxels at acquisition (typ.  $6\text{mm} \times 6\text{mm} \times 6\text{mm}$ ). The data were reconstructed to a  $16 \times 16 \times 16$  3D matrix. Each CSI voxel signal consists of 512 complex data points in the time domain and the sampling time is 0.8 ms. The acquisition averages responded to a weighted k-space sampling scheme so as to obtain a substantial gain in S/N within a short time, without affecting dramatically the spatial resolution. The total 3D volume was acquired in about 11 min. The coil was an intrarectal coil for maximal S/N in both images and spectra. All patients signed an informed consent paper, in agreement with the guidelines of the University Hospital Ethical Committee.

### 5.5.1 *In vivo* results

Figure 5.9 shows a screenshot, provided by the Siemens scanner, in which the spectral map characterizing the  $10 \times 10$  PRESS box region, as processed by the spectroscopy package of the Siemens scanner (Syngo MR 2004), is displayed.

The saturation blocks used to suppress unwanted fat signals around the prostate are displayed as well. In the prostate image, the suspicious zone is the dark region in the right bottom part. The screenshot also shows the spectrum of the MRS signal characterizing voxel number 88 (in the PRESS box region the voxels are numbered from the upper left corner to the lower right corner). The spectrum clearly shows a high level of Choline and a low contribution of Citrate. On the basis of the spectroscopy, the following voxels in the neighborhood can be labelled as tumor voxels: 78, 87, 89, 97, 98, 99. The signals characterizing the MRSI data set contain the following compounds: lipids (between 1 ppm and 2 ppm), Citrate doublet (2.6 ppm), Creatine (3 ppm), Choline (3.2 ppm), water resonance (4.7 ppm). In order to improve the performance of the proposed tissue segmentation procedure, the signals were preprocessed by filtering out the water and lipid components. The water and lipid removal was performed by means of HLSVD-PRO [35]. CCA was then applied to the grid of filtered signals, in order to retrieve the possible tissue types characterizing the sample under investigation. As for the simulation studies, the spatial model as well as the subspace model had to be defined. As far as the spatial model, i.e. the variable, is concerned, the best performance was obtained by applying the symmetric  $3 \times 3$  model. For the subspace model, i.e. the  $\mathbf{y}$  variable, the Taylor approach was adopted. The first component of  $\mathbf{y}$  was defined as the average of 2000 spectra containing the following variations of the noiseless simulated signal

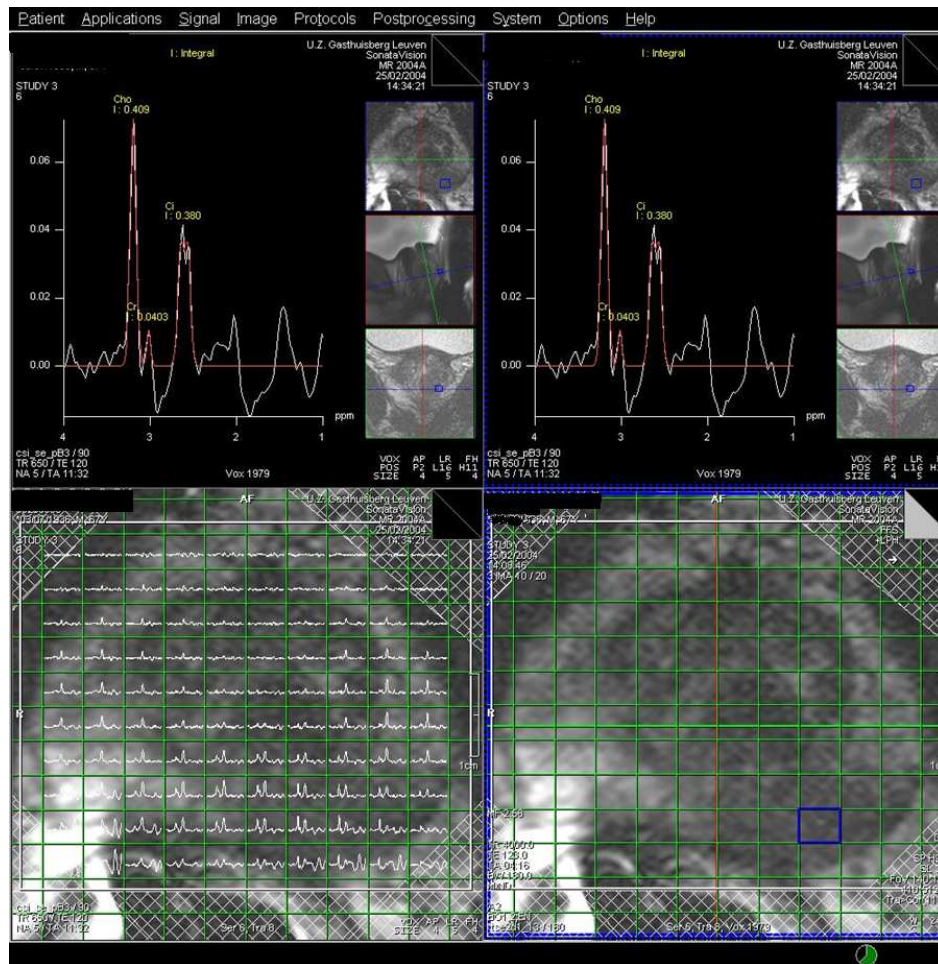


**Figure 5.9.** Screenshot provided by a Siemens scanner for an *in vivo* prostate MRSI data set.

parameters: up to 0.05 ppm for the frequencies, up to 40 times the original value of the damping factors, up to 20% of the original values of the amplitudes. Figure 5.10 shows the detection results obtained by applying CCA (left) as well as the results provided by ordinary correlation analysis (right), i.e. the single voxel model. In the nosologic images, the colors denote the tissue types as follows: the brown color denotes the aggressive tumor region, the red color represents the moderately aggressive tumor region, the orange color denotes the mixed tissue region and the light blue color corresponds to the healthy tissue region. In both images, some dark blue voxels can be observed as well. They correspond to voxels that have not been

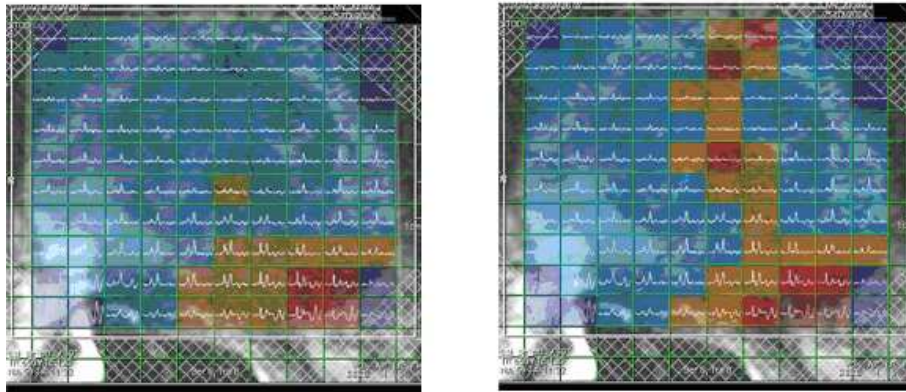


**Figure 5.10.** Nosologic images obtained by processing an *in vivo* MRSI data set. Left: CCA (spatial model: symmetric  $3 \times 3$ ; subspace model: Taylor). Right: ordinary correlation analysis. Brown region: aggressive tumor voxels; red region: moderately aggressive tumor voxels; orange region: mixed tissue voxels; light blue region: healthy tissue voxels, dark blue region: unprocessed voxels.

processed by the segmentation techniques since they are covered by the saturation blocks used for fat suppression around the prostate (see the spectral map in Figure 5.9). As can be observed, CCA is able to localize the suspicious tumor part, while the single voxel model detects as tumor/mixed tissue a much broader region. In particular, some tumor voxels are detected on the upper part of the grid.

In Figure 5.11 and Figure 5.12 the canonical coefficient maps obtained by CCA and the single voxel model, respectively, are visualized for each tissue type.

The maps show that the canonical coefficients provided by CCA are significantly larger than the coefficients provided by the single voxel approach, which points out that the spectra contained in the voxels detected by CCA correlate best with the chosen model spectra, i.e. with the first component of the  $\mathbf{y}$  variable.

As further evaluation of the performance of the two approaches, for each tissue region, the correlation coefficient between the spectrum obtained as average of the spectra contained in the detected voxels and the model spectrum was computed. In Figure 5.13 the aforementioned spectra are displayed.

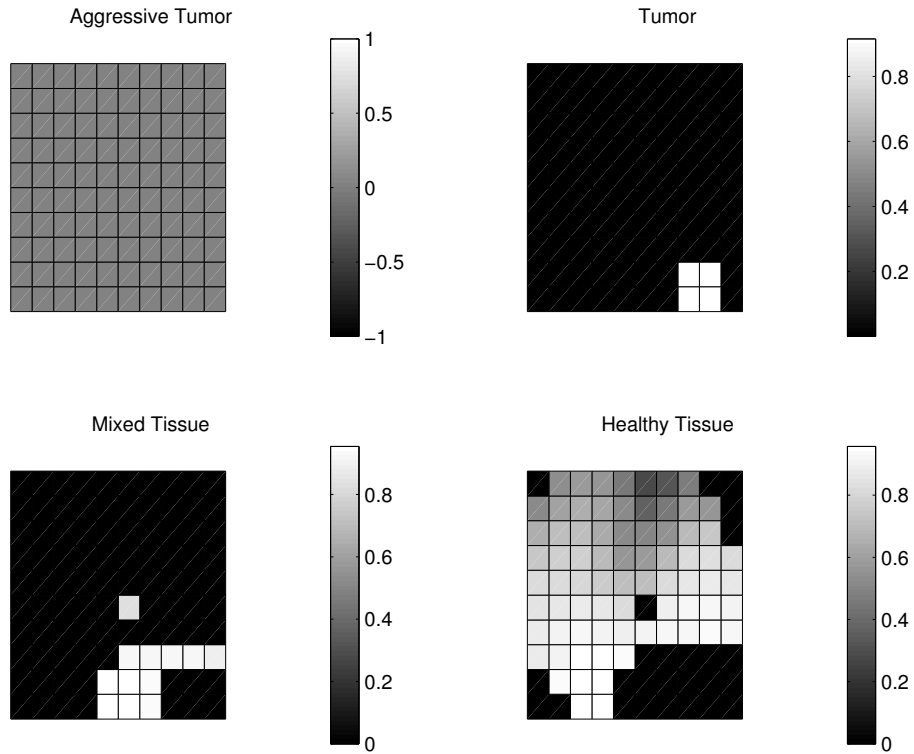


**Figure 5.11.** Canonical coefficient maps obtained for the in vivo MRSI data set by CCA (spatial model: symmetric  $3 \times 3$ ; subspace model: Taylor).

The obtained values, reported in Table 5.2, show a high level of correlation for both methods. However, CCA provides better results for the tumor and mixed regions.

Correlation coefficients	Aggressive tumor	Tumor	Mixed tissue	Healthy tissue
Taylor symmetric $3 \times 3$	ND	0.8464	0.9459	0.8581
Single voxel	0.8129	0.8047	0.8850	0.8697

**Table 5.2.** Correlation coefficients between the average spectrum and the model spectrum for each detected tissue region. ND stands for not detected, i.e. no aggressive tumor voxels have been detected.

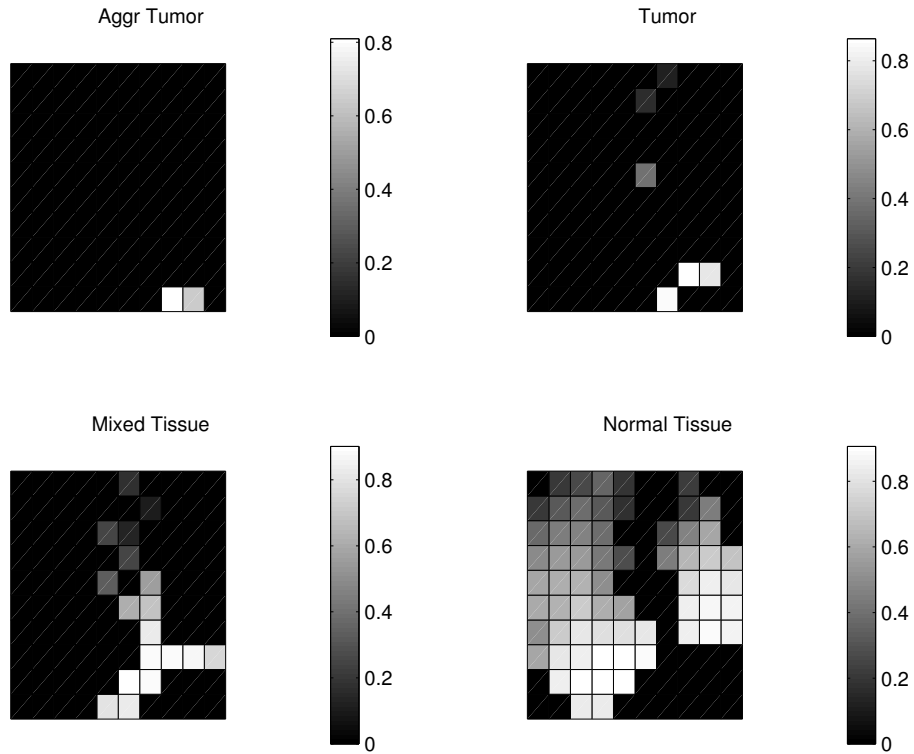


**Figure 5.12.** Canonical coefficient maps obtained for the in vivo MRSI data set by ordinary correlation analysis.

## 5.6 Conclusions

CCA is a statistical technique that quantifies the relationship between multivariate random vectors. Our studies show that it can be applied successfully to MRSI data sets since it fully exploits the spatio-spectral nature of this type of biomedical data. In particular, in this chapter we showed that CCA can be applied to MRSI data in order to retrieve in an efficient and accurate way the possible tissue types characterizing the organ under investigation. Extensive simulation and in vivo studies were performed and described. They show that CCA significantly outperforms the ordinary correlation analysis, especially for signals with a low Signal to Noise Ratio.

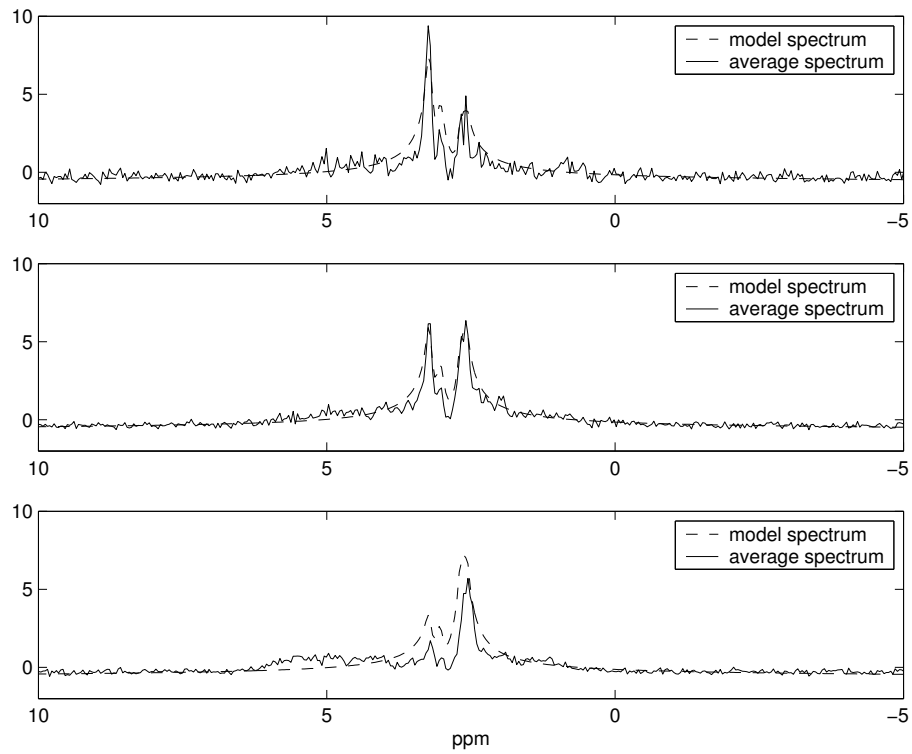


**Figure 5.13.** Model and average magnitude spectra for aggressive tumor (top), mixed tissue (middle) and normal tissue (bottom) obtained by applying CCA to the in vivo MRSI data set. Spatial model: symmetric  $3 \times 3$ . Subspace model: Taylor.

**FAST NOSOLOGICAL  
IMAGING OF 2DTSI BRAIN  
DATA BASED ON CCA**

*The purpose of this chapter is to investigate the potential and limitations of the tissue typing technique introduced in Chapter 5 when applied to brain data instead of prostate data. In fact, brain tumors differ significantly from prostate tumors since they are frequently very heterogeneous. The data considered in this study were acquired with two-dimensional Turbo Spectroscopic Imaging (2DTSI) sequences, characterized by limited acquisition times compared to those required for standard CSI data. CCA is applied to 2DTSI data in order to assess its ability to detect and classify tissues even when a high degree of heterogeneity is present in the considered sample.*

*The chapter is structured as follows. In Section 6.1 the main biochemical features of brain tumors are briefly described. In Section 6.2 turbo spectroscopic imaging is introduced and its potential and limitations are pointed out. Section 6.3 is devoted to the application of the CCA-based tissue typing technique introduced in Chapter 5 to 2DTSI brain data. Finally, in Section 6.4, the main conclusions are formulated.*

## 6.1 Biochemical features of brain tumors

As already specified in Section 1.2, also brain tumors can be detected by studying alterations in the metabolite levels. Although hundreds of neurochemical compounds are present in the human brain, only a few are detected by  $^1\text{H}$  MRS and the most important in brain tumor studies are: NAA (2.0 ppm), choline (3.2 ppm), creatine (3.0 ppm), lactate doublet (1.3 ppm), and lipids (0.9 and 1.3 ppm).

In general, a brain tumor is present when NAA and creatine levels are reduced, while choline levels are increased. Specifically, NAA is considered as a marker of neuronal/axonal density and viability and its decrease is associated with loss of neurons or axonal injury. Choline is almost inaccessible to MRS when considering healthy tissue since it is bound to cell membranes, myelin and lipids. However, in pathological conditions the choline contribution significantly increases as it reflects membrane, myelin and lipid turnover. Creatine plays a crucial role in cell energetic and mainly originates from intracellular metabolite pools of creatine and phosphocreatine. Generally, the choline and creatine peaks show similar intensities in healthy tissue. The creatine peak is the sum of creatine and phosphocreatine (PCr) with the same chemical shift of the CH<sub>3</sub> group. Lactate is considered as an energy marker. It is usually not detectable in healthy brain tissue and its concentration increases only under pathological conditions that are usually characterized by reduced oxidative metabolism or increased glycolysis. Finally, also lipids are not detectable in normal brain tissue as they are bound to macromolecules in membranes and myelin. When a severe pathology affects the brain, lipids result more mobile, thereby yielding a detectable resonance. Biopsy studies also show that lipids correlate with necrosis, which is a histological characteristic of high grade tumors [32]. All these alterations can be detected by MRSI since, unlike conventional neuroimaging, it provides neurochemical and spatial information. In particular, MRSI enables the simultaneous analysis of different parts of a lesion and also surrounding and contralateral areas. This property is very important when studying brain tumors since

these are often heterogeneous and may be characterized by the presence of viable tumor cells, cysts, zones of proliferation and necrosis, edema, and in the case of highly infiltrative tumors such as gliomas, there may also be contributions from normal brain tissue. Furthermore, tumor growth is not well regulated since variations in cellular metabolism and cell density occur, and as a tumor progresses, it may contain cells of different grades.

Finally, the ability to spatially map the biochemical information allows a more accurate presurgical diagnosis, such as that one based on biopsy, and surgical approach.

## 6.2 Turbo Spectroscopic Imaging applied to brain

In the previous chapters of this thesis the potential of MRSI as a non-invasive diagnostic tool has constantly been highlighted. Unfortunately, the acquisition of spatial spectroscopic information is limited by low metabolite concentrations and long acquisition times. In fact, in order to obtain well resolved spectra with good SNR, high field systems are needed. Moreover, the acquisition of slices with large number of volume elements and high spatial resolution require long acquisition times (usually more than 30 minutes). Therefore, in order to introduce MRSI more firmly into routine clinical use, MRSI techniques should offer multislice measurements, high spatial resolution, better outer volume suppression (to suppress skull lipids), faster acquisition sequences, and, eventually, automated processing and classification.

A technique that satisfies some of the aforementioned properties is the so-called Turbo Spectroscopic Imaging (TSI) technique. It is analogous to the turbo spin-echo imaging technique that allows the acquisition of MRSI data with relatively high spatial resolution in a significantly shorter period of time ( $\approx 6$  minutes with a turbo factor of 3 and a matrix size equal to  $24 \times 24$ ) [21]. In the literature, several studies exist in which TSI data are compared to SVS data (e.g. see [41]). Generally, a very good qualitative agreement is observed between SVS spectra and TSI spectra, although, sometimes, TSI spectra show a higher contamination from lipids which are either not evident or much lower in amplitude in the SVS spectra.

In this chapter CCA is applied to several 2DTSI brain data sets measured in patients affected by a glioblastoma tumor. The aim is twofold: to carry out a validation study on CCA when applied as a tissue typing technique to heterogeneous tumors, and to develop an MRSI technique that is able to combine a fast acquisition procedure (TSI) with a reliable and fast classification method (CCA).

## 6.3 Tissue segmentation and classification of 2DTSI brain data using CCA

### 6.3.1 Acquisition of 2DTSI brain data

The data were acquired at the Clínica Quirón, Servicio de Radiología, Valencia (Spain). Several days before the spectroscopy study, a full high resolution MRI

study with Gadolinium injection was acquired. After imaging with turbo spin echo T2 and proton density weighted images ( $TR = 5154$  ms,  $TE = 13$  and  $115$  ms), five MR spectroscopy experiments were acquired by 2DTSI in a 1.5 T Philips Gyroscan Intera NT (Philips Medical Systems, The Netherlands) using a  $90^\circ - 180^\circ - 180^\circ$  pulse sequence. Signals from surrounding cortical and bone areas were suppressed with 12–16 saturation slabs perpendicular to the acquisition plane (see Figures 6.1 and 6.2). Shimming and tuning were achieved with an automated procedure before acquisition. The water signal was suppressed with selective excitation. The multi-voxel spectroscopic images consist of a grid of  $24 \times 24$  voxels with a field of view of  $230 \times 230$  mm and a slice thickness of 20 mm. Each volume unit dimension was  $9.6 \times 9.6 \times 20$  mm (1.8 ml). The acquired signals are long echo time signals with  $TE = 272$  ms, and  $TR = 2000$  ms. They consist of 256 complex data points. Data processing also included zero filling to 512 points, removal of the residual water resonance by using HLSVD-PRO [35], and Fourier transformation.

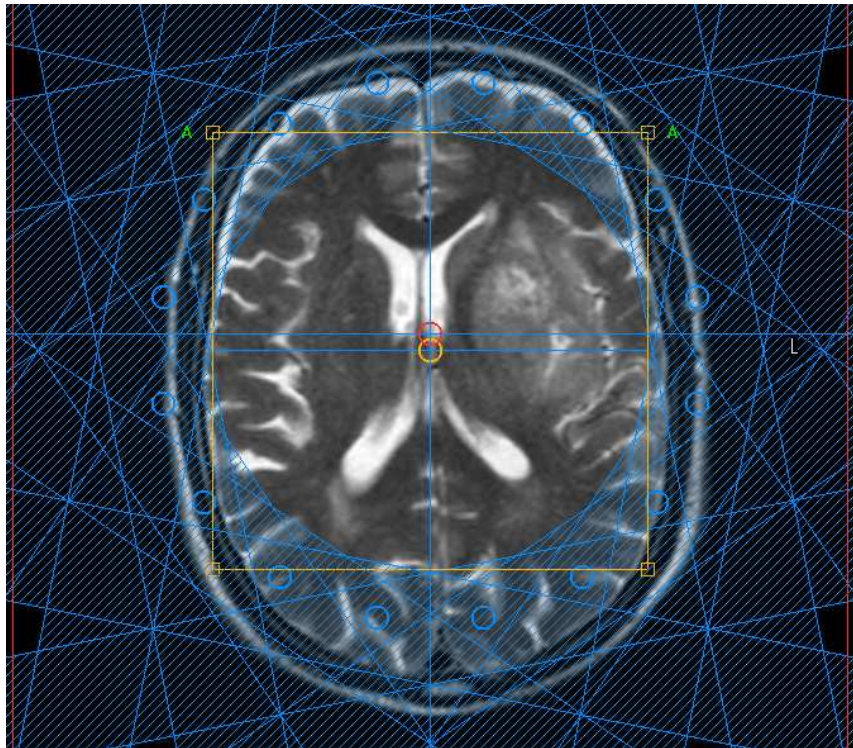


**Figure 6.1.** Transversal view image showing the 12 saturation slabs perpendicular to the acquisition plane.

A set of non-suppressed water spectra was also collected in the same sequence

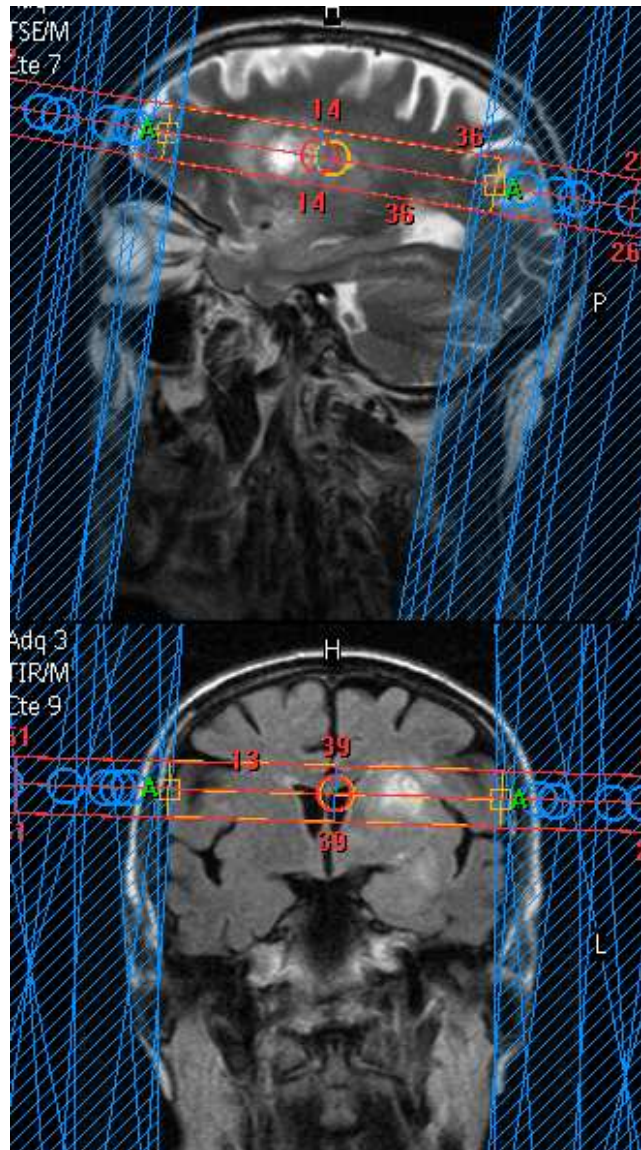


**Figure 6.2.** Sagittal (top) and coronal (bottom) view images showing the 12 saturation slabs perpendicular to the acquisition plane.

acquisition with a lower resolution (a grid of  $12 \times 12$  voxels with size  $19.2 \times 19.2 \times 20$  mm, 7.35 ml) as a reference in order to automatically correct the phase over the 2DTSI grid. The water resonance data in the reference set of spectra were used in

the reconstruction for correction of chemical shift and amplitude differences due to magnetic field inhomogeneity. Spectra quality was controlled through the shape, the width at half height, and the intensity of the water resonances measured with jMRUI software ([42], [23]). These methodological control parameters remained constant for all  $^1\text{H}$  MRS studies, indicating a stable magnetic field homogeneity [6].

### 6.3.2 CCA applied to 2DTSI brain data: selection of the model spectra

As already specified in Section 6.2, the data were measured in the brain of five patients affected by glioblastoma. In order to apply CCA, model spectra of the possible tissue types are needed, that may characterize a brain affected by glioblastoma. Such models are constructed by first selecting from the given data sets some spectra that, based on spectroscopy, the MRI, and the Gadolinium enhancement features, can be considered as characteristic of tissues found in glioblastoma tumors. Then, all the selected spectra corresponding to the same tissue type are averaged in order to take into account possible variations that affect *in vivo* data. In the examples under investigation several spectra could be selected as representative of the following tissue types: tumor, edema, normal, infiltration, necrosis, and axonal damage. In addition, mixed tissue types could be recognized, namely mixed tissue containing tumor and necrosis, and mixed tissue containing tumor and healthy cells. In this study, the former will be called Tumor+Necrosis tissue and the latter mixed tissue. Finally, some lipid spectra due to the presence of the skull were also considered since they sometimes may affect the border regions of the processed area of interest.

Table 6.1 shows the exact number of selected spectra for each example and for each tissue type.

Tissue	Example 1	Example 2	Example 3	Example 4	Example 5
Tumor	5	3	5	6	7
Edema	11	2			
Normal	14	9	6	5	5
Infiltration		1		5	
Tumor+Necrosis			6		
Necrosis			6	5	
Axonal damage					5
Mixed	6				
Lipids			3		

**Table 6.1.** Tissue patterns and corresponding number of selected spectra for each data set.

Note that when a data set is analysed, e.g. the data set related to Example 1, the spectra selected for the example under investigation do not contribute to the afore-

mentioned averaging procedure, i.e. all the selected spectra for the same tissue type are averaged except those corresponding to Example 1. Thus, the model spectra used to analyze Example 1 are obtained as the average of the only selected spectra of Examples 2, 3, 4 and 5. Moreover, since only a few spectra could be selected for Tumor+Necrosis tissue from the given examples, some more Tumor+Necrosis spectra were produced as the average of tumor spectra and necrosis spectra. The same procedure was applied to produce a higher number of mixed tissue spectra.

### 6.3.3 CCA applied to 2DTSI brain data: selection of the subspace and spatial models

Concerning the choice of the spatial model, as already described in Section 5.3.1, several multi-voxel approaches can be applied. The same spatial models, as in Section 5.3.1, were applied to the brain data considered in this chapter and the best performance was obtained by applying the symmetric  $3 \times 3$  model without corner voxels. When applying CCA a subspace model is also needed. In Section 5.3.2 two possible subspace models were introduced, namely the Taylor and PCA subspace models. Here, the Taylor subspace model is adopted and its components are defined as follows: the first component is set equal to the tissue model spectrum defined above (in Section 6.3.2), the second and third components are set equal to the first order derivative of the first component approximated as the first and second order finite differences, respectively. The Taylor model is preferred over the PCA model since only a few characteristic spectra are available for some tissue types and, therefore, no useful matrix  $\mathbf{D}$  can be constructed on which a principal component analysis can be performed. In fact, as explained in Section 5.3.2, the second component of the PCA model is obtained by performing principal component analysis on a matrix containing a large number of spectra, which is not the case in this study.

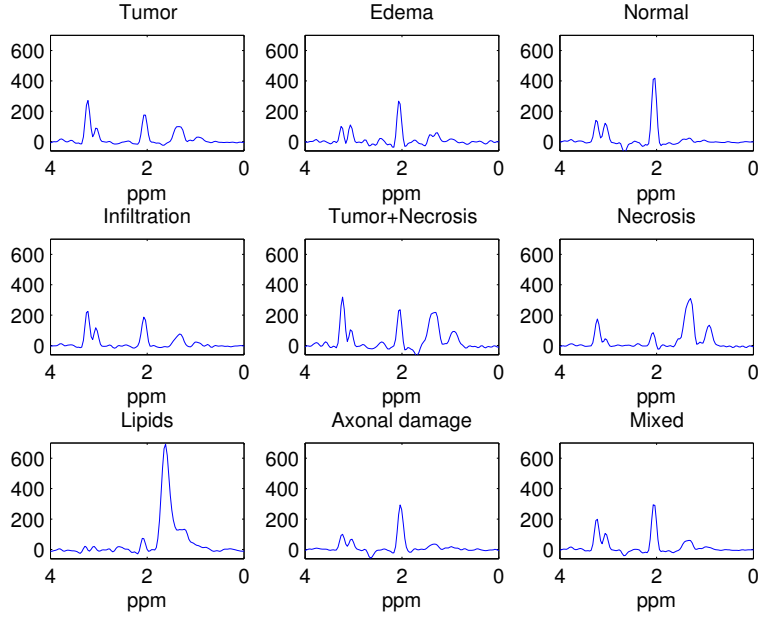
In the following sections, the detection results are illustrated. As in Chapter 5, our aim is to compare the performance of ordinary correlation analysis, which does not exploit any spatial information characterizing the 2DTSI data, and the performance of CCA. The nosologic images obtained by both methods are reported and the tissue regions are visualized on gray scale. The displayed correlation maps can be used for a correct identification of such regions. Note that the black border voxels represent voxels that have been excluded from the processing as they are covered by the saturation slabs.

### 6.3.4 Detection results: Example 1

Figure 6.3 shows the tissue model spectra used to construct the subspace model of Example 1. These spectra clearly show that the considered tissue types are characterized by different contributions of the metabolites of interest.

Figure 6.4 shows a screenshot provided by the Philips scanner in which the lesion and the corresponding spectral map can be observed. Only the area of interest of

the  $24 \times 24$  acquired data matrix was processed, namely from row 8 to row 17 and from column 7 to column 17.



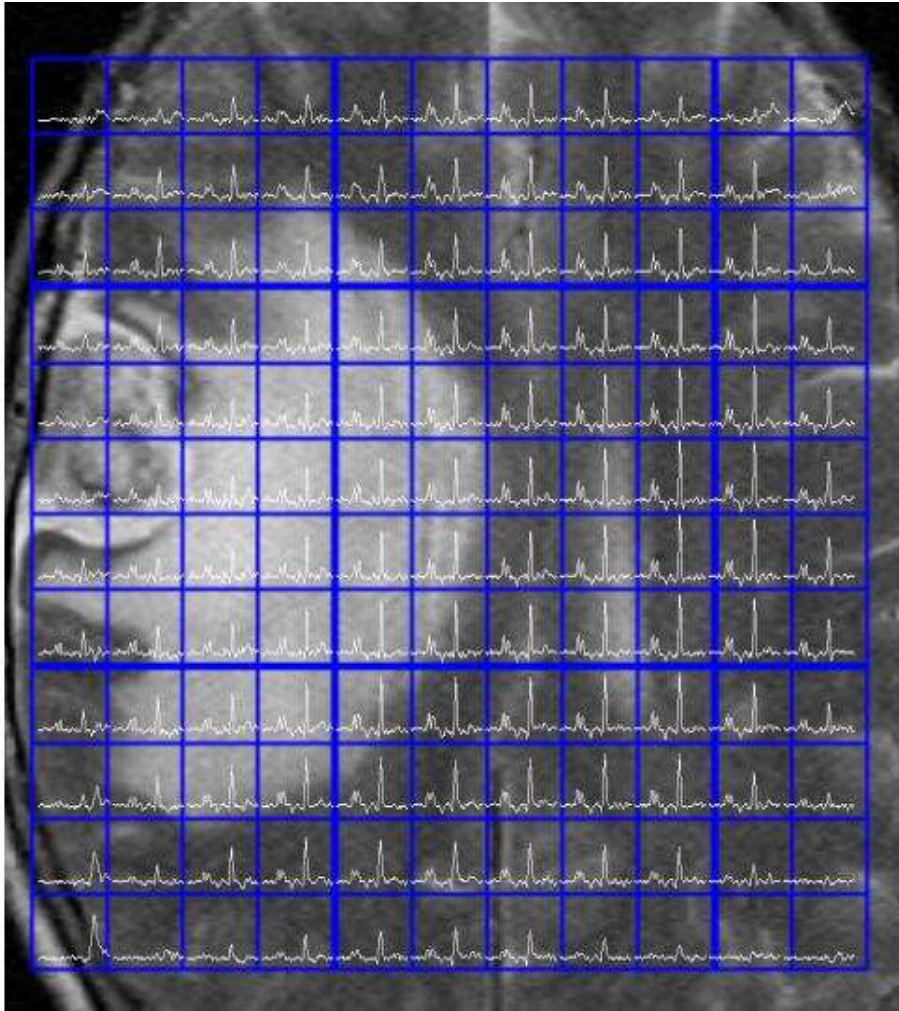
**Figure 6.3.** Real part of the tissue model spectra used in the Taylor subspace model of Example 1.

Figure 6.5 shows the nosologic image (top) and all the correlation maps (bottom), corresponding to the different tissue types, obtained by applying CCA.

Figure 6.6 shows the nosologic image (top) and all the correlation maps (bottom), corresponding to the different tissue types, obtained by applying ordinary correlation analysis.

As can be observed in the above mentioned figures, CCA is able to detect only three types of tissue, namely normal, axonal damage and mixed tissue. In particular, the tumor region is detected as mixed tissue. Moreover, based on spectroscopy, an edema region can be recognized in the right-hand side of the lesion, but this is not detected by CCA. The reason of these results may be due to the size of the lesion and to its location. In fact, the lesion is not so big and is very close to the skull.

Ordinary correlation analysis does not provide better results. It detects the tumor region as mixed and Tumor+Necrosis tissues. It also detects some edema voxels, but their location is wrong. Furthermore, the correlation coefficient values displayed in the correlation maps are significantly smaller than the canonical coefficients obtained by CCA.



**Figure 6.4.** Screenshot provided by the Philips scanner for Example 1.

Finally, as further evaluation of the performance of the two approaches, for each tissue region, the correlation coefficient between the spectrum obtained as average of the spectra contained in the detected voxels and the model spectrum was computed. The obtained values, reported in Table 6.2, show a high level of correlation for both methods.

Tissue	CCA	ordinary correlation analysis
Tumor	ND	ND
Edema	ND	0.8876
Normal	0.9790	0.9703
Infiltration	ND	ND
Tumor+Necrosis	ND	0.7871
Necrosis	ND	ND
Axonal damage	0.9572	0.9603
Mixed	0.8645	0.8587
Lipids	ND	ND

**Table 6.2.** Example 1. Correlation coefficients between the average spectrum and the model spectrum for each detected tissue region. ND stands for not detected, i.e. no aggressive tumor voxels have been detected.

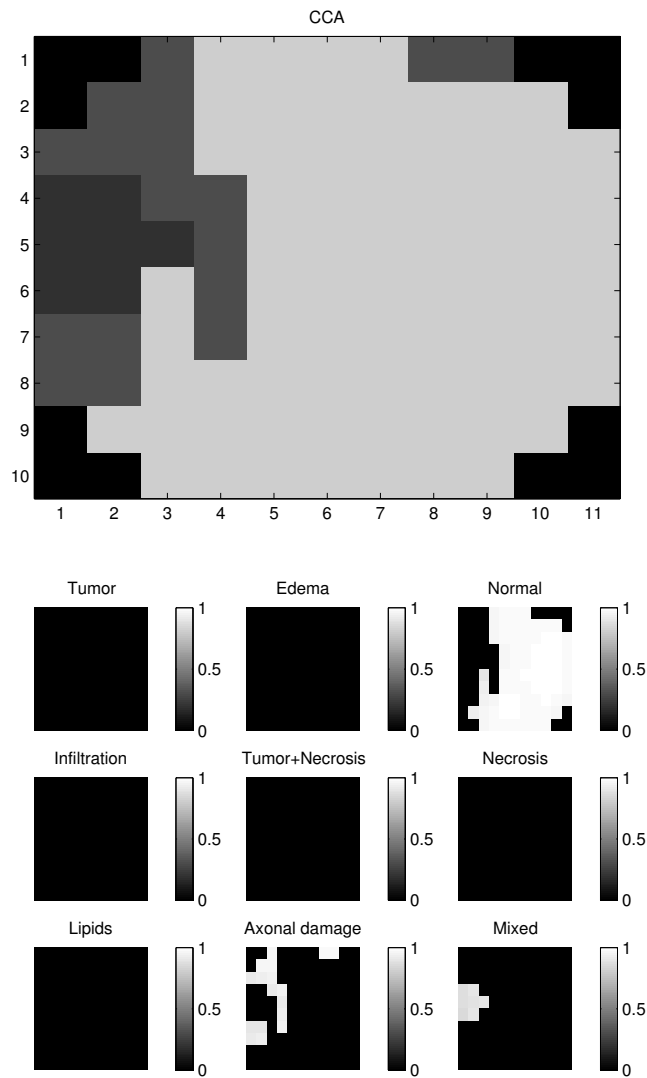


**Figure 6.5.** Example 1. Top: nosologic image obtained by CCA. Spatial model: symmetric  $3 \times 3$  without corner voxels. Subspace model: Taylor. Bottom: correlation maps corresponding to all the tissue types.

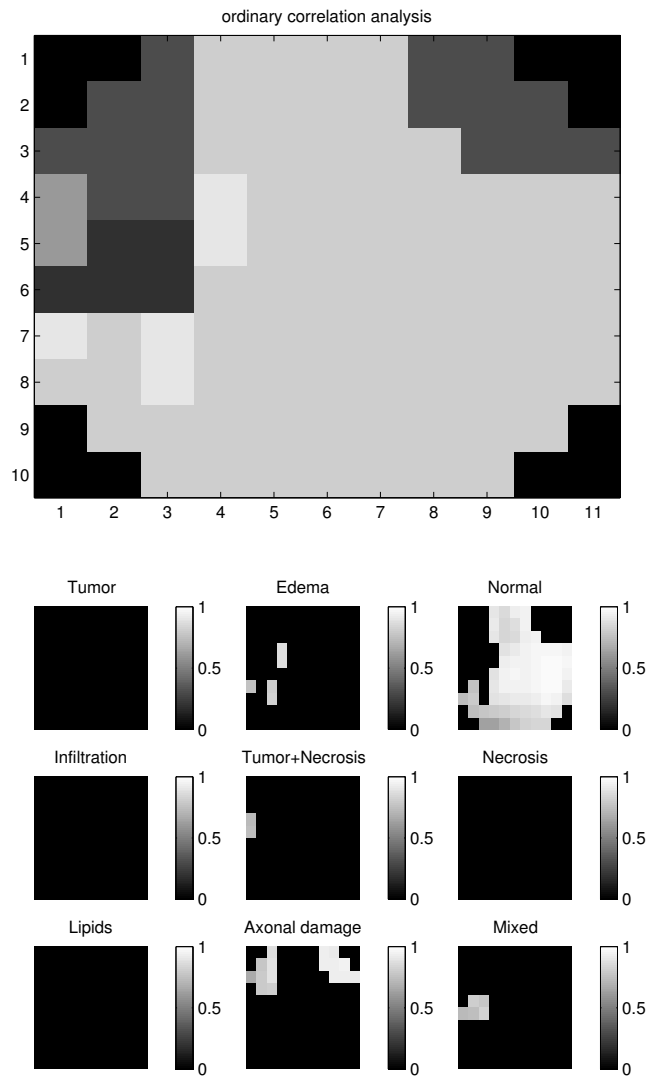


**Figure 6.6.** Example 1. Top: nosologic image obtained by ordinary correlation analysis. Bottom: correlation maps corresponding to all the tissue types.

### 6.3.5 Detection results: Example 2

Figure 6.7 shows the tissue model spectra used to construct the subspace model of Example 2. Also in this case, the spectra clearly show that the considered tissue types are characterized by different contributions of the metabolites of interest.

Figure 6.8 shows a screenshot provided by the Philips scanner in which the lesion as well as the spectral map can be observed. The slice of interest is the 15th slice.

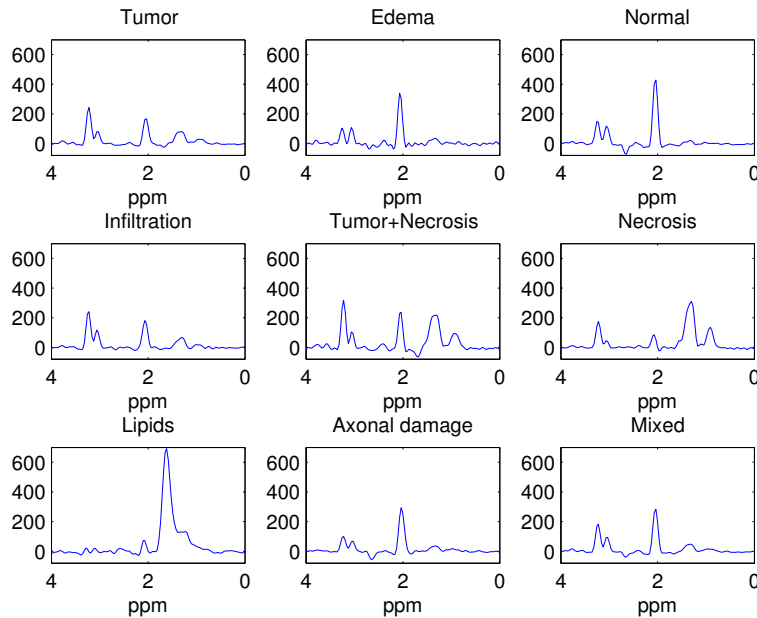


**Figure 6.7.** Real part of the tissue model spectra used in the Taylor subspace model of Example 2.

Once again, only the area of interest is processed, namely from row 8 to row 21 and from column 7 to column 17. Figure 6.9 shows the nosologic image (top) and all the correlation maps (bottom), corresponding to the different tissue types, obtained by applying CCA, while Figure 6.10 shows the results obtained by applying ordinary correlation analysis.

As can be observed in the figures, both methods are able to describe the tumor region by the mixed tissue and the Tumor+Necrosis tissue, but CCA is more accurate. Moreover, CCA significantly outperforms ordinary correlation analysis in detecting the edema and normal areas. Some lipid voxels are detected equally well by both techniques, but, as already explained in Section 6.3.2, they are due to the presence of the skull. Finally, the values displayed in the correlation maps obtained

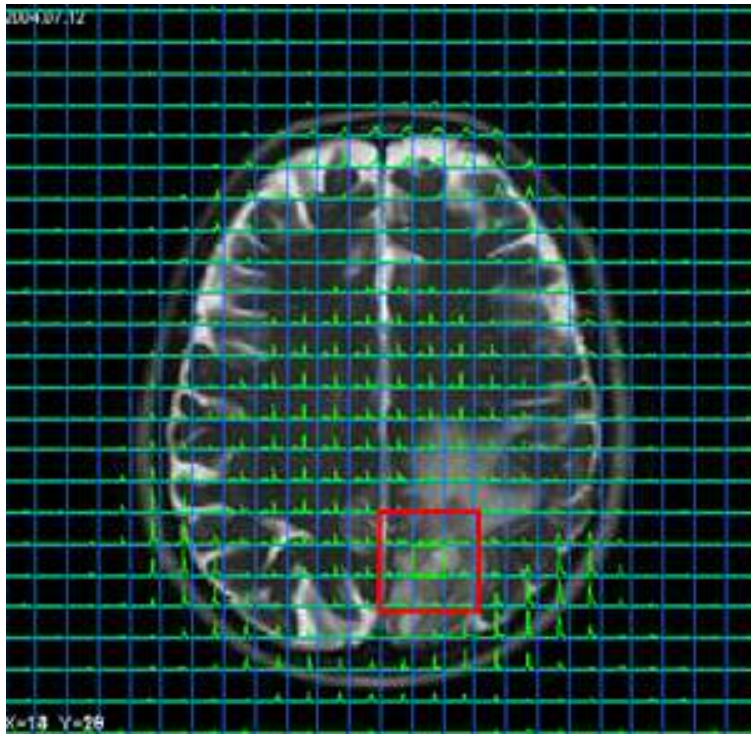


**Figure 6.8.** Screenshot of the 15th slice provided by the Philips scanner for Example 2.

by ordinary correlation analysis are significantly smaller than the canonical coefficients obtained by CCA.

Table 6.3 shows the correlation coefficient between the spectrum obtained as average of the spectra contained in the detected voxels and the model spectrum.

### 6.3.6 Detection results: Example 3

Figure 6.11 shows the tissue model spectra used to construct the subspace model of Example 3. Figure 6.12 shows a screenshot provided by the Philips scanner in which the lesion can be observed. The slice of interest is the 13th slice.

Figure 6.13 shows the area of interest of the image in Figure 6.12 and the corresponding spectral map. Some spectra are also pointed out as characteristic of some tissue types.

The area of interest is processed, namely from row 8 to row 17 and from column 7 to column 17. Figure 6.14 shows the nosologic image (top) and all the correlation maps (bottom), corresponding to the different tissue types, obtained by applying CCA, while Figure 6.15 shows the results obtained by applying ordinary correlation

Tissue	CCA	ordinary correlation analysis
Tumor	ND	ND
Edema	0.9477	0.9716
Normal	0.9564	0.9679
Infiltration	ND	ND
Tumor+Necrosis	0.8878	0.9089
Necrosis	0.5582	0.7110
Axonal damage	0.6054	0.4507
Mixed	0.9016	0.9158
Lipids	0.4581	0.4405

**Table 6.3.** Example 2. Correlation coefficients between the average spectrum and the model spectrum for each detected tissue region. ND stands for not detected, i.e., no aggressive tumor voxels have been detected.

analysis.

The example under investigation is much better characterized by CCA than ordinary correlation analysis. In fact, based on spectroscopy, CCA is able to well describe the different types of tissue that characterize the lesion. Moreover, ordinary correlation analysis fails with respect to the detection of the edema tissue, which is assigned to brain regions where only normal tissue is present.

Table 6.4 shows the correlation coefficient between the spectrum obtained as average of the spectra contained in the detected voxels and the model spectrum.

Tissue	CCA	ordinary correlation analysis
Tumor	0.9434	0.9515
Edema	ND	0.8886
Normal	0.9597	0.9808
Infiltration	0.9264	0.9493
Tumor+Necrosis	ND	0.9160
Necrosis	0.9064	0.8486
Axonal damage	0.7865	0.9150
Mixed	0.9848	0.9866

**Table 6.4.** Example 3. Correlation coefficients between the average spectrum and the model spectrum for each detected tissue region. ND stands for not detected, i.e., no aggressive tumor voxels have been detected.

### 6.3.7 Detection results: Example 4

Figure 6.16 shows the tissue model spectra used to construct the subspace model of Example 4. Figure 6.17 shows a screenshot provided by the Philips scanner in

which the lesion can be observed. The slice of interest is the 14th slice.

The area of interest, from row 8 to row 17 and from column 7 to column 17, is processed. This is shown in Figure 6.18 along with the corresponding spectral map. Some spectra are pointed out as characteristic of some tissue types.

Figure 6.19 shows the nosologic image (top) and all the correlation maps (bottom), corresponding to the different tissue types, obtained by applying CCA, while Figure 6.20 shows the results obtained by applying ordinary correlation analysis.

Similarly to Example 3, Example 4 is much better characterized by CCA than ordinary correlation analysis. Based on spectroscopy, CCA is able to “well describe” the different types of tissue that characterize the lesion. It is important to observe that the mixed tissue detected by CCA actually corresponds to the ventricular and periventricular normal appearing areas, which means that both Cerebral Spinal Fluid (CSF) and tissue are present in the detected mixed tissue voxels.

Table 6.5 shows the correlation coefficient between the spectrum obtained as average of the spectra contained in the detected voxels and the model spectrum.

Tissue	CCA	ordinary correlation analysis
Tumor	0.8996	0.8965
Edema	ND	0.8577
Normal	0.9789	0.9735
Infiltration	0.3860	0.6860
Tumor+Necrosis	0.9018	0.8957
Necrosis	0.9091	0.8613
Axonal damage	ND	0.7539
Mixed	0.9224	0.9681
Lipids	ND	ND

**Table 6.5.** Example 4. Correlation coefficients between the average spectrum and the model spectrum for each detected tissue region. ND stands for not detected, i.e., no aggressive tumor voxels have been detected.

### 6.3.8 Detection results: Example 5

Finally, Figure 6.21 shows the tissue model spectra used to construct the subspace model of Example 5. Figure 6.22 shows a screenshot provided by the Philips scanner in which the lesion can be observed. The slice of interest is the 16th slice.

The area of interest, from row 8 to row 17 and from column 7 to column 17, is processed. This is shown in Figure 6.23 along with the corresponding spectral map. Some spectra are pointed out as characteristic of some tissue types.

Figure 6.24 shows the nosologic image (top) and all the correlation maps (bottom), corresponding to the different tissue types, obtained by applying CCA, while Figure 6.25 shows the results obtained by applying ordinary correlation analysis.

CCA is able to “well localize” the tumor region which characterize the example

under investigation. On the contrary, ordinary correlation analysis detects an infiltration region where the tumor region is actually present. Moreover, ordinary correlation analysis detects a broader mixed tissue region. Finally, the detection of the edema voxels fails for both methods. Probably, the detection of edema is difficult as sometimes edema areas can be infiltrated and sometimes they are not. Table 6.6 shows the correlation coefficient between the spectrum obtained as average of the spectra contained in the detected voxels and the model spectrum.

Tissue	CCA	ordinary correlation analysis
Tumor	0.8439	ND
Edema	0.8611	0.9370
Normal	0.9806	0.9843
Infiltration	ND	0.9136
Tumor+Necrosis	ND	ND
Necrosis	ND	ND
Mixed	0.9412	0.9288
Lipids	ND	ND

**Table 6.6.** Example 5. Correlation coefficients between the average spectrum and the model spectrum for each detected tissue region. ND stands for not detected, i.e. no aggressive tumor voxels have been detected.

## 6.4 Conclusions

In this chapter a validation study on the application of CCA to 2DTSI brain data was carried out. In particular, the biochemical features of brain tumors and the advantages of acquiring MRSI data by using 2DTSI sequences were highlighted. The data were measured in patients affected by glioblastoma tumor, which represents one of the most heterogeneous tumors. Our studies show that CCA is a fast and reliable tissue typing technique since it is able to “well characterize” the different tissue regions of the brain, even when a high degree of heterogeneity is present. Moreover, the use of spatial information makes the detection results of CCA significantly better than those ones obtained by ordinary correlation analysis.

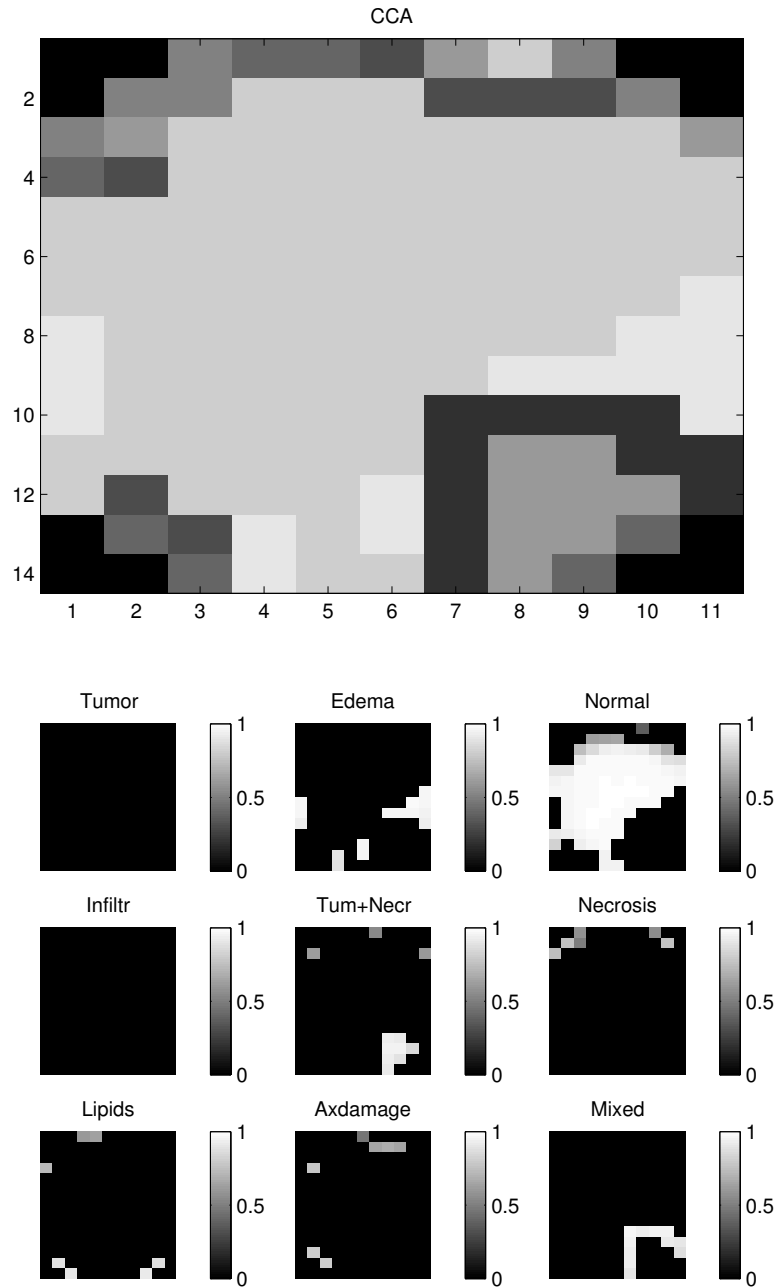


**Figure 6.9.** Example 2. Top: nosologic image obtained by CCA. Spatial model: symmetric  $3 \times 3$  without corner voxels. Subspace model: Taylor. Bottom: correlation maps corresponding to all the tissue types.

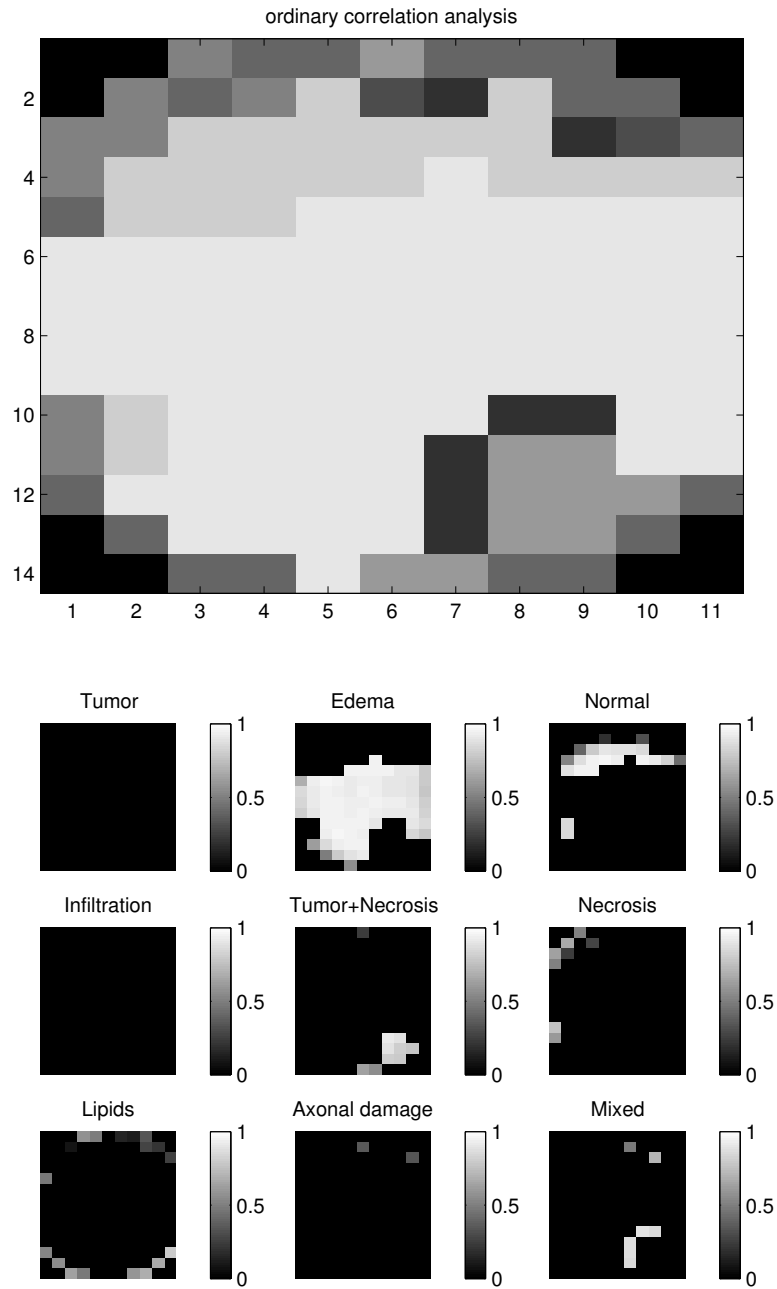


**Figure 6.10.** Example 2. Top: nosologic image obtained by ordinary correlation analysis. Bottom: correlation maps corresponding to all the tissue types.

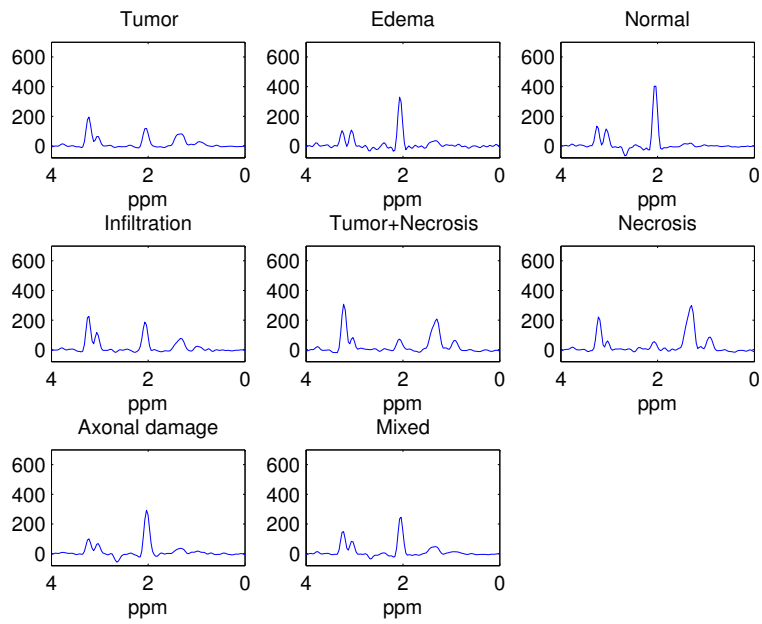


**Figure 6.11.** Real part of the tissue model spectra used in the Taylor subspace model of Example 3.

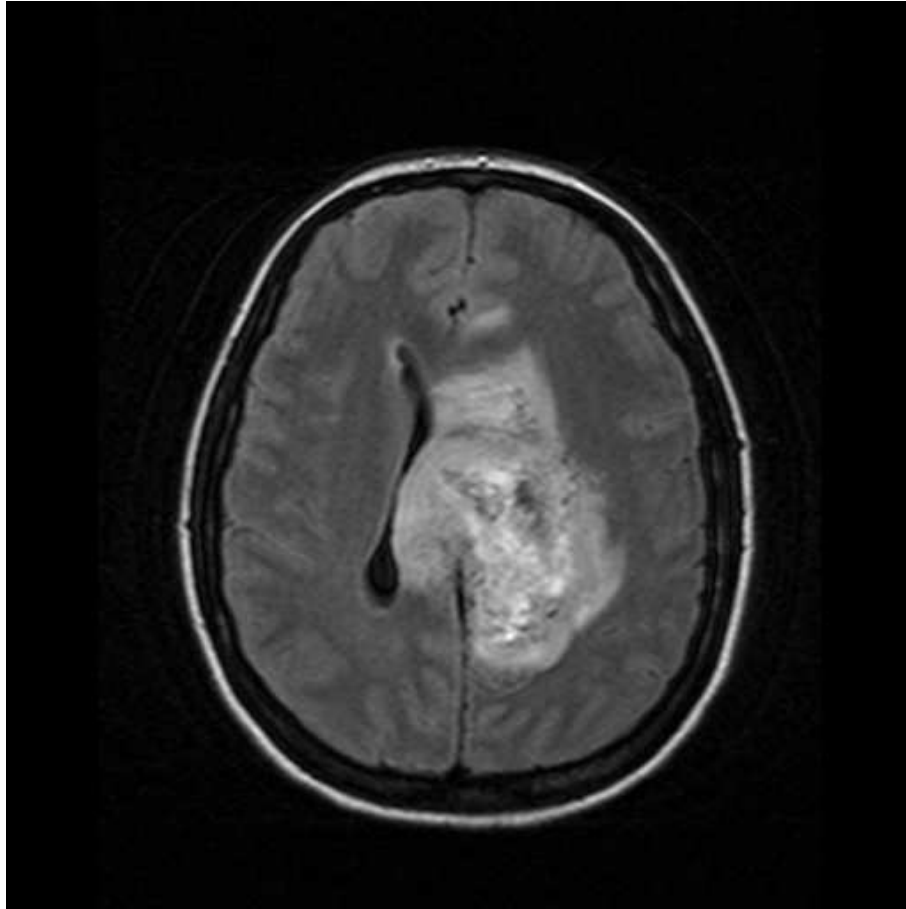


**Figure 6.12.** Screenshot of the 13th slice provided by the Philips scanner for Example 3.

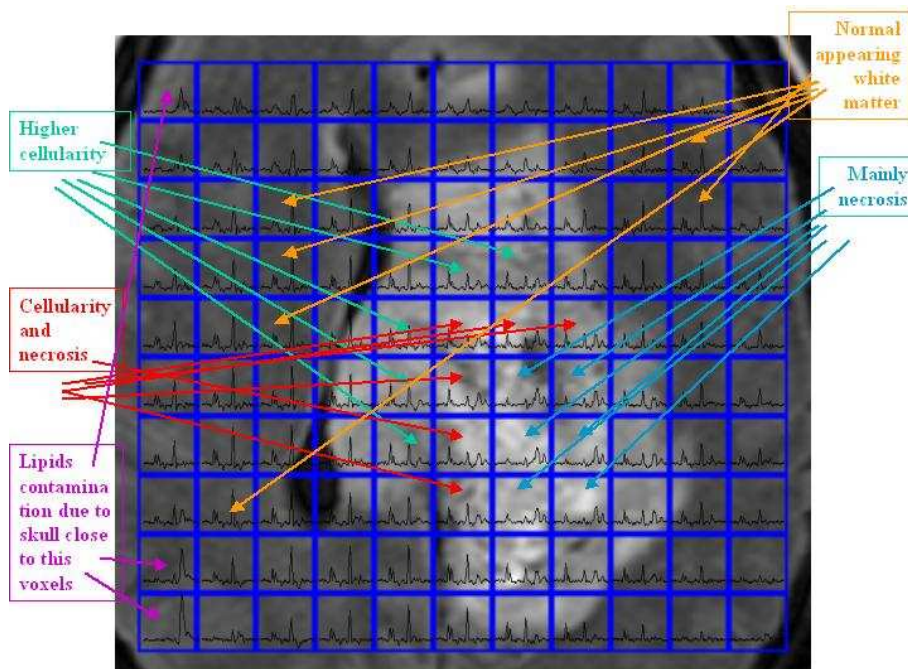
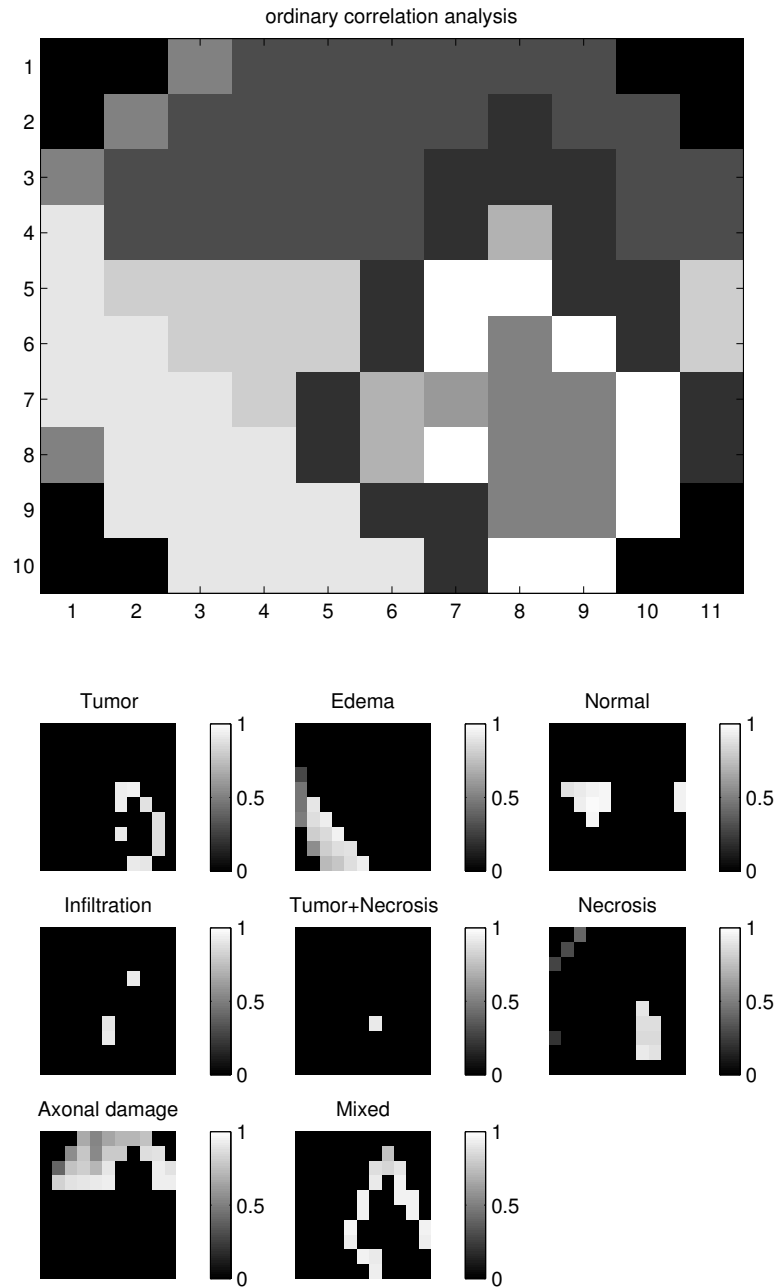
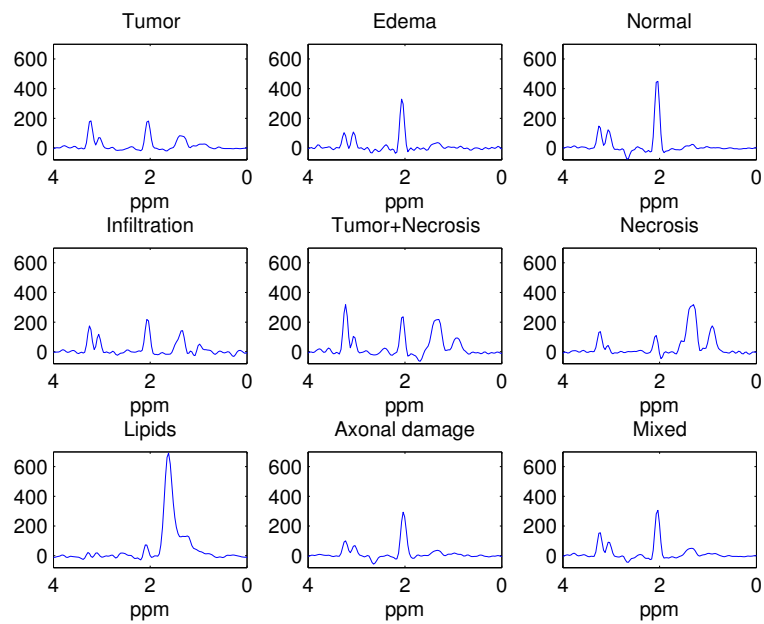


Figure 6.13. Area of interest of the 13th slice for Example 3.





**Figure 6.15.** Example 3. Top: nosologic image obtained by ordinary correlation analysis. Bottom: correlation maps corresponding to all the tissue types.



**Figure 6.16.** Real part of the tissue model spectra used in the Taylor subspace model of Example 4.

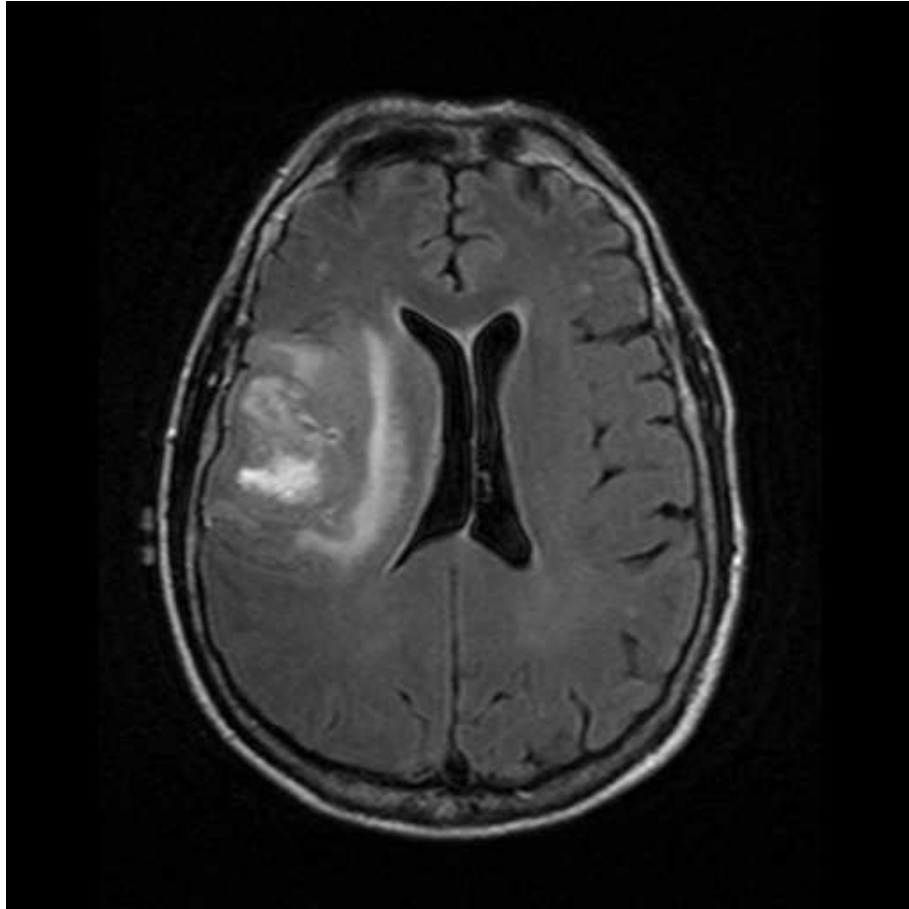


**Figure 6.17.** Screenshot of the 14th slice provided by the Philips scanner for Example 4.

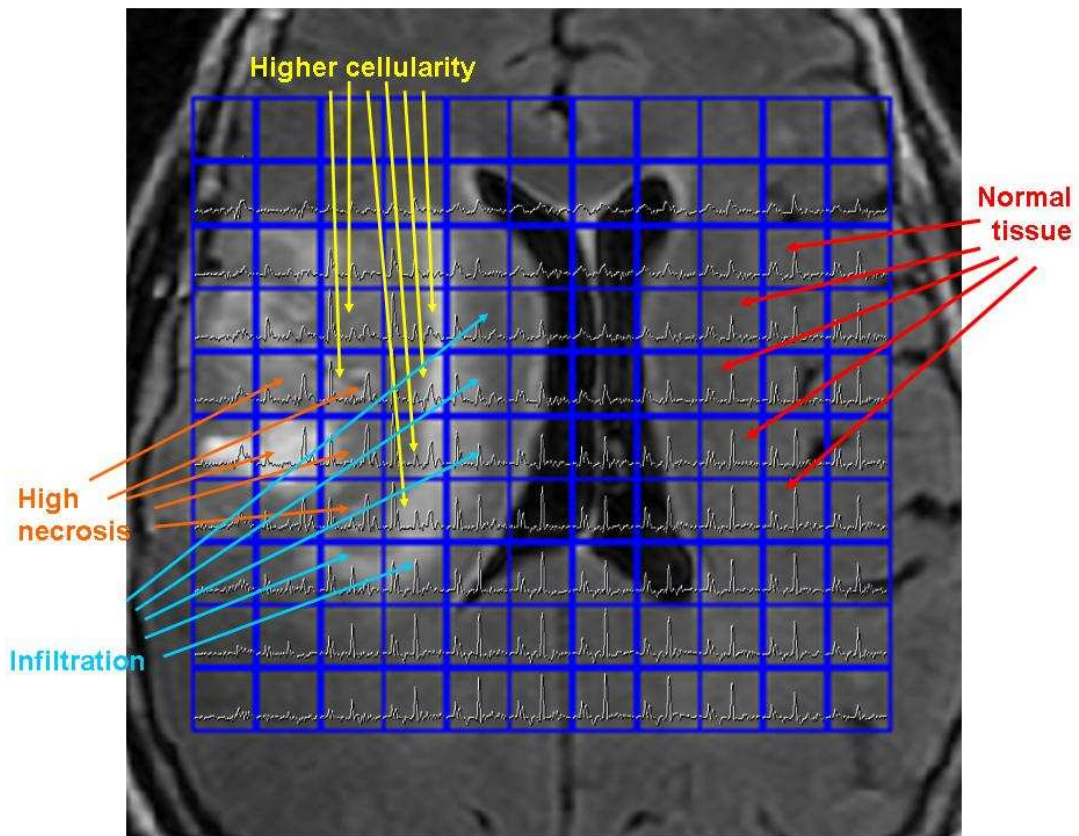
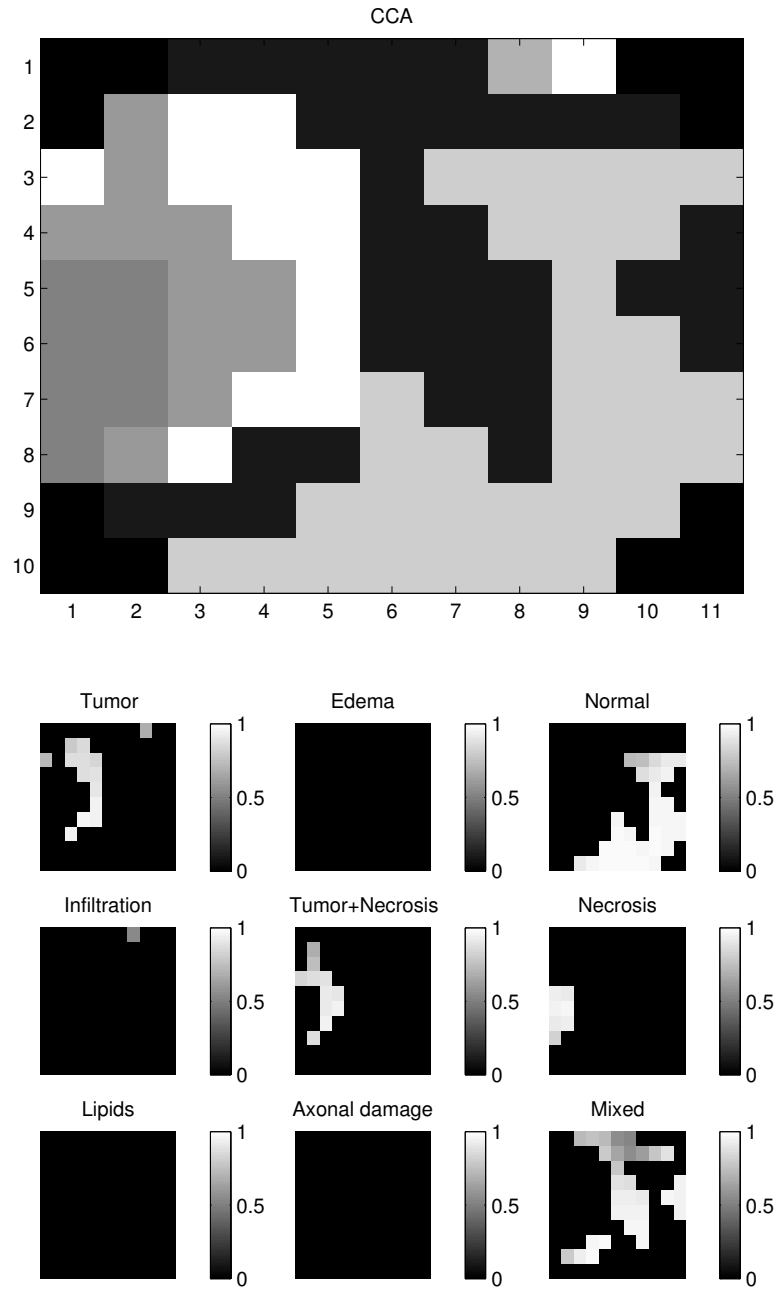
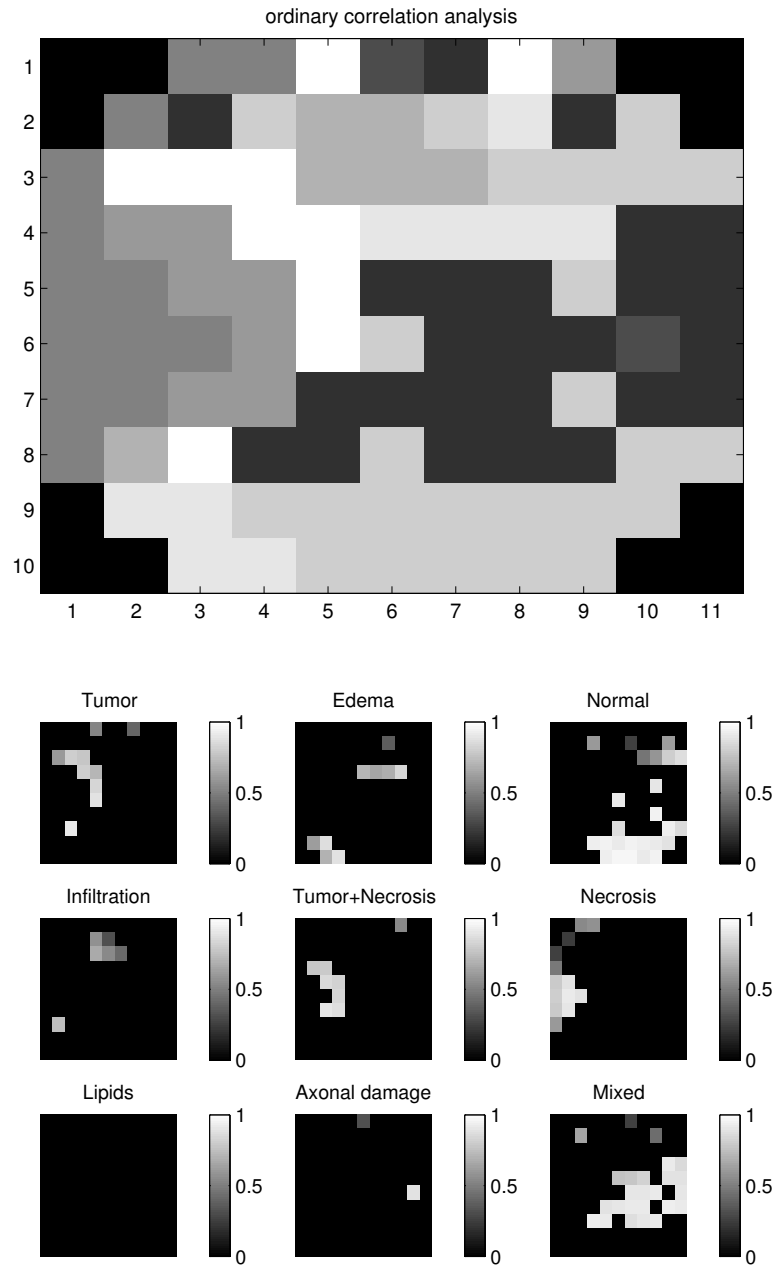


Figure 6.18. Area of interest of the 14th slice for Example 4.



**Figure 6.19.** Example 4. Top: nosological image obtained by CCA. Spatial model: symmetric  $3 \times 3$  without corner voxels. Subspace model: Taylor. Bottom: correlation maps corresponding to all the tissue types.



**Figure 6.20.** Example 4. Top: nosologic image obtained by ordinary correlation analysis. Bottom: correlation maps corresponding to all the tissue types.

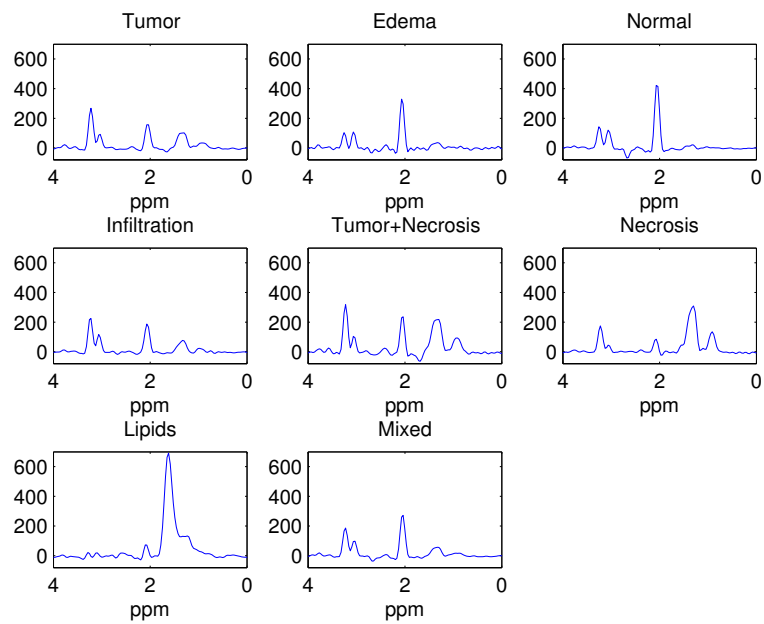


**Figure 6.21.** Real part of the tissue model spectra used in the Taylor subspace model of Example 5.

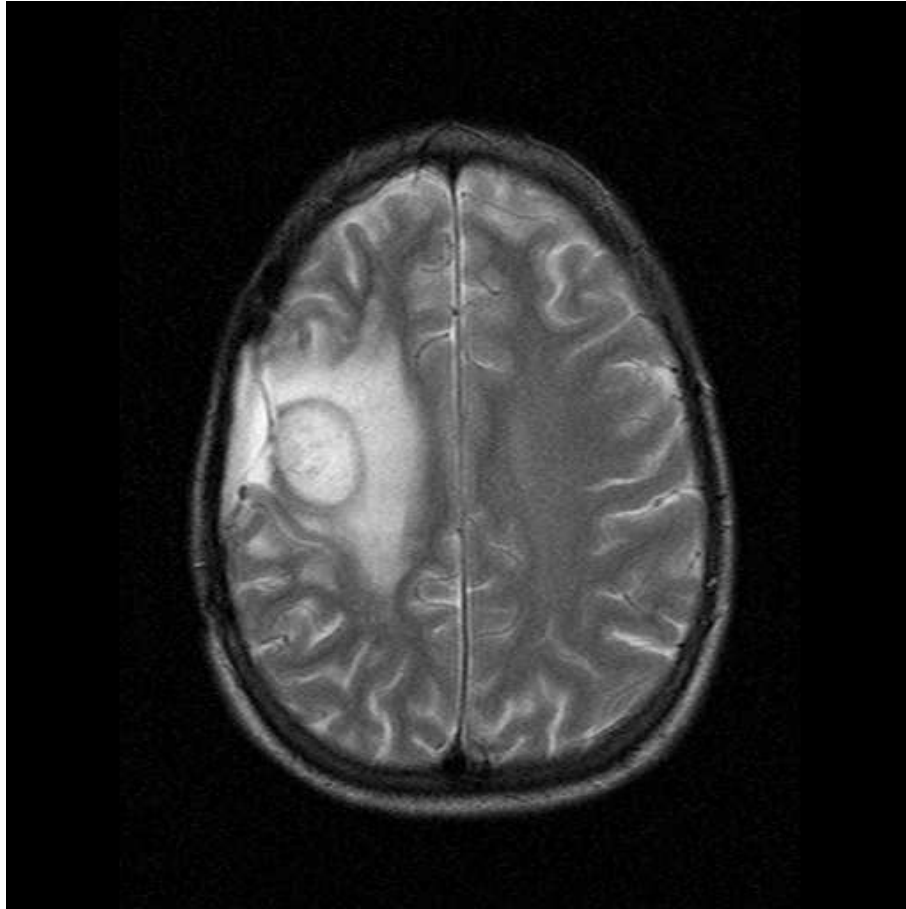


**Figure 6.22.** Screenshot of the 16th slice provided by the Philips scanner for Example 5.

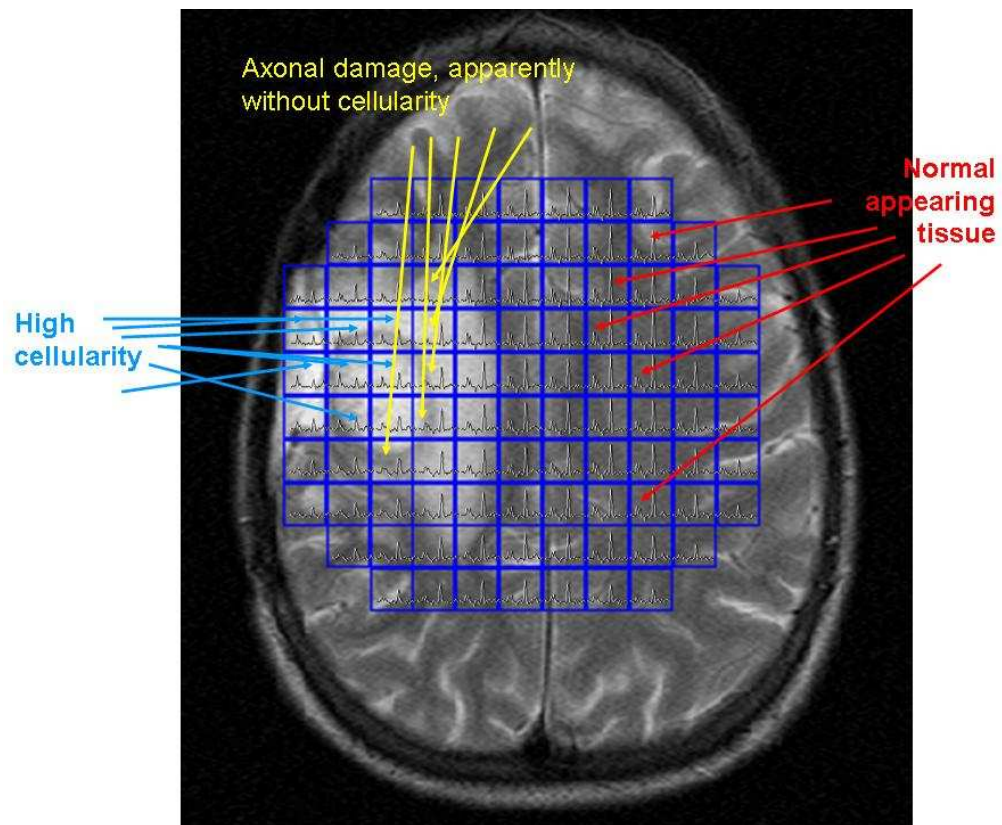
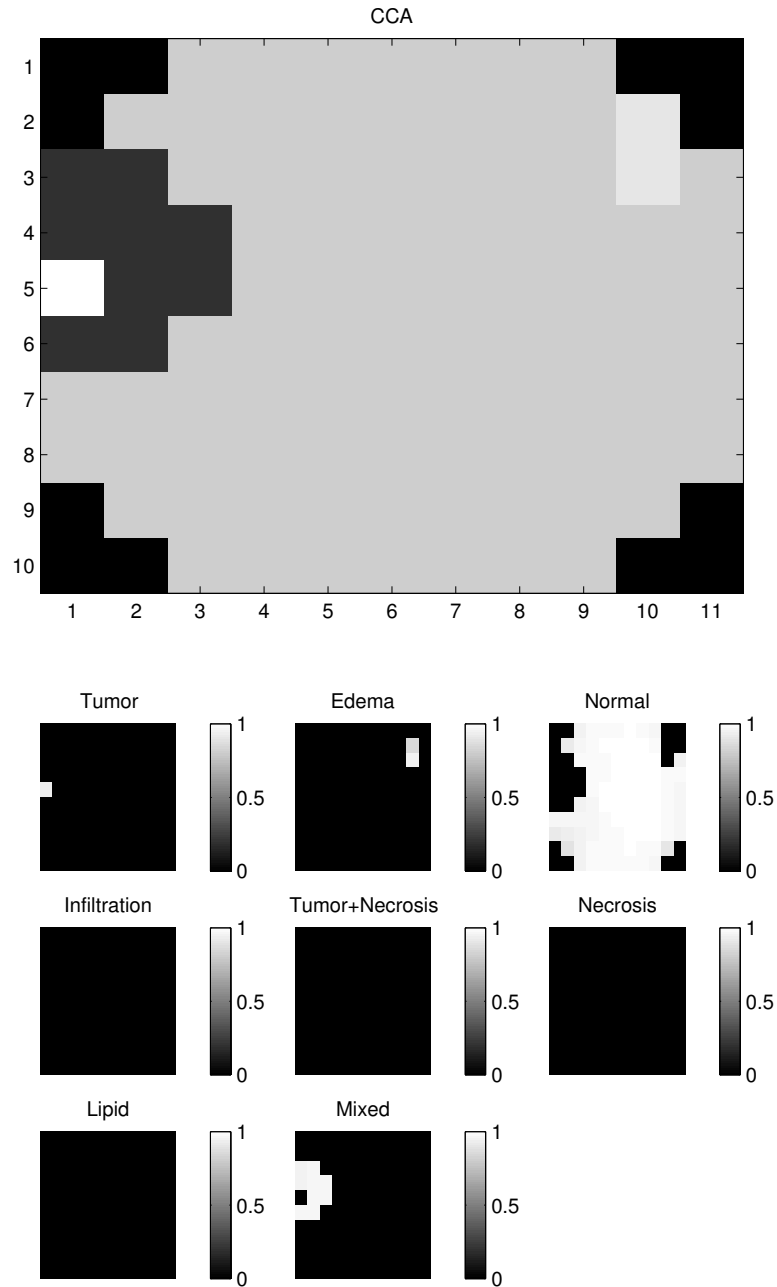
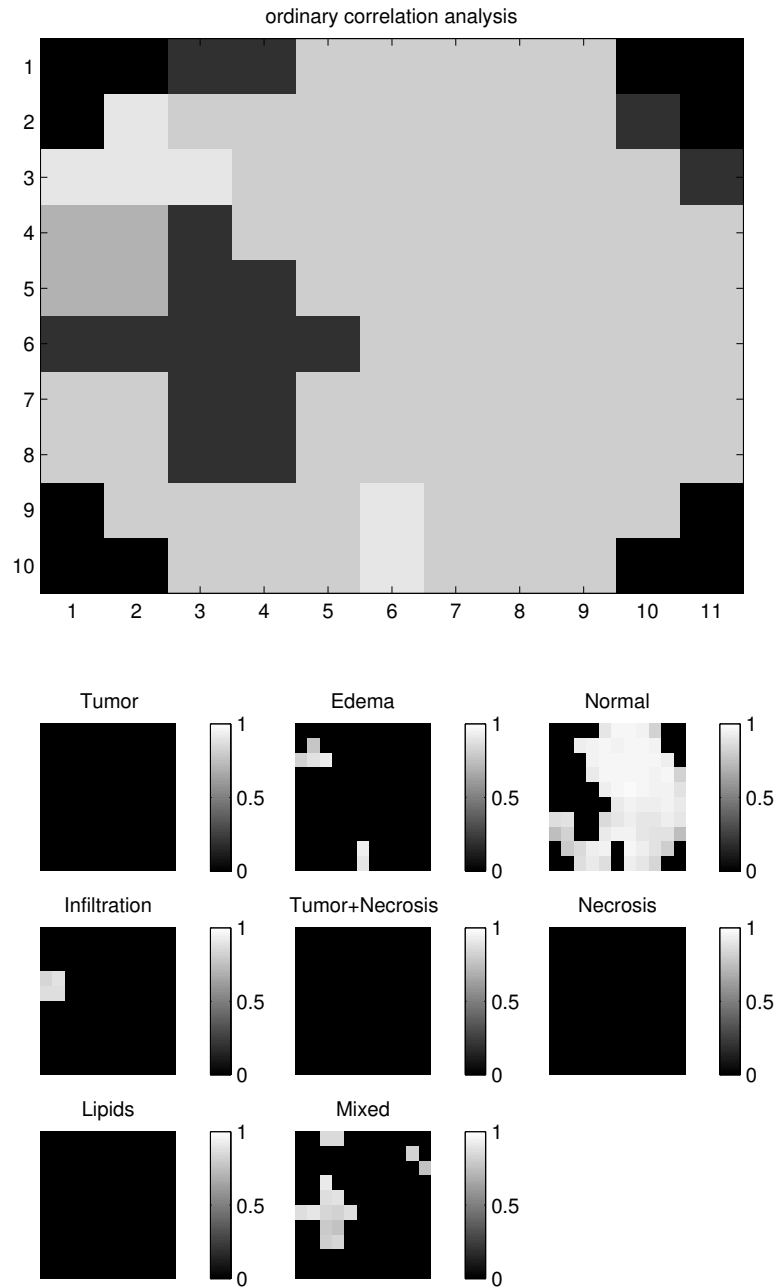


Figure 6.23. Area of interest of the 16th slice for Example 5.



**Figure 6.24.** Example 5. Top: nosologic image obtained by CCA. Spatial model: symmetric  $3 \times 3$  without corner voxels. Subspace model: Taylor. Bottom: correlation maps corresponding to all the tissue types.



**Figure 6.25.** Example 5. Top: nosologic image obtained by ordinary correlation analysis. Bottom: correlation maps corresponding to all the tissue types.

# CONCLUSIONS AND FURTHER RESEARCH

*In this chapter the main findings and conclusions of the thesis are summarized. Finally, the ongoing research work and suggestions for possible future research directions are described.*

## 7.1 Summary

The aim of this thesis is the development of accurate, robust and efficient subspace-based algorithms for the quantification of time domain MRS signals, and for the tissue segmentation and classification of MRSI data. Below, a short overview of the main contributions is provided.

### 7.1.1 Quantification of MRS signals

A well known subspace-based parameter estimation method is HSVD. The computationally most intensive part of this method is the computation of the truncated SVD of the Hankel data matrix. A more efficient version of HSVD is already available in the literature and is called HLSVD. It is freely available in the MRUI software package and very frequently used for solvent suppression. HLSVD efficiently computes the truncated SVD by using the Lanczos bidiagonalization algorithm. Unfortunately, when working in finite precision arithmetic, numerical problems occur and, although the van Kats – van der Vorst procedure is applied in order to overcome such problems, HLSVD sometimes fails in the estimation of the parameters of interest.

We propose two alternative Lanczos-based variants of HSVD, namely HLSVD-PRO and HLSVD-IRL, based on more robust implementations of the Lanczos algorithm, i.e., the Lanczos algorithm with partial reorthogonalization and the implicitly restarted Lanczos algorithm. Via extensive simulation studies, the performance of HLSVD, HLSVD-PRO and HLSVD-IRL is compared in terms of numerical reliability and computational efficiency. Our studies show that the proposed variants perform best.

### 7.1.2 Quantification of MRS signals using prior knowledge

MRS data are very often characterized by biochemical prior knowledge, the use of which significantly improves the performance of the parameter estimation methods in terms of robustness and accuracy. Unfortunately, subspace-based methods allow limited inclusion of prior knowledge, and, although several methods have been developed that make use of prior knowledge, their performance is generally worse than that of the optimization-based methods.

We propose a new subspace-based algorithm, called KNOB-TLS, that allows the use of more prior knowledge about the signal parameters than previously published subspace-based methods. Its performance is compared with that of three commonly used methods, namely the subspace-based methods HTLSPK( $\Delta f d_{eq}$ ) and HTLS, and the optimization-based method AMARES. Extensive simulation and *in vivo*

studies, using  $^{31}\text{P}$  as well as  $^1\text{H}$  MRS signals, show that the new method outperforms HTLS and HTLSPK( $\Delta f d_{eq}$ ) in robustness and accuracy, and that it provides parameter estimates comparable to the AMARES ones.

### 7.1.3 Tissue segmentation and classification of prostate MRSI data

The second part of the thesis is devoted to the development of an efficient and accurate tissue typing technique. This is based on the use of a statistical method, called Canonical Correlation Analysis (CCA), that represents the multivariate variant of the ordinary correlation analysis and has already been successfully applied to functional Magnetic Resonance Imaging data in order to map sensor, motor and cognitive functions to specific areas in the brain. CCA is adapted for MRSI data processing in order to detect possible homogeneous tissue regions characterizing the considered sample. The goal is achieved by exploiting the spectral-spatial information provided by the MRSI data set. CCA is used to quantify the relationship between two sets of variables, magnitude spectra of the measured data and the signal subspaces modelling the spectra of characteristic tissue types, by means of correlation coefficients. These coefficients are afterwards exploited in order to construct nosologic images in which all the detected tissues are visualized. The potential and limitations of the new technique are investigated by using simulated as well as *in vivo* prostate MRSI data, and the performance of CCA is compared to that of ordinary correlation analysis. The test results show that CCA performs best in terms of accuracy and robustness.

### 7.1.4 Tissue segmentation and classification of brain 2DTSI data

The performance of CCA as a tissue typing technique is further investigated by using brain 2DTSI data, where 2DTSI stands for two-dimensional Turbo Spectroscopic Imaging. More precisely, 2DTSI is a fast acquisition procedure able to provide data with a relatively high spatial resolution in a few minutes ( $\approx 6$  minutes for the human brain instead of  $\approx 30$  minutes). Five 2DTSI data sets are measured in patients affected by glioblastoma, which represents one of the most heterogeneous brain tumors. CCA is then applied in order to retrieve the possible tissue types characterizing the considered data sets. The purpose of this study is twofold: to carry out a validation study on CCA when applied as a tissue typing technique to heterogeneous tumors, and to develop an MRSI technique that is able to combine a fast acquisition procedure (TSI) with a reliable and fast classification method (CCA). The results show that CCA is an accurate and fast tissue typing technique and outperforms ordinary correlation analysis.

## 7.2 Further research

### 7.2.1 CCA based on selected MRSI data features

In the evaluation studies described in Chapters 5 and 6, the data processed by CCA were the magnitude spectra (for the prostate example) or the real part of the spectra (for the brain examples). In fact, CCA was used to quantify the relationship between two sets of variables, spectra of the measured data and the tissue signal subspace, by means of correlation coefficients. An alternative approach of CCA can be considered and is currently under investigation. The new approach makes use of selected MRS and MRI features instead of spectra. More precisely, the MRSI signals are first quantified by using a robust and accurate parameter estimation method. Afterwards, the estimated amplitudes of the metabolites of interest and four MRI variables ( $T_1$ -weighted,  $T_2$ -weighted, proton density image and gadolinium enhanced- $T_1$ ) are selected for each voxel of the MRSI grid. These quantities form a vector of features that can be used in the CCA technique to identify the different tissue types.

### 7.2.2 CCA applied to three-dimensional MRSI data

In this thesis, the tissue typing technique based on CCA was only applied to two-dimensional MRSI/TSI data. More precisely, only the slices of interest were processed and the processing only involved one slice per time. Therefore, only two-dimensional spatial information was exploited and the detection and classification results were only shown for the slices under investigation. It would be interesting to develop a CCA-based technique able to detect and classify tissues in three dimensions. To this aim, two possible approaches could be adopted. The first one consists of applying CCA to each slice and, once all the slices have been processed, to combine the detection results in a single three-dimensional image. The second approach could be based on the development of a three-dimensional version of CCA, that is able to exploit the three-dimensional spatial information present in the MRSI data. To this aim, three-dimensional spatial models are needed and their performance needs to be studied by using simulation as well as *in vivo* studies. The two different approaches could be investigated and compared in order to provide the best three-dimensional tissue typing technique.

### 7.2.3 Tissue assignment criterion in CCA

As already specified above, CCA was used to quantify the relationship between two sets of variables, spectra of the measured data and the tissue signal subspace, by means of correlation coefficients. These coefficients were afterwards exploited in order to construct nosologic images in which all the detected tissues were visualized. More precisely, the nosologic image was obtained by comparing, voxel by voxel, the canonical coefficients characterizing the different tissue correlation maps. The considered voxel was then assigned to the tissue with highest canonical coefficient and

labelled by the corresponding tissue color. This adopted assignment criterion was quite deterministic. An alternative approach could be the following one: introduce a threshold value for the correlation coefficients in order to properly classify the voxels of the slice under investigation. However, the choice of a suitable threshold is a delicate issue and future research studies could be devoted to its selection and to the investigation of the performance of CCA based on this new assignment criterion.

#### **7.2.4 Multistage CCA**

Finally, a multistage approach of CCA could be applied. In fact, MRSI data are often characterized by the presence of uninteresting voxels. CCA could be first applied to remove such voxels (first stage) and, afterwards, to characterize the tissue types present in the area of interest (second stage).

An alternative multistage approach could also be the following one: to detect the tumor tissue type by using rough model spectra (first stage) and, once the tumor type is known, to use a set of refined model spectra in order to define the tumor grade (second stage).



---

---

# BIBLIOGRAPHY

- [1] E. Anderson, Z. Bai, C. Bischof, J. Demmel, J. Dongarra, J. Du Croz, A. Greenbaum, S. Hammarling, A. McKenney, S. Ostrouchov, and D. Sorensen, *LAPACK Users' Guide*, SIAM, Philadelphia, 1995.
- [2] H. Barkhuysen, R. de Beer, and D. van Ormondt, *Improved algorithm for noniterative time-domain model fitting to exponentially damped magnetic resonance signals*, J. Magn. Reson., 73:553-557, 1987.
- [3] K.L. Behar, D.L. Rothman, D.D. Spencer, and O.A.C. Petroff, *Analysis of macromolecule resonances in  $^1H$  NMR spectra of human brain*, Magn. Reson. Med., 32:294-302, 1994.
- [4] J.C. Bezdek, L.O. Hall, and L.P. Clarke, *Review of MR image segmentation techniques using pattern recognition*, Medical Physics, 20:1033-1048, 1993.
- [5] D. Calvetti, L. Reichel, and D.C. Sorensen, *An implicitly restarted Lanczos method for large symmetric eigenvalue problems*, Electron. Trans. Numer. Anal., 2:1-21, 1994.
- [6] B. Casanova, M.C. Martínez-Bisbal, C. Valero, B. Celda, L. Marti-Bonmatí, A. Pascual, et al., *Evidence of wallerian degeneration in the normal appearing white matter in the early stages of relapsing-remitting multiple sclerosis. A  $^1H$ -MRS study.*, J. Neurol., 250:22-28, 2003.
- [7] S. Cavassila, S. Deval, C. Huegen, D. van Ormondt, and D. Graveron-Demilly, *The beneficial influence of prior knowledge on the quantitation of in vivo magnetic resonance spectroscopy signals*, Invest. Radiol., 34(3):242-246, 1999.
- [8] S. Cavassila, S. Deval, C. Huegen, D. van Ormondt, and D. Graveron-Demilly, *Cramer-Rao Bounds: an evaluation tool for quantitation*, NMR Biomed., 14:278-283, 2001.
- [9] H. Chen, *Subspace-Based Parameter Estimation of Exponentially Damped Sinusoids with Application to Nuclear Magnetic Resonance Spectroscopy Data*, PhD thesis, Faculty of Engineering, K.U.Leuven (Leuven, Belgium), 194 p, May 1996.

- [10] H. Chen, S. Van Huffel, C. Decanniere, and P. Van Hecke, *A signal enhancement algorithm for time-domain data MR quantification*, J. Magn. Reson., Series A, 109:46-55, 1994.
- [11] H. Chen, S. Van Huffel, D. van Ormondt, and R. de Beer, *Parameter estimation with prior knowledge of known signal poles for the quantification of NMR data in the time domain*, J. Magn. Reson., Series A, 119:225-234, 1996.
- [12] H. Chen, S. Van Huffel, and J. Vandewalle, *Improved methods for exponential parameter estimation in the presence of known poles and noise*, IEEE Trans. Signal Process., 45(5):1390-1393, 1997.
- [13] H. Chen, S. Van Huffel, A.J.W. Van den Boom, and P.P.J. Van den Bosch, *Subspace-based parameter estimation of exponentially damped sinusoids using prior knowledge of frequency and phase*, Sig. Proc., 59:129-136, 1997.
- [14] G.B. Coleman, H.C. Andrews, *Image segmentation by clustering*, Proceedings of the IEEE, 5:773-785, 1979.
- [15] L.C. Costello, R.B. Franklin, and P. Narayan, *Citrate in the diagnosis of prostate cancer*, The Prostate, 38:237-245, 1999.
- [16] J.K. Cullum and R.A. Willoughby, *Lanczos algorithms for large symmetric eigenvalue computations*, Vol. 1, Theory, Birkhäuser, Boston, 1985.
- [17] R.A. de Graaf, *In vivo NMR spectroscopy*, Wiley, England, 1998.
- [18] A.A. de Graaf, and W.M. Bovee, *Improved quantification of in vivo  $^1H$  NMR spectra by optimization of signal acquisition and processing and by incorporation of prior knowledge into the spectral fitting*, Magn. Reson. Med., 15(2):305-319, 1990.
- [19] J.E. Dennis, D.M. Gay, and R.E. Welsch, *An adaptive nonlinear least-squares algorithm*, ACM TOMS, 7(3):348-368, 1981.
- [20] J.E. Dennis, D.M. Gay, and R.E. Welsch, *Algorithm 573 NL2SOL - an adaptive nonlinear least-squares algorithm*, ACM TOMS, 7(3):369-383, 1981.
- [21] J.H. Duyn, and C.T.W. Moonen, *Fast proton spectroscopic imaging of human brain using multiple spin echoes*, Magn. Reson. Med., 30:409-414, 1993.
- [22] O. Friman, *Adaptive Analysis of Functional MRI Data*, PhD thesis, Dept. Biomed. Engin. Linkpings Univ., Sweden, 2003.
- [23] M. Gadea, M.C. Martínez-Bisbal, L. Marti-Bonmatí, R. Espert, B. Casanova, F. Coret, and B. Celda, *Spectroscopic axonal damage of the right locus coeruleus relates to selective attention impairment in early stage relapsing-remitting multiple sclerosis*, Brain, 127(1): 89-98, 2004.

- [24] D.G. Gadian, *NMR and its applications to living systems*, Oxford Science publishers, second edition, 1995.
- [25] G.H. Golub, and C.F. Van Loan, *Matrix Computations*, 3rd ed., The Johns Hopkins Univ. Press, Baltimore, MD, 1996.
- [26] G.H. Golub, and V. Pereyra, *The differentiation of pseudo-inverses and non linear least squares problems whose variables separate*, SIAM, J. Numer. Anal., 10(2):413-432, 1973.
- [27] G.H. Golub and C. Reinsch, *Singular value decomposition and least squares solutions*, Numer. Math., 14:403-420, 1970.
- [28] G.H. Golub, and H. Zha, *In: A. Bojanczyk and G. Cybenko, editors. Linear Algebra for Signal Processing*, New York: Springer, 59-82, 1995.
- [29] V. Govindaraju, K. Young, and A. Maudsley, *Proton NMR chemical shifts and coupling constants for brain metabolites*, NMR Biomed., 13:129-153, 2000.
- [30] K. Held, E.R. Kops, B.J. Krause, W.M. Wells, R. Kikinis, and H.W. Muller-Gartner, *Markov random field segmentation of brain MR images*, IEEE Transactions on Medical Imaging, 16(6):878-886, 1997.
- [31] H. Hotelling, *Relation between two sets of variates*, Biometrika, 28:321-377, 1936.
- [32] A.C. Kuesel, G.R. Sutherland, W. Halliday, and I.C.P. Smith,  *$^1H$  MRS of high grade astrocytomas: mobile lipid accumulation in necrotic tissue*, NMR Biomed., 7:149-155, 1994.
- [33] S.Y. Kung, K.S. Arun, and D.V. Bhaskar Rao, *State-space and singular value decomposition-based approximation methods for the harmonic retrieval problem*, J. Opt. Soc. Am., 73(12):1799-1811, 1983.
- [34] R.M. Larsen, *Lanczos bidiagonalization with partial reorthogonalization*, PhD thesis, Department of Computer Science, University of Aarhus, Denmark, 1998.
- [35] T. Laudadio, N. Mastronardi, L. Vanhamme, P. Van Hecke, and S. Van Huffel, *Improved Lanczos algorithms for blackbox MRS data quantitation*, J. Magn. Reson., 157:292-297, 2002.
- [36] T. Laudadio, Y. Selén, L. Vanhamme, P. Stoica, P. Van Hecke, and S. Van Huffel, *Subspace-based MRS data quantitation of multiplets using prior knowledge*, J. Magn. Reson., 168:53-65, 2004.
- [37] T. Laudadio, P. Pels, L. De Lathauwer, P. Van Hecke, and S. Van Huffel, *Tissue segmentation and classification of MRSI data using Canonical Correlation Analysis*, accepted for publication by Magn. Reson. Med., 2005.

- [38] R.B. Lehoucq, D.C. Sorensen, and C. Yang, *ARPACK Users's guide: solution of large scale eigenvalue problems with implicitly restarted Arnoldi methods*, SIAM, Philadelphia, 1998.
- [39] J.F. Mangin, V. Frouin, I. Bloch, J. Regis, and J. Lopez-Krahe, *From 3D magnetic resonance images to structural representations of the cortex topography using topology preserving deformations*, Journal of Mathematical Imaging and Vision, 5:297-318, 1995.
- [40] I. Marshall, J. Higinbotham, S. Bruce, and A. Freise, *Use of Voigt lineshape for quantification of in vivo  $^1H$  spectra*, Magn. Reson. Med., 37:651-657, 1997.
- [41] A.J. Martin, H. Liu, W.A. Hall, and C.L. Truwit, *Preliminary Assessment of Turbo Spectroscopic Imaging for Targeting in Brain Biopsy*, Am. J. Neuroradiol., 22:959-968, 2001.
- [42] A. Naressi, C. Couturier, J.M. Devos, M. Janssen, C. Mangeat, R. de Beer, et al., *Java-based graphical userinterface for the MRUI quantitation package*, MAGMA, 12:141-152, 2001.
- [43] D.P. O'Leary, and J.A. Simmons, *A bidiagonalization-regularization procedure for large scale discretizations of ill-posed problems*, SIAM J. Sci. Stat. Comput., 2(4):474-489, 1981.
- [44] M. Osborne, *Some aspects of non-linear least squares calculations*, In Numerical Methods for Non-linear Optimization, Lootsma, FA (ed.), Academic Press, London, 1972.
- [45] C.C. Paige, *The computation of eigenvalues and eigenvectors of very large sparse matrices*, Ph.D. thesis, London University, 1971.
- [46] W.W.F. Pijnappel, A. Van den Boogaart, R. de Beer, and D. van Ormondt, *SVD-based quantification of magnetic resonance signals*, J. Magn. Reson., 97:122-134, 1992.
- [47] S.W. Provencher, *Estimation of metabolite concentrations from localized in vivo proton NMR spectra*, Magn. Reson. Med., 30(6), 1993.
- [48] H. Ratiney, Y. Coenradie, S. Cavassila, D. van Ormondt, and D. Graveron-Demilly, *Time-domain quantitation of  $^1H$  short echo-time signals: Background accommodation*, MAGMA, 16:284-296, 2004.
- [49] W.E. Reddick, J.O. Glass, E.N. Cook, T.D. Elkin, and R.J. Deaton, *Automated segmentation and classification of multispectral magnetic resonance images of brain using artificial neural networks*, IEEE Transactions on Medical Imaging, 16:911-918, 1997.
- [50] J. Rissanen, *Modelling by shortest data description*, Automatica, 14:465-471, 1978.

- [51] P.K. Sahoo, S. Soltani, and A.K.C. Wong, *A survey of thresholding techniques*, Computer Vision, Graphics and Image Processing, 41:233-260, 1988.
- [52] M.L. Schiebler, J.E. Tomaszewski, M. Bezzi, H.M. Pollack, H.Y. Kressel, and E.K. Cohen, *Prostatic carcinoma and benign prostatic hyperplasia: correlation of high-resolution MR and histopathologic findings*, Radiology, 172(1):131-137, 1989.
- [53] G. Schwartz, *Estimating the dimension of a model*, Ann. Stat., 6:461-464, 1978.
- [54] D. Sima, and S. Van Huffel, *Regularized semiparametric model identification with application to NMR signal quantification with unknown macromolecular baseline*, Journal of Royal Statistical Society: Series B, accepted for publication, 2006.
- [55] H.D. Simon, *The Lanczos algorithm with partial reorthogonalization*, Math. Comp., Vol. 42, 165:115-142, 1984.
- [56] A.W. Simonetti, J.B. Poulet, D.M. Sima, B. De Neuter, L. Vanhamme, P. Lemmerling, and S. Van Huffel, *An open source short echo time MR quantitation software solution: AQSES*, Tech. Report, ESAT-SISTA, K.U.Leuven, Leuven, Belgium, 2005.
- [57] D.C. Sorensen, *Implicit applications of polynomial filters in a k-step Arnoldi method*, SIAM J. Matrix Anal. Appl., 13:357-385, 1992.
- [58] P. Stoica, Y. Selén, N. Sandgren, and S. Van Huffel, *Using Prior Knowledge in SVD-based parameter estimation for magnetic resonance spectroscopy - the ATP example*, IEEE Trans. on Biomedical Engineering, 51(9):1568-1578, 2004.
- [59] P. Stoica, and R. Moses, *Introduction to spectral analysis*, Prentice Hall, Uppers Saddle River, New Jersey, 1997.
- [60] P. Stoica, H. Li, and J. Li, *Amplitude estimation of sinusoidal signals: survey, new results and an application*, IEEE Trans. Signal Processing, 48:338-552, 2000.
- [61] P. Stoica, and T. Sundin, *Nonparametric NMR spectroscopy*, J. Magn. Reson., 152:57-69, 2001.
- [62] F. Szabo De Edelenyi, C. Rubin, F. Estve, S. Grand, M. Dcorps, V. Lefournier, J.F. Le Bas, C. Rmy, *A new approach for analyzing proton magnetic resonance spectroscopic images (1H MRSI) of brain tumors: nosologic images*, Nature Medicine, Vol. 6:11, 1287-1289, 2000.
- [63] P.N. Swartztrauber, R.A. Sweet, W.L. Briggs, Van Emden Hensen, and J. Otto, *Bluestein's FFT for arbitrary N on the hypercube*, Parallel Comput., 17:607-617, 1991.
- [64] J.W.C. van der Veen, R. de Beer, P.R. Luyten, and D. van Ormondt, *Accurate quantification of in vivo  $^{31}\text{P}$  NMR signals using the variable projection method and prior knowledge*, Magn. Reson. Med., 6:92-98, 1988.

- [65] L. Vanhamme, A. van den Boogaart, and S. Van Huffel, *Improved method for accurate and efficient quantification of MRS data with use of prior knowledge*, J. Magn. Reson., 129(1):35-43, 1997.
- [66] L. Vanhamme, S. Van Huffel, P. Van Hecke, and D. Van Ormondt, *Time-domain quantification of series of biomedical magnetic resonance spectroscopy signals*, J. Magn. Reson., 140(1):120-130, 1999.
- [67] L. Vanhamme, A. Van den Boogaart, and S. Van Huffel, *Improved Method for Accurate and Efficient Quantification of MRS Data with Use of Prior Knowledge*, J. Magn. Reson., 129:35-43, 1997.
- [68] L. Vanhamme, T. Sundin, P. Van Hecke, Ioannis Dologlou, and S. Van Huffel, *Accurate Quantification of  $^1H$  Spectra: From Finite Impulse Response Filter Design for Solvent Suppression to Parameter Estimation*, J. Magn. Reson., 139:189-204, 1999.
- [69] L. Vanhamme, A. van den Boogaart and S. Van Huffel, *Improved Method for Accurate and Efficient Quantification of MRS Data with Use of Prior Knowledge*, J. Magn. Reson., 129:35-43, 1997.
- [70] S. Van Huffel, L. Lagae, L. Vanhamme, P. Van Hecke, and D. van Ormondt, *Improving blackbox MRS data quantification by means of prior knowledge*, Abstracts of the 15th Annual Meeting European Society for Magnetic Resonance in Medicine and Biology (ESMRMB 98), Geneva, Switzerland, Sept. 17-20, 1998, paper no. 44, published in Magnetic Resonance Materials in Physics, Biology and Medicine (MAGMA), Vol. 6, Suppl. 1, p. 13, September 1998.
- [71] S. Van Huffel, H. Chen, C. Decanniere, and P. Van Hecke, *Algorithm for time-domain NMR data fitting based on total least squares*, J. Magn. Reson., Series A, 110:228-237, 1994.
- [72] S. Van Huffel, and D. van Ormondt, *Subspace-based exponential data modelling using prior knowledge*, Proceedings Signal Processing Symposium, IEEE Benelux Signal Processing Chapter (SPS 98), Leuven, Belgium, March 26-27, 211-214, 1998.
- [73] S. Van Huffel and J. Vandewalle, *The Total Least-Squares Problem: Computational Aspects and Analysis*, Frontiers in Applied Mathematics Series, Vol. 9, SIAM, Philadelphia, 1991.
- [74] H. Zha, *The Singular Value Decomposition Theory, Algorithms and Applications*, PhD thesis, Pennsylvania State University, University Park, PA 16802, 1993.

## PUBLICATION LIST

### Articles in International Journals

1. T. Laudadio, N. Mastronardi, L. Vanhamme, P. Van Hecke and S. Van Huffel, *Improved Lanczos algorithms for blackbox MRS data quantitation*, **Journal of Magnetic Resonance**, Vol. 157, pp. 292–297, 2002
2. T. Laudadio, Y. Selén, L. Vanhamme, P. Stoica, P. Van Hecke, S. Van Huffel, *Subspace-based MRS data quantitation of multiplets using prior knowledge*, **Journal of Magnetic Resonance**, Vol. 168, pp. 53-65, 2004
3. F. Diele, T. Laudadio, N. Mastronardi, *On some Inverse Eigenvalue Problems with Toeplitz-related Structure*, **SIAM J. Matrix Analysis and Applications**, vol. 26, no. 1, pp. 285-294, 2004.
4. T. Laudadio, P. Pels, L. De Lathauwer, P. Van Hecke, S. Van Huffel, *Tissue segmentation and classification of MRSI data using Canonical Correlation Analysis*, accepted as publication by **Magnetic Resonance in Medicine**, August 2005

### Articles in conference proceedings

1. T. Laudadio, N. Mastronardi, L. Vanhamme and S. Van Huffel, *Fast and stable algorithms for blackbox MRS data quantitation*, Proceedings of 12th PRORISC Workshop on Circuits, Systems and Signal Processing, Veldhoven, The Netherlands, November 29–30, pp. 480–488, 2001.

2. T. Laudadio, P. Pels, L. De Lathauwer, P. Van Hecke, S. Van Huffel, *Tissue segmentation of MRSI data using Canonical Correlation Analysis*, Proceedings of the Second International Conference on Computational Intelligence in Medicine and Healthcare (CIMED 2005), Lisbon, Portugal, June 2005.

### **Abstracts for international conferences**

1. T. Laudadio, Y. Selén, L. Vanhamme, P. Stoica, P. Van Hecke, S. Van Huffel, *Subspace-based MRS data quantitation of multiplets using prior knowledge*, Third Belgian Day on Biomedical Engineering, 17 October, 2003, Brussels, Belgium
2. T. Laudadio, Y. Selén, L. Vanhamme, P. Stoica, P. Van Hecke, S. Van Huffel, *Subspace-based MRS data quantitation of multiplets using prior knowledge*, Twelfth Scientific Meeting and Exhibition, 15-21 May, 2004, International Society for Magnetic Resonance in Medicine, Kyoto, Japan.
3. T. Laudadio, P. Pels, L. De Lathauwer, P. Van Hecke, S. Van Huffel, *Unsupervised tissue segmentation of MRSI data using Canonical Correlation Analysis*, Thirteenth Scientific Meeting and Exhibition, 7-13 May 2005, International Society for Magnetic Resonance in Medicine, Miami, Florida, USA.
4. T. Laudadio, P. Pels, L. De Lathauwer, P. Van Hecke, S. Van Huffel, *Tissue segmentation of MRSI data using Canonical Correlation Analysis*, Fifth Belgian Day

on Biomedical Engineering, 28 October, 2005, Brussels, Belgium

**Technical reports (including submitted papers)**

1. Laudadio T., Van Huffel S., *Extraction of independent components from fMRI data by Principal Component Analysis, Independent Component Analysis and Canonical Correlation Analysis*, Internal Report 04-89, ESAT-SISTA, K.U. Leuven (Leuven, Belgium), 2004.
2. S. Van Huffel, T. Laudadio, *Magnetic Resonance Spectroscopic Imaging: a survey of quantification and classification algorithms*, Internal Report 05-249, ESAT-SISTA, K.U. Leuven (Leuven, Belgium), 2005.
3. T. Laudadio, M.C. Martinez-Bisbal, B. Celda, S. Van Huffel, *Fast nosological imaging of 2DTSI brain data using Canonical Correlation Analysis*, Internal Report 05-250, ESAT-SISTA, K.U. Leuven (Leuven, Belgium), 2005.